INFORMATION TO USERS

This manuscript has been reproduced from the microfilm master. UMI films the text directly from the original or copy submitted. Thus, some thesis and dissertation copies are in typewriter face, while others may be from any type of computer printer.

The quality of this reproduction is dependent upon the quality of the copy submitted. Broken or indistinct print, colored or poor quality illustrations and photographs, print bleedthrough, substandard margins, and improper alignment can adversely affect reproduction.

In the unlikely event that the author did not send UMI a complete manuscript and there are missing pages, these will be noted. Also, if unauthorized copyright material had to be removed, a note will indicate the deletion.

Oversize materials (e.g., maps, drawings, charts) are reproduced by sectioning the original, beginning at the upper left-hand corner and continuing from left to right in equal sections with small overlaps. Each original is also photographed in one exposure and is included in reduced form at the back of the book.

Photographs included in the original manuscript have been reproduced xerographically in this copy. Higher quality 6" x 9" black and white photographic prints are available for any photographs or illustrations appearing in this copy for an additional charge. Contact UMI directly to order.

U·M·I

University Microfilms International
A Bell & Howell Information Company
300 North Zeeb Road Ann Arbor MI 48106-1346 USA
313 761-4700 800 521-0600

Order Number 9417514

Electron energy loss spectra and Auger spectra of thin films on transition metal substrates

Wu, Zhibiao, Ph.D.

City University of New York, 1994

U·M·I

300 N. Zeeb Rd.
Ann Arbor, MI 48106

ELECTRON ENERGY LOSS SPECTRA AND AUGER SPECTRA OF THIN FILMS ON TRANSITION METAL SUBSTRATES

by

ZHIBIAO WU

A dissertation submitted to the Graduate Faculty in Physics
in partial fulfillment of the requirements for
the degree of Doctor of Philosophy,
The City University of New York.

1994

This manuscript has been read and accepted for the Graduate Faculty in Physics in satisfaction of the dissertation requirement for the degree of Doctor of Philosophy

1/10/94
Date

J. M. Dickey
Professor J. M. Dickey
Chair of Examining Committee

1/10/94
Date

Joseph Krieger
Professor Joseph Krieger
Executive Officer

Professor Jacob Neuberger

Professor Miriam Rafailovich

Professor Henry Lancman

Jonathan Sokolov
Professor Jonathan Sokolov

Supervisory Committee

The City University of New York

Abstract

ELECTRON ENERGY LOSS SPECTRA AND AUGER SPECTRA OF THIN FILMS ON TRANSITION METAL SUBSTRATES

by

Zhibiao Wu

Advisor: Professor J. M. Dickey

Al is an ideal metal for studying the electron energy loss spectra (EELS) since both bulk and surface plasmons are prominent and are well explained by a nearly free electron model. For the transition metals, on the other hand, the situation is complicated by *d*-band effects. Thin films of Al and Sn have been grown on the transition metals Nb, Mo and Ta as substrates. The EELS measurements have been taken during the growth and annealing of the films. For very thin films we see a transition from the characteristic Al (Sn) spectra and the appearance of extra structures which may be associated with the interface between the transition metal and the films.

Several Sn films were studied to investigate the growth mechanism, thermal stability, and possible alloy formation during the anneals. A similar four-stage annealing behaviour of Sn films on the substrates Nb and Mo was observed in both the AES and the EELS spectra. There were the systematic shifts of the break points, for changing from one stage to another, to higher temperatures when the thickness of the film increases. The initial stages of the growth of a Sn film on a clean Nb substrate have been examined for comparison with the

theoretical models, which have been proposed for the different modes in which a film may grow depending on the relative surface energies of the adsorbate and substrate. The experimental data have been displayed as an AA–*t* (Auger Amplitude versus deposition time) plot, which is consistent with the Stranski-Krastanov (SK) model and from which the attenuation length of the electrons has been determined.

Acknowledgments

First and foremost, I would like to express my very special gratitude to Professor J. M. Dickey for her inspiration and unflagging enthusiasm in the guidance of this project. I am deeply grateful for having had the opportunity to meet and work with her. A special note of appreciation goes to Dr. Lawrence Ferrari for his assistance of providing some equipment. To the Physics Department of Queens College, I am indebted for the academic and financial support that I have received during my studies here. I would also like to thank Grigory German and Paul Schaedler for their help and cooperation as well as for their time, effort, and technical assistance. My special thanks go to my brother, my parents and especially to my wife Yifang, for their understanding, valuable encouragement, and moral support, and finally to my dearest daughter Winnie who missed me so much and her interruptions during the study provided an enjoyable break.

Table of Contents

List of Tables

List of Figures

Chapter 1. Introduction

A common feature of electron spectroscopy methods is the possibilities of getting a high surface sensitivity by taking advantage of the short penetration and escape depth of the electrons in solids. We used electron energy loss spectroscopy (EELS)[1] and Auger electron spectroscopy (AES)[2,3]. The objective of this thesis is to present studies of surface plasmons of pure metals and interface plasmons (overlayer plasmons) of thin films by means of EELS. Also presented are the examinations of the thermal stability and the growth mechanism of the thin films by using AES.

The adsorption of metals on refractory metal substrates continues to be of considerable interest in many areas for several years[4,5]. Periodic multilayer films that consist of many interfaces and which do not usually occur in nature have attracted much attention for technical applications like a high intensity monochromator for diffraction experiments. In recent years another interest has developed in magnetic metallic super lattices as a possible device for data storage using the Kerr effect. Consequently a proper understanding of the surface and interface properties is not only of academic interest but also has practical applications.

Plasmon loss features, which are observed as satellites of the no-loss peaks in UPS, XPS, and AES, are also well known in EELS. EELS is a technique which is flexible and is sensitive to the character of the surface and changes in the valence band density of states. In addition the depth of the surface layers sampled can be varied by changing the energy of the incident electrons. Present theories about plasmons provide nice descriptions for nearly-free-election metals, but the interpretation of characteristic EELS for transition metals is complicated by the

possibility of interband transitions. Furthermore, extra structures in the EELS of thin films and semiconducting superlattice (semiconductor multilayer systems) have been of continuing theoretical and experimental interest[6,7].

Beginning with the pioneering work of Frank and van der Merwe[8], theoretical studies of the energetics of epitaxial growth, including Monte Carlo simulations, molecular-dynamics simulations and phenomenological methods, have provided an important basis for understanding the growth modes and stability of films[8,9]. Experimentally the AA–*t* (Auger Amplitude–time) plot of AES measurements, taken as the film is gradually build up, provides information for determining the thin film growth mechanism[10]. Moreover, by analyzing the AA *t* plot one can find the corresponding attenuation length in the film of the Auger electrons from the adsorbate and the substrate[11]. When the film is heated the mobility of the atoms increases so the structure of the film will change. Measuring the AES peak signal heights versus the anneal temperature will release some clues for analyzing these changes.

Chapter 2. Experimental

2.1 Apparatus

Figure 1 shows, schematically, the major components of the apparatus. To study the properties of a surface the basic condition is that the composition of the surface must remain constant; in other words, the rate of arrival of reactive species from the surrounding gas should be as low as possible. The arrival rate of atoms or molecules from a gas of density n and with an average velocity υ is[12]:

$$R = \frac{1}{4} n v = 3.51 \times 10^{22} \times \frac{P}{\sqrt{mT}} \qquad (2.1.1)$$

where P, m, T are the pressure, mass of an atom, and the temperature respectively.

For O_2 at $T = 300K$, if $P = 10^{-9}$ Torr, then $R = 3.58 \cdot 10^{13} / cm^2 \cdot s$; since a monolayer is about $(6.02 \times 10^{23} cm^3)^{2/3} \cong 10^{15} / cm^2$, a 'clean' surface will be covered with a monolayer of oxygen in about 30 minutes with system pressure $\sim 10^{-9}$ Torr; so for the surface study we need a vacuum system with pressure of 10^{-10} Torr or better. In our laboratory a high vacuum system made by Varian was used. The chamber was constructed of stainless steel; the high vacuum seals were made with stainless steel knife edge flanges and copper gaskets to keep the system tight. Fore pumping to a pressure less then about a micron was accomplished with an oil free mechanical pump and a Vac Sorb pump containing a molecular sieve that was chilled with liquid nitrogen. Then the system was pumped by an 110 liter per second ionization pump. That was done by first closing the valve that separates the upper half system and the ion pump located at the bottom of the system, then

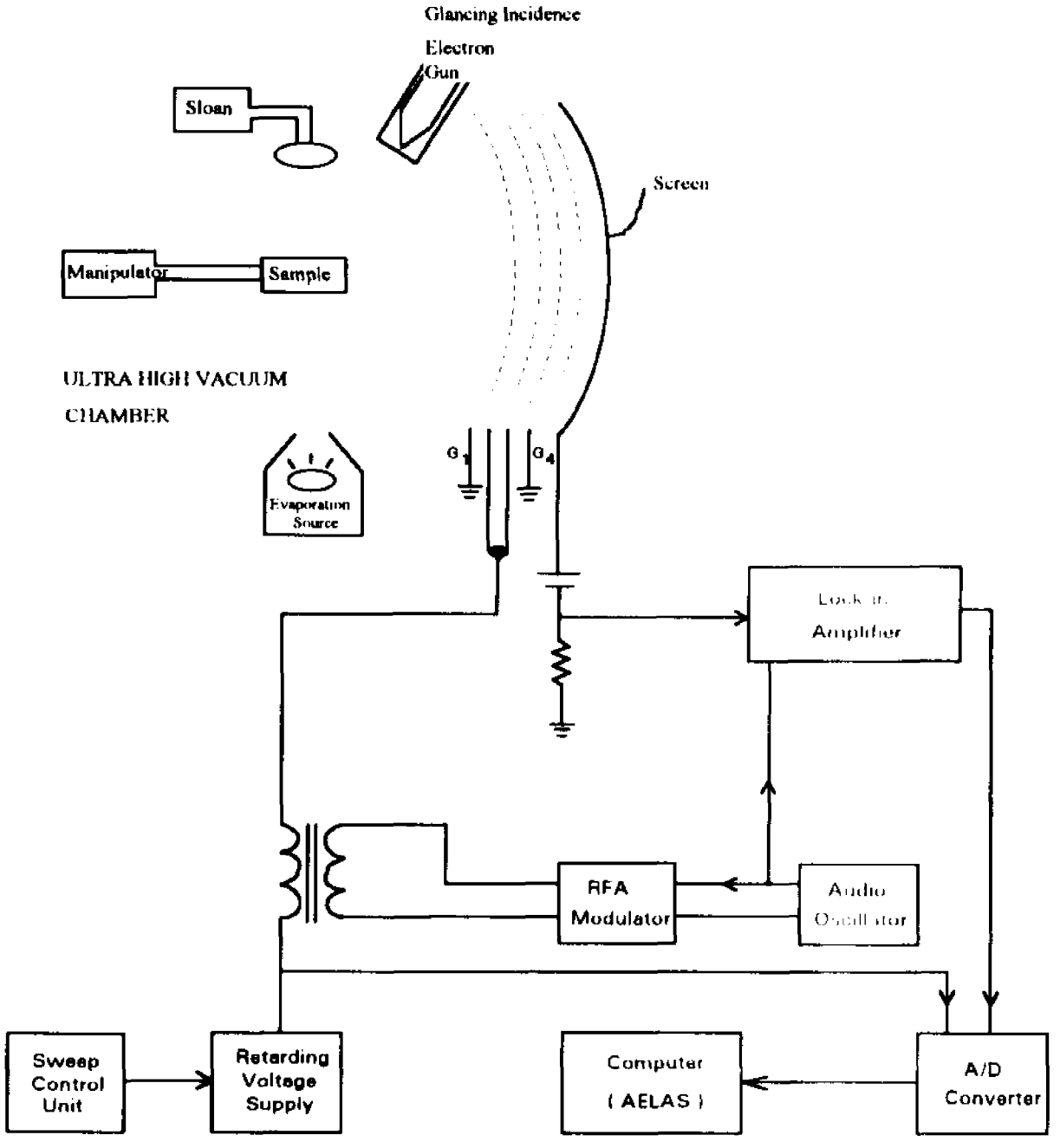

Figure 1. Schematic diagram of the vacuum system and electronics.

slowly opening the valve after the pressure of the lower half system reached 10^{-7} Torr or lower. We have to do the pumping in these two steps way due to the capability of the ion pump, and we found that success is much easier on going from the first step to the second step if we give the first step a long time pumping. Usually it takes two or three hours for the system to reach the pressure around low 10^{-7} to high 10^{-8} Torr range. A titanium sublimation pump was used to help pump down the system too. The chamber was baked ~ 200 °C for several hours after the ion pump was on the whole system. The base pressure of the system could be brought to less than 10^{-9} Torr, and usually the pressure of the system was in the low 10^{-8} Torr range or lower during a thermal evaporation.

The sample holder was attached to a manipulator which allowed us to precisely control its position and orientation. The sample can be moved into and out of the regions of heating, detection, and evaporation by rotating the central shaft and compressing or expanding the bellows. The manipulator's central shaft was electrically isolated from the chamber and the sample. The sample holder was connected via thick copper leads to high current feed throughs. A power-supply provided the high current required to heat the sample to almost 2000 °C. A thermocouple of tungsten and rhenium was spot welded onto the sample to monitor the sample's temperature. The temperature was also measured by an optical pyrometer to make the calibrations.

The thin films were grown by the thermal evaporation method. The thermal evaporation was done by heating the evaporate source material in a basket or boat above its melting temperature, after outgassing of the basket or boat. From our experience it is much easier to control the evaporation rate for the 'used' basket or boat rather than the brand new one. Besides it is also quicker to pump down the system to its base pressure after the pre-outgassing of the 'used' basket, while for

a brand new one, it is a little bit tricky to control the evaporation rate if we intend to keep the rate at a constant value. A Sloan meter (OMNI III) was used to measure the thickness of the film during the thermal evaporation.

The detector and display system consists of a Retarding Field Analyzer (RFA), consisting of a LEED optics and associated electronics, a lock-in amplifier, an A/D (analog to digital) converter and a compatible IBM PC. The retarding grid system, as shown in figure 1, uses four grids to improve the collected signal's quality. The middles two grids were connected together and the outer two grids were connected to ground to sharpen the spectra by reducing field penetration affects. The electron gun used to bombard the sample was also focused to increase the yield of electrons. The collected electron current from the RFA was input to the lock-in amplifier made by Princeton Applied Research. The output analog signals were digitized by using the LabMaster[13] converter (12 bit resolution, 16 channels, and 30 KHZ sampling speed maximum). The board has programmable gain which may be selected to be 1, 10, 100, or 500, which corresponds respectively to 10 V, 1 V, 100 mV, and 20 mV full scale range. This analog to digital converter (ADC) is located outside the PC and near the lock-in amplifier and sweep unit; therefore the sensitive ADC is isolated from internal electrical noise of the PC. This arrangement optimizes the analog signal clarity providing the most accurate readings. Finally the digital data served as the raw data input of AELAS (abbreviation of: Auger Electron spectroscopy Lab Analysis System) which is a software written in C by Dr. Dickey and me[14]. AELAS will automatically change the A/D converter gain to avoid losing significant bits of the original data due to changes in order of magnitude of the input signals. AELAS can save the original data; show the AES curve simultaneously while the data is being taken or retrace the curve later for analysis; do some basic mathematical

analysis such as Savitzky-Golay[15] polynomial smooth, Auger signal's peak-to-peak height calculations; go to DOS shell without quitting from AELAS, etc.

2.2 General Techniques

2.2.1 Sample Preparation

The sample substrate foil with dimensions' 5 cm × 15 cm and high purity of Marz grade[16] (99.999%) was attached to the holders by using a spot welder with typically a power of 250 W and current of ~ 28 A for Nb, ~ 30 for Ta, and ~32 A for Mo. The holders used for Nb, Mo, and Ta were thick foil of Nb, Mo, and Ta respectively to avoid introducing new impurities. Before being mounted in the experimental chamber the sample foil was pre-cleaned in methanol for 30 minutes by using a 125 watt ultrasonic cleaner made by Fisher. After the sample was transferred into the UHV system and the pressure of the system had been brought down to its base pressure, the foil was cleaned by heating at temperatures of about 2000 °C for Nb, 1700 °C for Mo, and 2200 °C for Ta, approaching their melting points, until AES cannot detect any C, O, N or other impurities. The heating process was done in several stages of 2~3 hours' heating with different temperatures. The main contaminants of the substrates were oxygen, carbon, nitrogen, and tantalum for niobium, and also tungsten for molybdenum and tantalum. The concentration of the impurities is, separately, less than 40 ppm (parts per million) for tantalum, 200 ppm for niobium and 480 ppm for molybdenum[16]. The clean surfaces of Al and Sn were prepared by thermal deposition of a thick film of the pure metals; Al was evaporated from

12A-3x.025W[17] baskets while S19B-TA[17] boats were used for the deposition of Sn.

2.2.2 Temperature Measurement

We used both a thermocouple and an optical pyrometer to measure the samples' temperatures. The thermocouple was composed of W-3%Re/W-25%Re wires. It was a little bit tricky to weld the thermocouple wires onto the desired position. Generally the thermocouple is mounted at the edge of the sample instead of the middle, since if we melt the thermocouple to the center of the sample, some dots will be made on center of the sample during melting. Those dots will later contaminate the surface of the sample and weaken the sample so it may more likely break when it is heated to a high temperature for cleaning. Due to this kind of mounting, the temperature measured by the thermocouple is not the same as that measured from the optical pyrometer. The optical pyrometer can be focused on the sample and measure the highest temperature that is usually at the middle of a sample, and also any variation in temperature across the sample. By measuring simultaneously the temperatures from both the optical pyrometer and thermocouple, very good thermocouple calibration curves can be obtained. The sample's temperatures should be measured at the surface analysis region, if this is not possible due to the practical difficulties the temperatures were obtained from the measured thermocouple voltages. Since the optical pyrometer cannot read the lower temperatures ($< 750^{\circ}C$), the extrapolated part of the temperature-volt curve was used to determine the low temperatures. A typical thermocouple temperature-volt curve is shown in figure 2 where all the experimental data (in

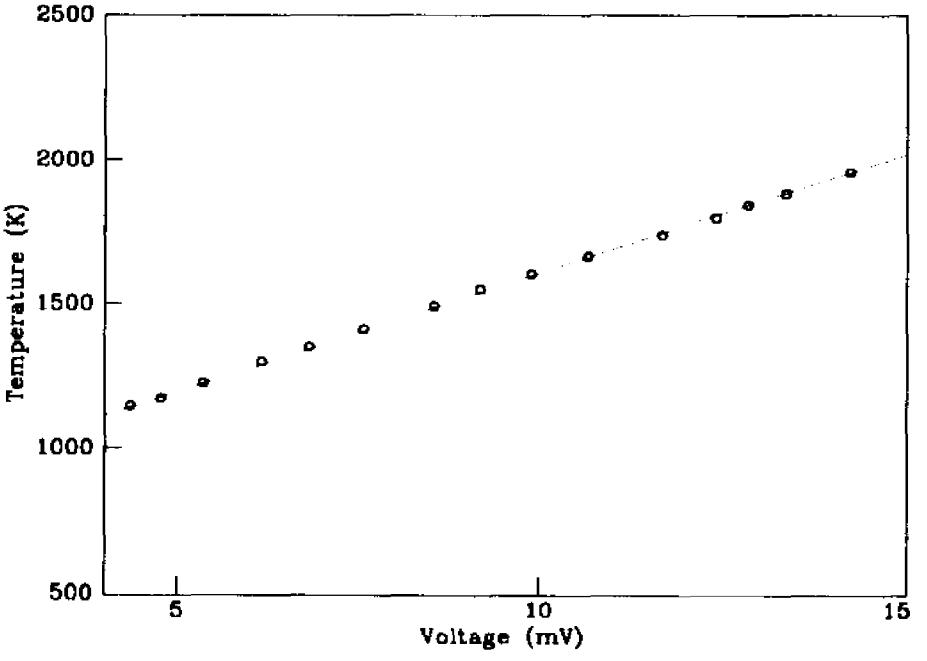

Figure 2. A typical thermocouple curve of the temperature as a function of voltage.

circle) are well fitted to a straight line. The measured voltages of the thermocouple are automatically recorded by the computer. From time to time the calibration curve was checked during a run. For each run a similar curve was obtained.

2.2.3 Thermal Evaporation and Annealing

The thermal evaporation method was used for the thin film growth. Since the transition metals react strongly with the oxygen, they were always heated to a high temperature immediately before each evaporation to ensure a clean surface. The Sloan meter monitors the vapor flux when the evaporate source had been heated to high enough temperature (figure 3). The substrate was moved into the evaporate region when a slow, stable evaporation rate had been gotten by adjusting the boats (or baskets) heating currents, then it was moved away after the desired thickness had been reached. The key point during the thermal evaporation is to get a reasonable high temperature but not too high, so the evaporation rate during the process is slow and stable. We usually made the evaporation rate maintained at 0.1 Å/s or 0.2 Å/s measured by the Sloan meter. For Sn, the pressure rise during evaporation was less than 5×10^{-8} Torr, and with aluminum, the pressure increased to 9×10^{-8} Torr during deposition. The AES and plasmon loss spectra's data were recorded within a 20–30 minute's period following the evaporation. The detailed evaporation conditions of Al and Sn are listed in table1. The commercially available evaporation source used were Marz grad[16] (99.999%) Al wires and 99.999% Sn shot. For Al the B12A–3x.025W[17] baskets were used while for Sn the S19B–TA[17] boats were used.

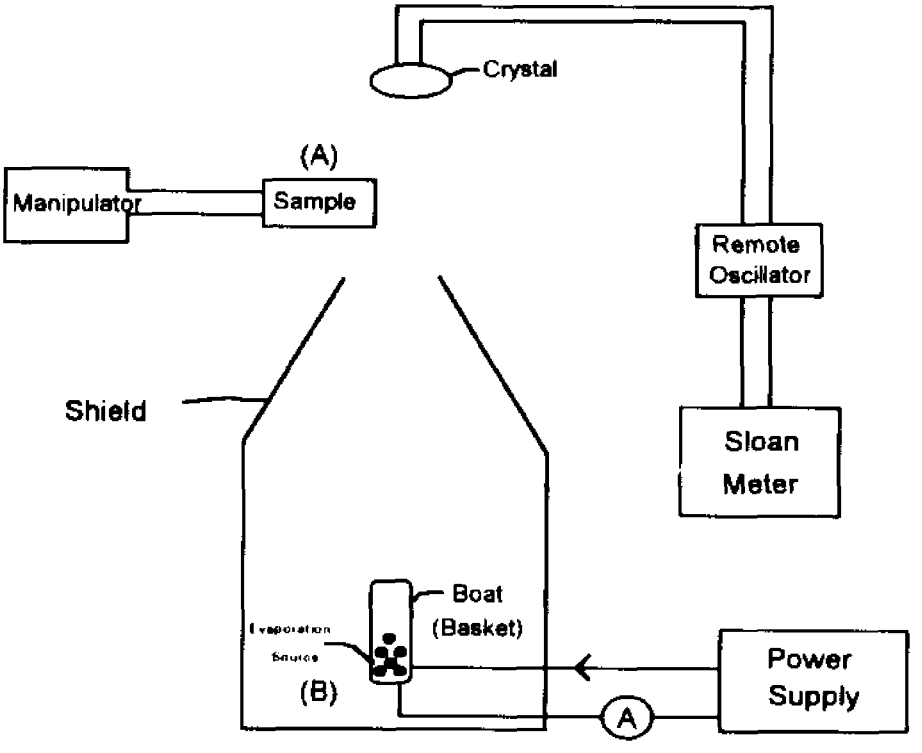

Figure 3. Schematic diagram of thermal evaporation.

Table 1. Typical thermal evaporation conditions

Substrate	Evaporate Source	Rate(Å/s)	Current (A)†
Nb	Al	0.2 - 0.3	48
Nb	Sn	0.1 - 0.2	110
Mo	Sn	0.1 - 0.2	100
Ta	Sn	0.1 - 0.2	105

The film thickness was measured by the Sloan meter that functions by measuring the change of the frequency caused by the growth of evaporation material on the crystal head (5 MHz, Plano Convex, gold coated crystal was used). When an AT-cut crystal is placed in the feedback path of an electronic oscillator, mechanical oscillation in the shear mode occurs. The frequency of oscillation is determined by the thickness of the crystal and the electromechanical characteristics of quartz. By Behrndt et al[18], when a quartz crystal is excited to thickness-shear oscillations, the plate's thickness corresponds to a half-wavelength of the fundamental frequency:

$$f = \frac{v_u}{2\tau} = \frac{C'}{\tau} \qquad (2.2.1)$$

Where v_{tr} is the velocity of the elastic transverse wave in the direction of the plate thickness τ and C' is the frequency constant.

† Boat or basket heating current.

Let Δm and ρ, respectively, denote the mass and density of the thin film, one has

$$\Delta m = \rho A \cdot \Delta \tau \tag{2.2.2}$$

with A be the area of the plate and $\Delta \tau$ be the thin film thickness. Expressions (2.2.1) and (2.2.2) yield:

$$\Delta m = -C \frac{\rho A}{f \cdot f_o} \Delta f \tag{2.2.3}$$

where f_o, f and Δf is, respectively, the starting, ending frequency and the frequency change. Hence a change in mass of the crystal due to the deposition of a thin film can be determined from the frequency shift.

To study the growth mechanism of an adsorbate metal B on a substrate metal A, first I moved A into a position, P_{AES}, where the AES signal taken was the highest, then the sample A was rotated to a position, P_{EVP}, where the whole sample was exposed to the evaporation vapor flux of adsorbate B, as demonstrated in figure 3. Positions P_{AES} and P_{EVP} were marked as accurate as possible for later reference. After the initial evaporation the sample was rotated back to position P_{AES}, then both AES and EELS measurements were taken. Later the sample was moved back to the position P_{EVP} for the next evaporation. The procedures were repeated until all desired evaporation and measurements were done. The films were deposited at typical rate 0.1 or 0.2 Å/s in stages; in each stage I registered the film thickness, the Auger spectra of both adsorbate and substrate and the EELS spectra of the film.

After the evaporation of the adsorbate B on the substitute A, I studied the annealed B/A surface to get more information about the film structure and the possibility of alloying. The thin film B/A was annealed at stepwise increasing

temperatures guided by readings from the thermocouple. During the annealing the sample was maintained in the same position.

2.2.4 Spectroscopy

After careful outgassing of all components the base pressure of the UHV system was in the low 10^{-9} Torr range. The sample's position was fine adjusted until the signal of the first plasmon loss peak of EELS reached its maximum where the primary energy and beam current were usually set to 500 eV and ~15 μA. In order to detect the build up of the impurities such as C and O during the measurements, the sample was continually monitored by taking the impurities' Auger signal. For AA–t measurements the substrate specimen was rotated on a manipulator between the position for deposition and the position for AES measurement. To minimize scatter in the data, these positions had to be precisely located by marking down the readings of the manipulator's scales. Changes of the Auger signals of both adsorbate and substrate during the process of thin film growth enable one to draw the AA–t plot that in turn will be used to determine the film growth mechanism[19-22], besides it also yields information which can be used to calculate Auger electron's IMFP (inelastic mean free path)[23-25]. In case of the annealed A/B system, at each different heating conditions, both materials A and B's Auger finger prints were taken as well as the film's plasmon loss spectrum. For the study of plasmon loss peak intensity versus the primary energy, the sample was fixed so that the geometry factor and its influence on the peak intensities can be eliminated.

2.3 Electron Energy Spectrum

2.3.1 Auger Electron Spectroscopy

In this thesis the Auger spectra were taken in the second derivative mode. Due to the small signal and steeply sloping background the Auger peaks are very difficulty to observe in the ordinary counting mode. Instead by superimposing a modulation on the scan energy, the more useful differential form of Auger spectrum is obtained. If the perturbing voltage applied on the analyzer energy is: $\Delta E = k \sin \omega t$, the collected electron current is[26]:

$$I(E + \Delta E) = I(E) + I'\Delta E + \frac{1}{2!}I''\Delta E^2 + \frac{1}{3!}I'''\Delta E^3 + \frac{1}{4!}I''''\Delta E^4 + \cdots$$

or $$I = I_0 + \left(I'k + \frac{3}{8}I'''k^3\right)\cdot \sin \omega t - \left(\frac{1}{4}I''k^2 + \frac{1}{48}I''''k^4\right)\cdot \cos 2\omega t + \cdots \qquad (2.3.1)$$

when the modulation voltage ΔE is small, the higher-order terms ($> k^3$) can safely be neglected, so we have:

$$I = I_0 + I'k \sin \omega t - \frac{1}{4}I''k^2 \cos 2\omega t + \cdots \qquad (2.3.2)$$

Let V be the voltage applied to the grids of the retarding field analyzer, then only the elections with energy higher than $E = eV$ can passing through the retarding field to contribute to the collected current. This gives the current:

$$I(E) \propto \int_{eV}^{\infty} N(E')dE' \qquad (2.3.3)$$

where N(E) is the energy distribution function of the electrons.

From equation (2.3.3) we therefore have:

$$N(E) \propto I'(E) \tag{2.3.4}$$

From equation (2.3.2), the energy distribution N(E) can be obtained by tuning the lock-in amplifier to the modulating frequency ω. Similarly by tuning to the second harmonic 2ω, the derivative Auger spectrum dN(E)/dE is obtained as follows:

$$N'(E) \propto I''(E) \tag{2.3.5}$$

In our laboratory we detect the second harmonic 2ω and therefore get the derivative Auger spectra dN(E)/dE. Most peaks in the N(E) curve have a low energy tail, while the position of the peak is more readily seen on the N'(E) curve[27,28]. The AES measurements were taken in the dN(E)/dE form with a primary energy and current of 2 KeV and ~ 45 μA. The peak to peak modulation voltage was 2 V.

2.3.2 Plasmon Loss Spectroscopy

Plasmon loss features are well known in electron spectroscopy, and have been extensively observed not only by X-ray Photoelectron Spectroscopy (XPS), but also by Electron Energy Loss Spectroscopy (EELS) and Auger Electron Spectroscopy (AES) since the primary theoretical work of Pines and Bohm[29-32]. By looking at the nature of these plasmon excitations, one may gain deeper understanding of the photoionization mechanism, and of the electron scattering in matter. In the EELS experiment the so called extrinsic excitation of the plasmon occurs during the transport of the electron through the solid, while in the XPS and AES experiments, the other kind of plasmon excitation – the so called intrinsic

excitation takes place simultaneously with the creation of the holes. Attekum et al[33] had shown that in the EELS extrinsic excitation process, the surface plasmon loss especially the very first one has higher intensity than in the XPS spectra. Another parameter effecting the relative intensities of plasmon loss is the electrons incident energy, i.e., with the higher primary energy the relative intensity will increase for the bulk plasmon loss and decrease for the surface plasmon loss. To select a suitable primary electron energy requires a balance between these two and also some practical limitations such as the electron gun currents. From our experience we find out that the 500~700 eV energy range is nice for our laboratory, a typical set for the plasmon loss spectrum is E_i = 500eV and I ~ 15μA.

One way most widely used in checking the cleanness of a surface is to take the AES finger prints of the possible impurities. The other way used to check the build up of the impurities, especially O and C, is to take the spectrum of the surface plasmon. Since, if the surface oxide forms during the measurements, the surface plasmon peak will show an energy shift. For example, aluminum's surface plasmon loss will show an energy shift from 10.2 eV down to 7.1 eV in the presence of the oxide and similar effect for other metals[29,34-36]. The details of this kind of shift are discussed in later section 3.2 to avoid duplications. Overall both the Auger finger print and the plasmon energy shift will tell us the same story.

2.4 AELAS

(Auger Electron Lab Analysis System)

The software AELAS was designed in the pop-up menu fashion for easy use. AELAS' main task is to save the original spectrum in digital form (it can save up to 10,000 points in floating number format). AELAS was written and complied in Turbo C++ [14]. AELAS accesses the LabMaster interface board via subroutine calls to LabPac[13]. LabPac is a low level software driver which is memory resident. Instead of giving a full description of AELAS, following is just a brief discussion about its analog to digital converter (ADC). An important thing which needs our special attention was matching the AES system's sweep-speed and the sampling rate of the digital data. It is obvious that there is always the danger for an overrun to occur when sampling the data, where overrun means that when the process context calculates it is time to begin sampling the next data and the previous sampling is still in process. It takes approximately 90 μs to serve one hardware interrupt by the combined efforts of the CPU, the main LabPac service routine and one process context. By taking into account the time needed by the program, we use 800 μs for the minimum time interval of one complete service cycle (Service Cycle Interval = 4 * Interrupt Interval). That in turn gives us the condition (2.4.2) for the time consideration of sampling data. In the calculation part (not shown) that we did, let *t_sweep* be the time needed for a sweep, and *n_point* be the total number of points to be saved for the sweep. The *period*, *source*, and *skip* are integer variables introduced from LabPac. The problem is to find out the right combination(s) between *skip*, *period*, *source*, *t_sweep*, and *n_point*, so that the following relationship between them will hold:

$$t\_sweep = n\_point \times 4 \times skip \times (period \times 10^{source\ -11}) \quad (2.4.1)$$

where $(period \times 10^{source\ -11})$ is the interrupt interval. Besides, they are also bounded by the following conditions:

$$period \times 10^{source\ -11} > 200\,\mu s \quad (2.4.2)$$

$$11 \le source \le 15 \quad (2.4.3)$$

$$1 \le period \le 2^{15} \quad (2.4.4)$$

$$1 \le skip \le 65{,}535 \quad (2.4.5)$$

Another extra practical condition introduced by our energy sweeper generator is that the *t_sweep* must be: 0.5, 1.5, 5.0, or 15 minutes. The possible combinations satisfy the conditions (2.4.1)–(2.4.5) are listed in table 2. The final value chosen for *source*, *period* is 11 and 625.

Table 2. Parameters used in AELAS to determine the *skip*

Parameters	Combinations
source	11
period	625
n-point (in thousand)	2k, 4k, 6k, 10k
t-sweep (in minute)	0.5, 1.5, 5.0
n-multiplier ≡ n-point/1,000	2, 4, 6, 10
t-multiplier ≡ t-sweep/0.50	1, 3, 10
skip (if n-multiplier =10)	10×(t-multiplier/n-multiplier)
skip (if n-multiplier = 12)	12×(t-multiplier/n-multiplier)

The next thing we need to take care with was the precision of the digits saved in AELAS. What we let the AELAS do is first read a data, checks its range, then chooses a suitable gain for that data. By doing this AELAS will not lose digit(s) due to the change of the data's scale. The last thing was certainly the time consuming job – write the codes and debug them until they work.

2.5 Smoothing

2.5.1 Digital Filters

A principal concern in practical Auger spectroscopy is to keep or to improve the quality of the recorded electron spectrum while performing the analysis quickly. Smoothing digital filters are valuable tools for improving the signal-to-noise ratio of spectrometric measurements[37]. Several methods of smoothing fluctuating data are available; one way used in AELAS is the moving average. In this method, one takes a fixed number of points, sum their values together, then divides by the number of points to obtain the average value at the center of the group. To calculate the next average value, the point at one end of the previous group is dropped, then the next point is added at the other end of the group, and the process repeated until all the points are visited. This method is not the most powerful technique, but it is simple and it is clear and easy to program. It is noticed that the end-points need a separate consideration.

2.5.2 Polynomial Digit Filter

Another commonly used method for digital filtering is that of least squares. Described by Savitzky and Golay[15], the finite polynomial filters are especially suitable to all types of spectrometry; they conserve area, symmetry, line position (for symmetric lines), and higher moments while yielding a signal-to-noise improvement that can be near the theoretical limit of the matched filter.

In this method a set of points is to be fitted to some curve described by a polynomial equation, the coefficients of this equation are to be selected such that when each abscissa point is substituted into this equation the square of the differences between the computed numbers and the original numbers (data) is a minimum for the total of the observations used on determining the coefficients. Savitzky and Golay did the detailed calculations and proposed a series of numerical tables for the smoothing of experimental data and for the computation of the derivative. The Savitzky-Golay convolution smoothing technique is based on fitting an array of $2m+1$ equally spaced data points $(x_{-m}, y_{-m}), \cdots (x_0, y_0), \cdots (x_m, y_m)$ to a polynomial of degree n, $(n < 2m+1)$[38]:

$$P(x) = c_0 + c_1(x - x_0) + c_2(x - x_0)^2 + \cdots + c_n(x - x_0)^n \qquad (2.5.1)$$

Then the smoothed value $\overline{y_0}$ of the group at the center point is the value given by the polynomial at point $x = x_0$, i.e.,

$$\overline{y_0} = P(x = x_0) = c_0 \qquad (2.5.2)$$

The objective of the digital least-squares-fit convolution procedure is thus the determination of a set of $n+1$ coefficients, $\{c_i\}$, such that the sum of the errors at each of the observation points, E, will be minimized, where E is defined as follows:

$$\mathrm{E} \equiv \sum_{i=-m}^{i=m} \left[y_i - P(x_i) \right]^2 = \sum_{i=-m}^{i=m} \left[y_i - \left(c_0 + c_1 (x_i - x_0) + \cdots + c_n (x_i - x_0)^n \right) \right]^2 \qquad (2.5.3)$$

To minimize E with respect to the coefficients $\{c_i\}$, differentiating E with respect to each c_i and setting the result equal to zero gives us the following $n+1$ equations:

$$\frac{\partial \mathrm{E}}{\partial c_k} = -2 \sum_{i=-m}^{i=m} \left[y_i - \left(c_0 + c_1 (x_i - x_0) + \cdots + c_n (x_i - x_0)^n \right) \right] (x_i - x_0)^k = 0,$$

$$\text{where } (k = 0, 1, 2, \cdots n) \qquad (2.5.4)$$

Solving equations (2.5.4) for the coefficients $\{c_i\}$, especially the c_0, and using expression (2.5.2) one has the smoothed value at the center point:

$$\overline{y_0} = c_0 = \sum_{s=-m}^{m} p_s y_s \qquad (2.5.5)$$

General formulae for the coefficients p_s for fitting to polynomials of degree 2 to 5, as listed below, have been derived by several authors[39]. For quadratic or cubic fits the formula is:

$$p_s = \frac{3(3m^2 + 3m - 1 - 5s^2)}{(2m+3)(2m+1)(2m-1)} \qquad (2.5.6)$$

and for quartic or quintic fits the formula is:

$$p_s = \left(\frac{15}{4}\right) \frac{(15m^4 + 30m^3 - 35m^2 - 50m + 12) - 35(2m^2 + 2m - 3) \cdot s^2 + 63s^4}{(2m+5)(2m+3)(2m+1)(2m-1)(2m-3)} \qquad (2.5.7)$$

The corresponding coefficients for quadratic (101 points) are listed in Table 3. In AELAS both quadratic- and quartic-smooth is available.

By analyzing the effects of single least-squares-fit smoothing on noise-free Gaussian lines Willson and Edward[39] have found that the optimum width of the

smoothing array is 1.4 times the full width at half maximum (FWHM) of the narrowest Gaussian line of their spectra. In a similar analysis considering Lorentzian-shaped as well as Gaussian-shaped lines, Enke and Nieman[40] conclude that the best signal-to-noise enhancement from a single-pass (quadratic-cubic) smoothing occurs for a smoothing array that is twice as wide as the FWHM of the peak being smoothed.

To check the effect of polynomial smooth built in the AELAS; we took an Auger electron spectrum of clean niobium as our original raw data. After adding random noises with different levels to the original raw data, we smooth the noise-added data. The effects of the polynomial filter on improving the signal-to-noise ratio of spectrometric measurements are shown in figure 4. In the figure, series curves (a), (b), and (c) represent the raw data, noise added data and noise added data after smooth respectively. The smooth is an 101-point quartic one (smooth range of 101 point is ~1% of the full x-scale which is 10,000 points). Clearly the polynomial smoothes can move away the random noise (recover the raw data) if the noise level is reasonable low as shown in figure 4-1 (c), but the polynomial smoothes will fail to recovering the noise-added data when the noise level is too high as shown in figure 4-4 (c). Other intermediate noise levels are also shown in figure 4-2 and figure 4-3 for comparison. From above tests, by applying the polynomial filter to the spectrometric measurements we can improve the signal-to-noise ratio, or in another word, we do indeed clean up a dirty spectrum by removing the background noise. To make it unique, most of the spectra shown in this thesis are in their original form, i.e., the spectra without applying data filters. The spectra treated by the smooth technique are noted where they are given (examples: figure 4, 23, 24).

It is noticed that the smooths mentioned above do not work for the end-points, but since these end-points are only 0.1%~1.0% of the full scale, provided that the energy range of the data extends well beyond the features of interest there will not be any problems.

Table 3. Savitzky-Golay coefficients P_i (quadratic, an 101-point array)

P[0] = -0.014131	P[25] = 0.013178	P[50] = 0.022281	P[75] = 0.013178
P[1] = -0.012689	P[26] = 0.013892	P[51] = 0.022266	P[76] = 0.012435
P[2] = -0.011276	P[27] = 0.014576	P[52] = 0.022223	P[77] = 0.011663
P[3] = -0.009892	P[28] = 0.015232	P[53] = 0.022150	P[78] = 0.010862
P[4] = -0.008538	P[29] = 0.015858	P[54] = 0.022048	P[79] = 0.010032
P[5] = -0.007212	P[30] = 0.016455	P[55] = 0.021917	P[80] = 0.009173
P[6] = -0.005916	P[31] = 0.017023	P[56] = 0.021757	P[81] = 0.008284
P[7] = -0.004649	P[32] = 0.017562	P[57] = 0.021567	P[82] = 0.007367
P[8] = -0.003411	P[33] = 0.018072	P[58] = 0.021349	P[83] = 0.006420
P[9] = -0.002202	P[34] = 0.018552	P[59] = 0.021101	P[84] = 0.005444
P[10] = -0.001022	P[35] = 0.019004	P[60] = 0.020824	P[85] = 0.004439
P[11] = 0.000128	P[36] = 0.019426	P[61] = 0.020519	P[86] = 0.003405
P[12] = 0.001250	P[37] = 0.019819	P[62] = 0.020184	P[87] = 0.002342
P[13] = 0.002342	P[38] = 0.020184	P[63] = 0.019819	P[88] = 0.001250
P[14] = 0.003405	P[39] = 0.020519	P[64] = 0.019426	P[89] = 0.000128
P[15] = 0.004439	P[40] = 0.020824	P[65] = 0.019004	P[90] = -0.001022
P[16] = 0.005444	P[41] = 0.021101	P[66] = 0.018552	P[91] = -.002202
P[17] = 0.006420	P[42] = 0.021349	P[67] = 0.018072	P[92] = -0.003411
P[18] = 0.007367	P[43] = 0.021567	P[68] = 0.017562	P[93] = -0.004649
P[19] = 0.008284	P[44] = 0.021757	P[69] = 0.017023	P[94] = -0.005916
P[20] = 0.009173	P[45] = 0.021917	P[70] = 0.016455	P[95] = -0.007212
P[21] = 0.010032	P[46] = 0.022048	P[71] = 0.015858	P[96] = -0.008538
P[22] = 0.010862	P[47] = 0.022150	P[72] = 0.015232	P[97] = -0.009892
P[23] = 0.011663	P[48] = 0.022223	P[73] = 0.014576	P[98] = -0.011276
P[24] = 0.012435	P[49] = 0.022266	P[74] = 0.013892	P[99] = -0.012689
			P[100] = -0.014131

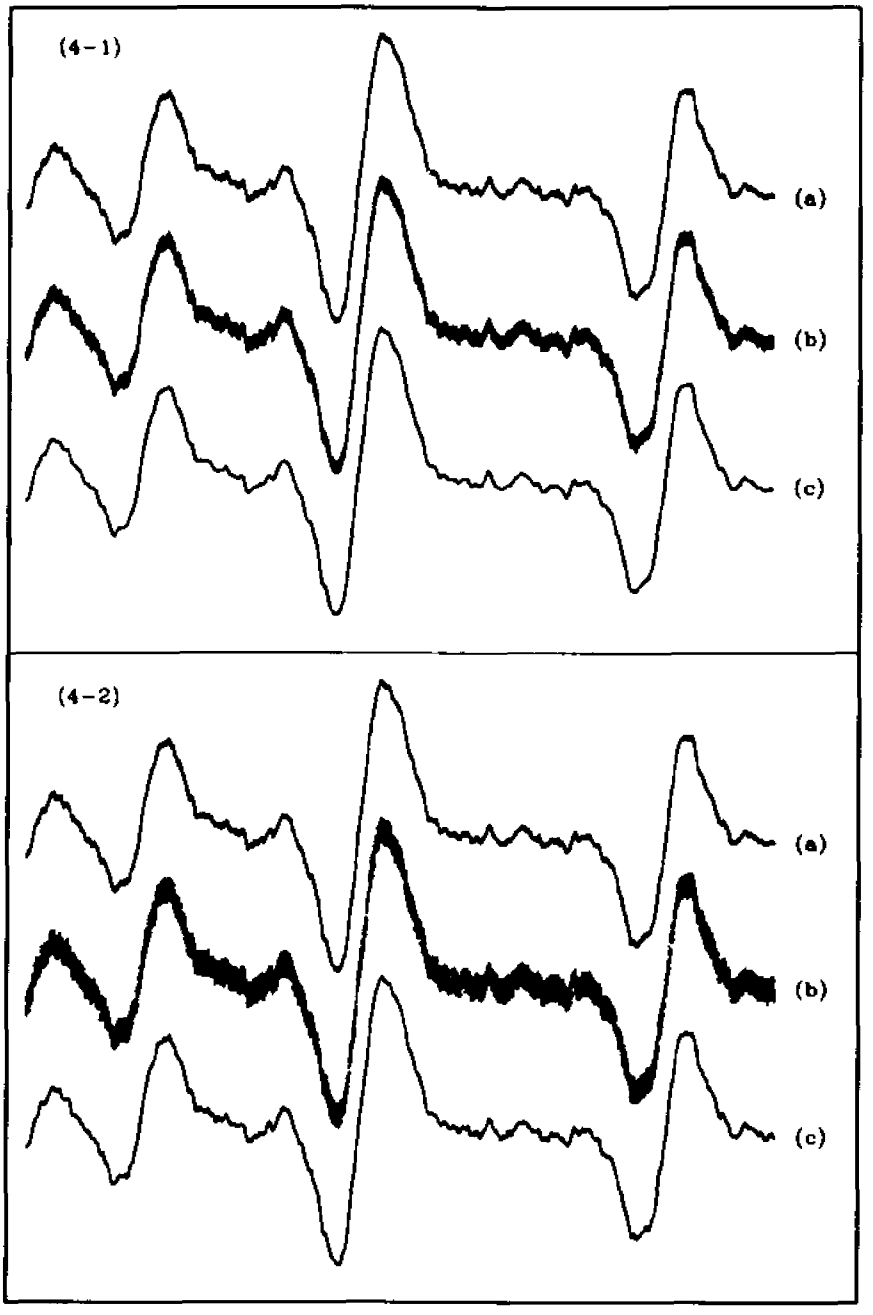

Figure 4. Smooth effect on random noise: (a) original raw data, (b) noise-added data, (c) noise-added data after an 101-point quartic smooth.

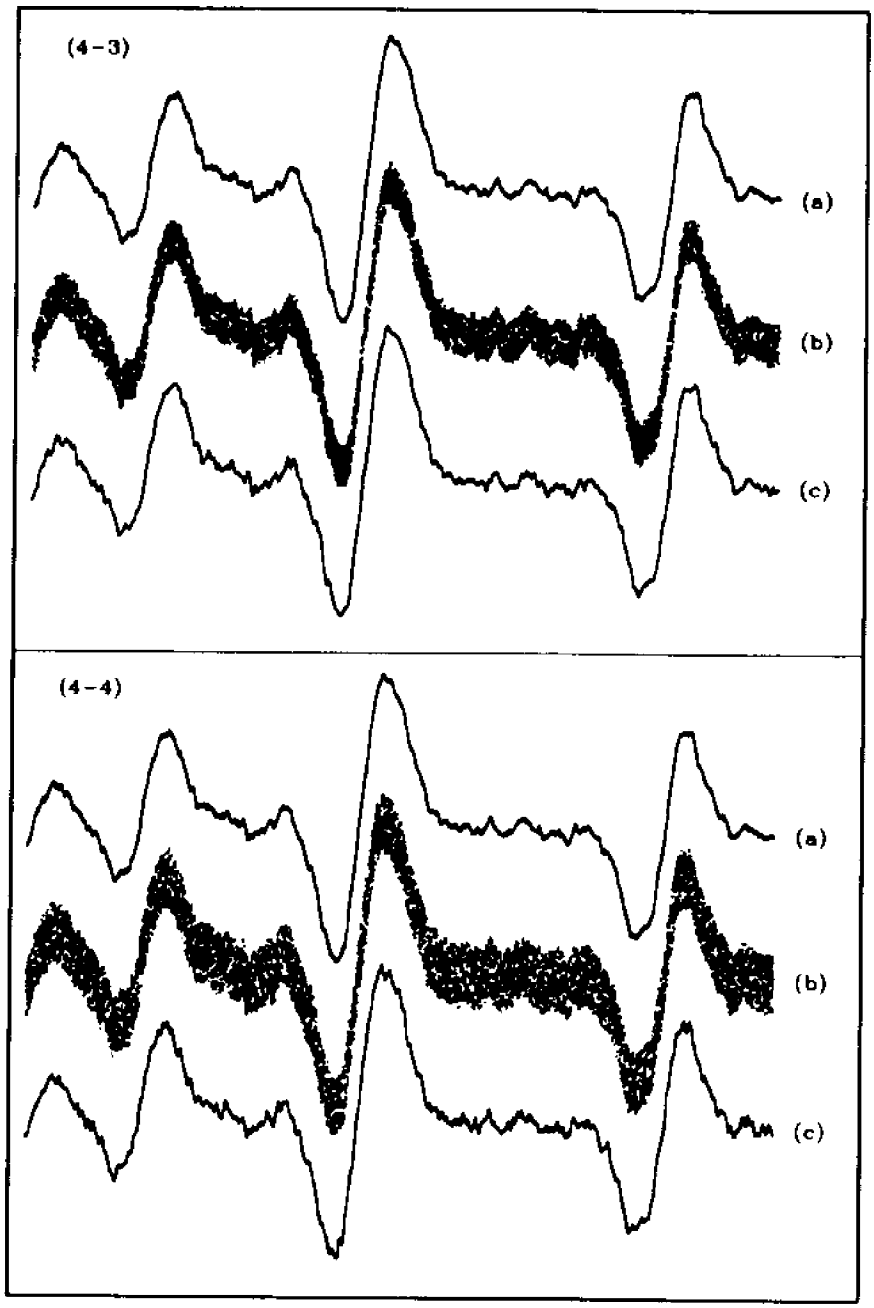

Continued from figure 4.: (4-3) and (4-4).

Chapter 3. Theory

3.1 Auger Electron Spectroscopy (AES)

Auger electrons were first discovered in 1925 by Pierre Auger who saw their tracks in a Wilson Cloud Chamber and explained their origin[1]. Auger Electron Spectroscopy has emerged as one of the most sensitive methods of surface analysis and has been widely accepted due to the relative simplicity of the LEED-Auger and cylindrical mirror analyzers (CMA). The method has found widespread application in the fields of metallurgy, semiconductor technology, thin film analysis, and fundamental surface physics.

Auger electron spectroscopy is accomplished by irradiating the surface of a solid with a primary electron beam while energy analysis is performed on the resultant secondary electrons. An initial core hole in a shell or subshell (energy E_v) created either by incident photons or electrons may be filled with electrons from an outer shell (energy E_x). The two possible filling processes are photon emission and Auger emission as shown in figure 5. In the photon emission, photons with energy $\hbar\nu = E_v - E_x$ are emitted, while in the Auger emission, the energy released is transferred via the electrostatic interaction to another bound electron (energy E_y) that then escapes from the atom. This outgoing election, the so called Auger electron, has an energy of:

$$E_{Auger} = E_v - E_x - E_y - I \qquad (3.1.1)$$

where I is the hole-hole interaction energy and E_v, E_x, and E_y are the normal one-electron binding energies. These are usually taken to be those measured in XPS

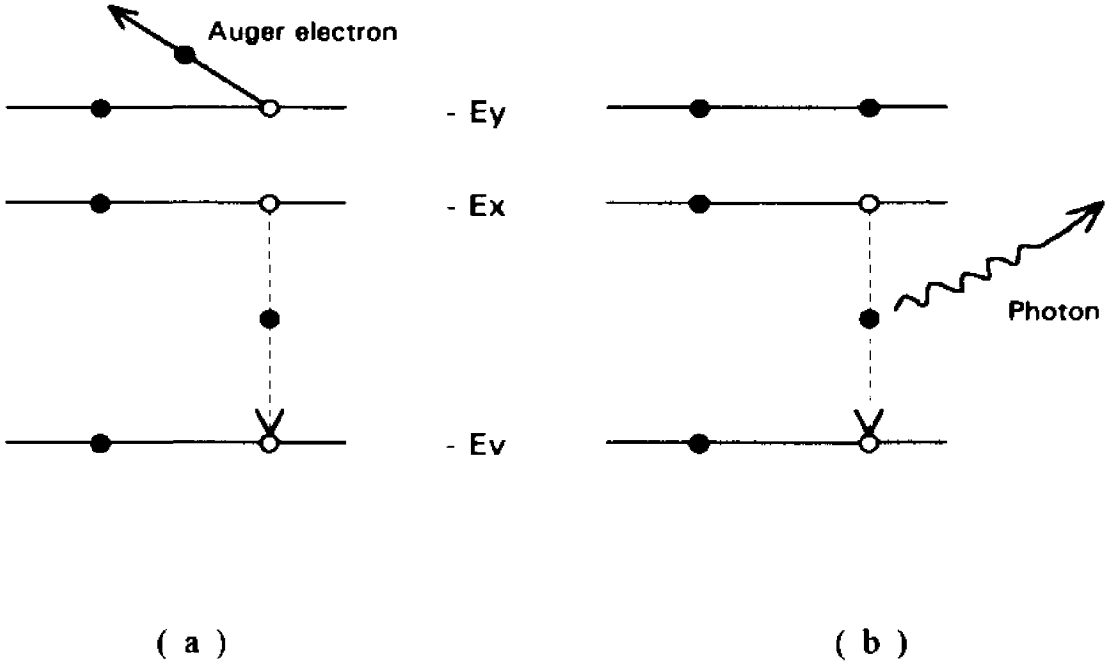

Figure 5. Two possible processes for filling an inner shell electron vacancy: (a) Auger emission, (b) photon emission.

(X-ray Photoelectron Spectroscopy) and therefore include one-hole relaxation effects already. The I, therefore, lumps together the two-hole energy effects within the material under study. It may be divided into two terms:

$$I = H - S \qquad (3.1.2)$$

where H is the hole-hole interaction energy in the free atom and S takes account of the screening polarization or relaxation effects of the solid state environment. The Auger electron energy is directly related to core levels of the parent atom; it is dependent only on the energy levels of the atom and does not depend on the energy of the electron that caused the initial ionization. In the Auger radiationless de-excitation process, the atom is left in the final state with two holes (vacancies), if one of the final state holes lies in the same shell as the primary hole (although not in the same subshell) the transition is referred to as a Coster-Kronig[27,41] transition. The number of core-holes produced due to the electron impact in the various subshells of the same shell is proportional to their occupation number; for example, the initial distribution of core holes in the L-shell should be around 1:1:2 for $2s:2p_{1/2}:2p_{2/3}$. Due to the fact that the Coster-Kronig satellite process involves migration of core-holes between the subshells and therefore changes the core-hole distribution and to the fact that its transition rates are much higher than the normal Auger transitions, the Coster-Kronig transition is significant and influences the relative intensities of the Auger lines. As shown in figure 6, if an L_1 shell has a vacancy, the L_2 to L_1 transition (Coster-Kronig) will be rapid thereby reducing M electron to L_1 vacancy.

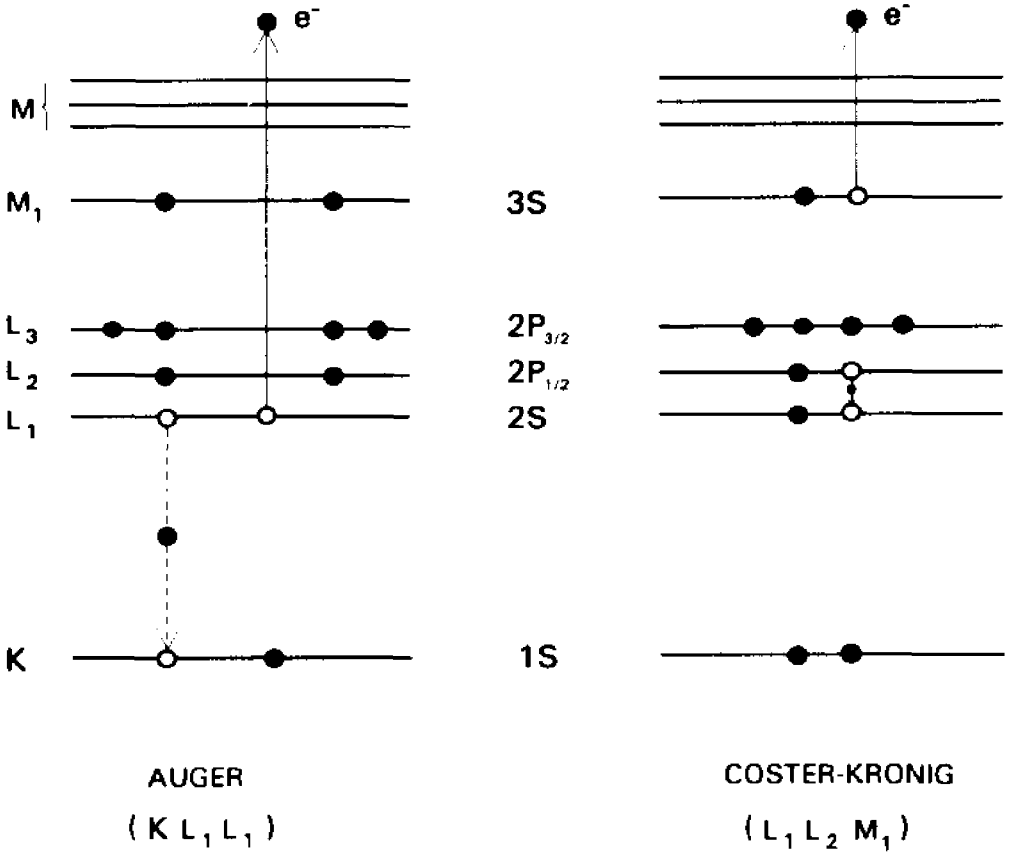

Figure 6. Normal Auger emission and Coster-Kronig process.

3.2 Plasmons

Plasmons are quantized oscillations in the density of an electron gas. They were discovered in ionized gases by Langmuir[42]. Such oscillations can be excited by shooting in a photon or a charged particle. When electrons pass through or reflect from a thin film, the reflected or transmitted electrons may show an energy loss equal to integer multiples and combinations of the plasmon energies. The plasmon energies depend upon the density of the electron gas and whether they are three dimensional fluctuations – the bulk plasmons, or two dimensional fluctuations at the surface – the surface plasmons, or localized fluctuations at an interface – the interface plasmons.

The frequency dependent dielectric constant $\varepsilon(\omega,k)$ is used to describe the dynamic electrical properties of a medium. Let ω_p denote the frequency determined by:

$$\omega_p = \left(4\pi N e^2 / m\right)^{1/2} \tag{3.2.1}$$

where m, e is the electron mass and charge respectively and N is the free electron's density. Derived by Nozieres Pines[43] the electrons' inelastic scattering from a solid can be expressed in terms of $\varepsilon(\omega,k)$, which is a complex frequency-dependent function, as follows:

$$\varepsilon(\omega,0) = 1 - \frac{f_0\omega_p^2}{\omega^2 - i g_0 \omega} - \omega_p^2 \cdot \sum_{j=1} \frac{f_j}{\omega^2 - \omega_j^2 - i g_j \omega} \tag{3.2.2}$$

where ω_p is the frequency given by (3.2.1), f_0 is the oscillator strength that describes the free-electron contribution to $\varepsilon(\omega,0)$ and g_0 is the reciprocal of the relaxation time. The last sum-term in (3.2.2) is due to the contributions of

interband transitions of frequency ω_j with oscillator strength f_j and damping constant g_j of the j-th interband transition. The f_j's follow the sum rule of the oscillator strengths:

$$\sum_{j=0}^{\infty} f_j = 1 \tag{3.2.3}$$

The imaginary part of $\varepsilon(\omega,0)$ is simply a measure of the number of states available for real transitions. For free-electron metals, $\omega << \omega_j$ when $\omega \cong \omega_p$, therefore the last term of expression (3.2.2) is negligible small; then the dielectric constant $\varepsilon(\omega,0)$ of the free electron gas is obtained as:

$$\varepsilon \equiv \varepsilon(\omega,0) = 1 - \frac{\omega_p^2}{\omega^2 - i g_0 \omega} \tag{3.2.4}$$

or: $$\varepsilon(\omega) = 1 - \frac{\omega_p^2}{\omega^2} + \left[\left(\frac{\omega_p^2}{\omega^4 \tau^2} - \frac{\omega_p^2}{\omega^6 \tau^4} + \cdots\right) - i\left(\frac{\omega_p^2}{\omega^3 \tau} - \frac{\omega_p^2}{\omega^5 \tau^3} + \cdots\right)\right]$$

where $\tau^{-1} \equiv g_0$ is the damping rate. The last term of the above expression is small for free electrons. The expression therefore becomes the well-known free electron dielectric constant relationship:

$$\varepsilon(\omega,0) = 1 - \frac{\omega_p^2}{\omega^2} \tag{3.2.5}$$

It is well known[142] that the condition for a bulk plasmon resonance occurs for a frequency ω at which $\varepsilon(\omega) = 0$, then the electron energy loss due to the excitation of the bulk plasmon can be easily gotten from equation (3.2.1) and (3.2.5):

$$\Delta E_b = \hbar\omega_p = \hbar\sqrt{\frac{4\pi N e^2}{m}} \tag{3.2.6}$$

For calculation of the surface plasmon energy, consider a semi-infinite electron gas terminated in a plane surface and use the dispersion relationship for the dielectric constant of the free electron gas (3.2.5), one can solve the Laplace's equation by applying the electromagnetic boundary conditions at the surface–vacuum interface, i.e., that the normal component of the electric displacement vector should be continuous at the interface, one obtains the following equation:

$$\varepsilon(\omega,0) = -1 \tag{3.2.7}$$

From equations (3.2.5) and (3.2.7) the energy lost due to the excitation of a surface plasmon is obtained[44]:

$$\Delta E_s = \hbar\omega_s = \frac{1}{\sqrt{2}}\hbar\omega_p = \frac{1}{\sqrt{2}}(\Delta E_b) \tag{3.2.8}$$

For an even more general case, consider the metal is not bounded by the vacuum any more, but by a dielectric medium with the dielectric constant ε, for example, an oxide layer above the metal. The following formula will then be obtained for the energy loss due to the excitation of a surface plasmon:

$$\Delta E_s = \frac{1}{\sqrt{1+\varepsilon}}\hbar\omega_p = \frac{1}{\sqrt{1+\varepsilon}}(\Delta E_b) \tag{3.2.9}$$

Similarly, by applying the electromagnetic boundary conditions at the plane $Z = 0$ between metal 1 at $Z > 0$ and metal 2 at $Z < 0$ one has the energy lost due to the excitation of an interface plasmon:

$$\Delta E_i = \sqrt{\frac{1}{2}\left[(\hbar\omega_{p1})^2 + (\hbar\omega_{p2})^2\right]} = \sqrt{\frac{1}{2}\left[(\Delta E_{b1})^2 + (\Delta E_{b2})^2\right]} \tag{3.2.10}$$

where ΔE_{b1} and ΔE_{b2} denote the bulk plasmon energy of metal 1 and metal 2 respectively. From the above formulae, metals with conduction band electron densities in the range of 10^{27}~10^{29} electrons/m^3 will show plasmon losses in the order of a few electron volts. The exciting particle may generate more than one plasmon as it passes through the solid and so suffers multiple plasmon losses. Table 4 lists some metals' plasmon loss energies calculated by using above formulae (assuming that the *s*- and *d*-band electrons are free).

Table 4. Predicted plasmon energies (eV)

Part 1: bulk and surface plasmon energies

Material	Bulk Plasmon	Surface Plasmon
Nb	19.6	13.9
Mo	23.1	16.3
Ta	19.6	13.9
Sn	12.7	8.96
Al	15.8	11.2

Part 2: interface plasmon energies

Al/Nb	Sn/Nb	Sn/Mo	Sn/Ta
17.8	16.5	18.6	16.5

Now let us take a look of an interesting case of the metal–thin-film–vacuum sandwiches. Consider a semi infinite metal in the half space of $z \le 0$ with a thin film layer in the region of $0 \le z \le \tau$ and the vacuum in the region of $z \ge \tau$, (the so called step-function), let $\hbar\omega_m$ and $\hbar\omega_1$ denote the bulk plasmon energy of the substrate metal and the thin film respectively as defined in equation (3.2.6); then the two dielectric functions are:

$$\varepsilon_m \equiv \varepsilon(\omega,0) = 1 - \frac{\omega_m^2}{\omega^2} \qquad \text{and} \qquad \varepsilon_1 \equiv \varepsilon(\omega,0) = 1 - \frac{\omega_1^2}{\omega^2} \tag{3.2.11}$$

The electric scalar potential distribution set up by a classical charge wave bound to the interfaces must be zero at infinite distance and satisfy the Laplace's equation within the substrate metal and the thin film. Let's use the Cartesian coordinates x and y parallel to the interfaces and z normal to them; therefore the electric potentials in the three regions must have the forms:

$$\psi_m(x,z,t) = \cos(kx - \omega t)(Ae^{kz}), \qquad z \le 0$$

$$\psi_1(x,z,t) = \cos(kx - \omega t)(Be^{kz} + Ce^{-kz}), \qquad 0 \le z \le \tau$$

$$\psi_v(x,z,t) = \cos(kx - \omega t)(De^{-k(z-\tau)}), \qquad z \ge \tau$$

where A is the amplitude of the running wave, k is its wave number, and B, C, and D are constants to be determined. At each interface, the boundary condition holds. At plane $z = 0$, the continuity of the transverse electric field,

$$\left.\frac{\partial \psi_m}{\partial x}\right|_{z=0} = \left.\frac{\partial \psi_1}{\partial x}\right|_{z=0}$$

gives: $$B + C = A \tag{3.2.12}$$

and the continuity of the normal electric displacement,

$$\varepsilon_m \left.\frac{\partial \psi_m}{\partial z}\right|_{z=0} = \varepsilon_i \left.\frac{\partial \psi_i}{\partial z}\right|_{z=0}$$

gives: $$B - C = \left(\frac{\varepsilon_m}{\varepsilon_i}\right) \cdot A \tag{3.2.13}$$

Similarly at plane $z = r$, the boundary conditions give:

$$Be^{kr} + Ce^{kr} = D \tag{3.2.14}$$

$$Be^{kr} - Ce^{kr} = -\frac{1}{\varepsilon_i} D \tag{3.2.15}$$

The four equations (3.2.12)–(3.2.15) can be used to determine the eigenvalues and the constants B, C, and D in terms of A. The eigenvalues are obtained

through: $$\frac{\varepsilon_m}{\varepsilon_i} = -\frac{1 - \gamma e^{2kr}}{1 + \gamma e^{2kr}} \tag{3.2.16}$$

and $$\gamma \equiv \frac{\varepsilon_i - 1}{\varepsilon_i + 1} \tag{3.2.17}$$

Combines (3.2.16) with (3.2.17) one has:

$$\omega^4 - \left(\frac{1}{2}\omega_m^2 + \omega_i^2\right) \cdot \omega^2 + \frac{1}{2} \cdot \left(\frac{1}{2}\omega_m^2\right) \cdot \omega_i^2 \cdot \left[\left(1 + \frac{\omega_i^2}{\omega_m^2}\right) + \left(1 - \frac{\omega_i^2}{\omega_m^2}\right) \cdot e^{2kr}\right] = 0$$

with the corresponding solutions:

$$\omega^2 = \left(\frac{1}{4}\omega_m^2 + \frac{1}{2}\omega_i^2\right) \pm \sqrt{\left(\frac{1}{4}\omega_m^2\right)^2 + \left(\frac{1}{2}\omega_i^2\right)^2 \cdot \left(1 - \frac{\omega_m^2}{\omega_i^2}\right) \cdot e^{2kr}} \tag{3.2.18}$$

Following are several limiting cases of the eigenvalues given by equation (3.2.18):

(i) Very thick- and thin-films.

In the thick film limit case, $e^{-2kt} \to 0$, equation (3.2.18) gives two solutions:

$$\omega_{(1)} = \frac{1}{\sqrt{2}}\omega_t \quad \text{and} \quad \omega_{(2)} = \sqrt{\frac{1}{2}\left(\omega_m^2 + \omega_t^2\right)}$$

These two eigenvalues, not surprisingly, are exactly the same as given by equations (3.2.8) and (3.2.10) where one is the surface plasmon loss of film–vacuum interface and the other is the interface plasmon loss of film–metal interface.

In the thin film limit case, $e^{-2kt} \to 1$, equation (3.2.18) gives us the following two eigenvalues:

$$\omega_{(1)} = \frac{1}{\sqrt{2}}\omega_m \quad \text{and} \quad \omega_{(2)} = \omega_t$$

These two eigenvalues also obtained from equations (3.2.8) and (3.2.6) one of those is the surface plasmon loss of the metal–vacuum interface and the other is just the bulk plasmon loss of the film.

(ii) Film bounded by a vacuum on both sides.

In this case, the $\varepsilon_m = 1$ then $\omega_m = 0$, so from equation (3.2.18) one has:

$$\omega_{(1),(2)} = \frac{1}{\sqrt{2}}\omega_t\left(1 \pm e^{-kt}\right)^{1/2} \tag{3.2.19}$$

These formulae obtained by Simmons and Scheibner[45] previously, predict the splitting of the surface plasmon loss due to the surface oscillation at the two boundaries.

So far we have considered only the nearly free electron approximation for $\varepsilon(\omega, k)$. Improvements in the theory require a treatment of the electron-electron interactions and the electron-ion interactions. The latter requires a band structure calculation to determine the last term in equation 3.2.2. Following for example

Ibach[46], the loss function $I(\omega,k)$ which describes the distribution of energy losses is:

$$I(\omega,k) \propto -\mathrm{Im}\left\{\frac{1}{\varepsilon(\omega,k)}\right\}, \qquad \omega > 0 \tag{3.2.20}$$

In the case of weak damping, inserting the expression (3.2.4) for $\varepsilon(\omega,k)$ for the free electron gas:

$$-\mathrm{Im}\left\{\frac{1}{\varepsilon(\omega,k)}\right\} = \frac{\pi}{2}\omega_p\,\delta(\omega-\omega_p) \tag{3.2.21}$$

It becomes clear that the loss function has a pole at ω_p which corresponds to the BP-loss, i.e., a pole at the plasmon frequency. The corresponding surface loss function is expressed as[46]:

$$I(\omega,k) \propto -\mathrm{Im}\left\{\frac{1}{\varepsilon(\omega,k)+1}\right\} \tag{3.2.22}$$

and the associated losses are the surface losses. For weak damping, the position of the pole in the loss function lies at $\mathrm{Re}\{\varepsilon(\omega)\} = -1$, which corresponds to the SP-loss condition[47]. Using this formalism, our earlier results for thin films can also be retraced[48]. The derivation of an exact formula for the dielectric function of a homogeneous electron gas (or Jellium) has not yet been accomplished[42]. Several approximate formulae, for example, the Lindhard[49] formula based on the RPA (random phase approximation) have been suggested and have been used to determine the corresponding loss functions[50].

3.3 Electron Inelastic Mean Free Path (IMFP)

When an electron passes through a solid it can have many ways of losing energy, the main processes are single-particle electron excitations and plasmon scattering if we neglect phonon scattering for the electron range ~ 50eV–2KeV. Theoretical calculation of the scattering cross section and the inelastic-mean-free-path (IMFP) have been performed usually for idealized free-electron materials. The so called universal curve, which is a plot of IMFP versus electron's kinetic energy as given in figure 7[51] (details about our data ★ are given in section 4.4) shows a broad minimum near 50 eV. That can be explained as follows. At lower energies the scattering is due to single-particle excitation's while as the energy increases (above the plasmon energy, typically ~ 15 eV) the scattering is dominated by plasmon creation due to the increase of the plasmon scattering cross section[52]. At higher energies both scattering cross sections decrease. The universality then becomes clear from the above mechanism of valence band electron excitation and the fact that electron density in the valence band is almost the same for most materials, which is about 0.25 electron/$Å^3$. However the scatter in the experimental data points shown in figure 7 probably does reflect the detailed material dependence.

The IMFP is given by[53]:

$$\lambda_{IMFP} = E_k / k M_1 \qquad (3.3.1)$$

where E_k is the electron energy, k its momentum, and

$$M_1 = \frac{e^2}{2\pi^2} \int \frac{d^3k}{k^2} \mathrm{Im}\left[\frac{-1}{\varepsilon(\omega,k)}\right] \qquad (3.3.2)$$

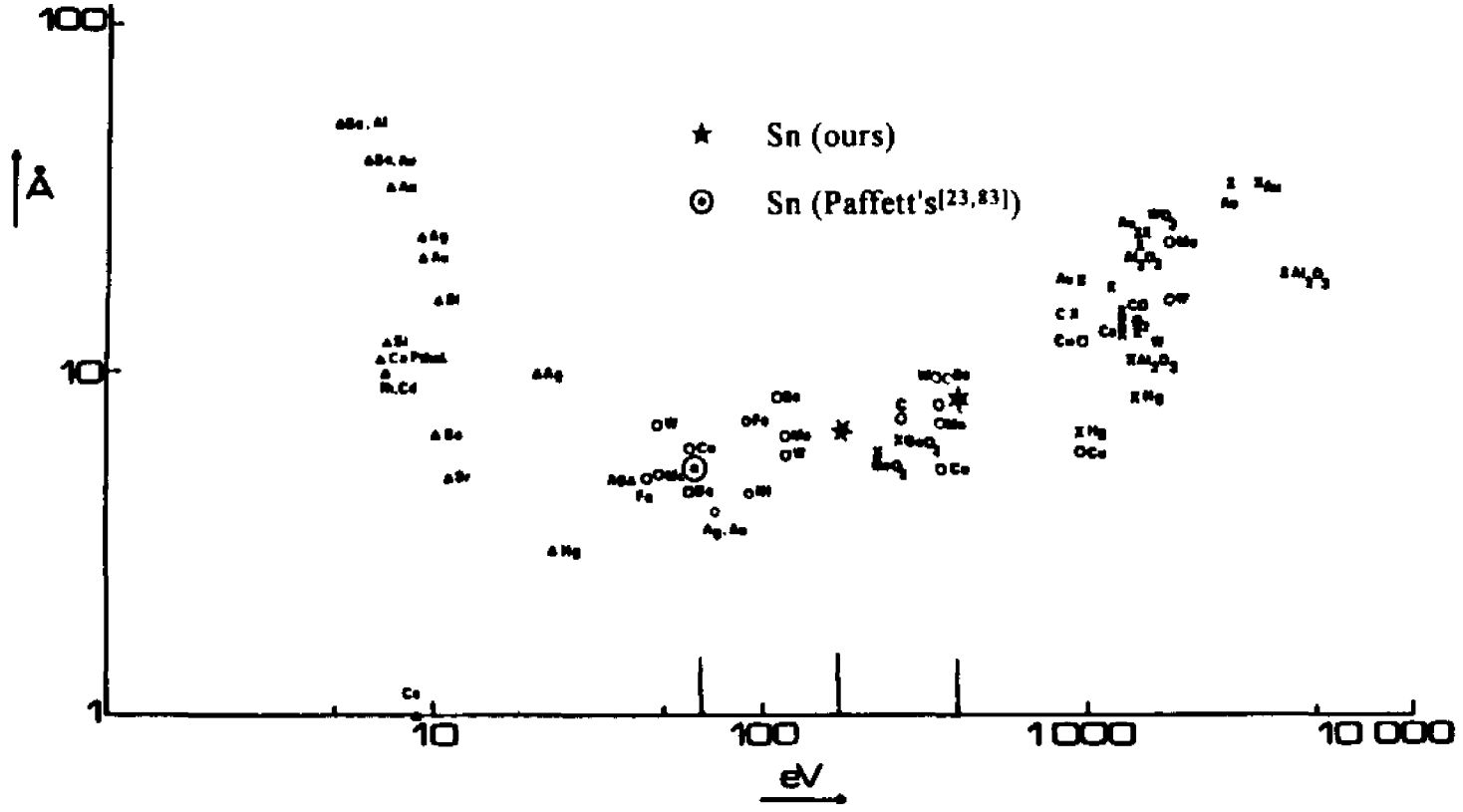

Figure 7. Experimental determinations of the IMFP (electron inelastic mean free path) in several materials. The symbols designate the experimental technique employed in obtaining each measurement: XPS(x), UPS(o), AES(Δ)[51].

In expression (3.3.2), $\varepsilon(\omega,k)$ is the complex dielectric constant which depends on momentum transfer k and energy loss $\hbar\omega = E_q - E_{q,k}$ in an inelastic scattering event. Tanuma et al[54,55] proposed a new general formula based on the RFA (random phase approximation) for the IMFP's for 200–2000 eV electrons in solids. Their calculations predict IMFP's of less than 30 Å. Overall the fact that IMFP's are only a few monolayers for the electrons energy range 50–2000 eV implies that electrons which escape must originate from and sample only a few layers close to the surface. Thus AES and EELS are very sensitive to the surface conditions and useful techniques in the surface study.

Another term often used interchangeably with the IMFP is the AL which has the same order of magnitude as the IMFP. The attenuation length (AL) is an experimental value derived from film overlayers. The attenuation in a layer of thickness d is $e^{-d/\lambda}$ where λ is the AL. The sampling depth of AES is determined by the escape depth of Auger electrons, which is the product of the AL and the cosine of the angle defined by analyzer direction and the surface normal. Seah and Dench[56] have made an analysis of AL measurements and proposed a relation between the electron energy, E_k, and the AL, as follows:

$$\lambda = \frac{538}{E_k^2}a + 0.41\sqrt{a^3 E_k} \qquad (3.3.3)$$

where a is the average monolayer thickness (in nm) defined by:

$$a = \left(10^{27} A / \rho n N_a\right)^{1/3} \qquad (3.3.4)$$

with the common materials constants: A is the molecular weight, n is the number of atoms in the molecule, ρ is the mass density and N_a is Avogadro's constant. From relation (3.3.1) it is clear that AL is in range of 4–20Å for the electrons'

kinetic energy in the range 50 eV to 2 KeV. Several authors[54,55] have pointed out that the IMFP may exceed the AL by about up to 30%, because the conditions close to the surface may differ from the environment in the interior. Nevertheless Tanuma et al[54,57] show that the formula proposed by Seah and Dench[56] gives results close to their and other calculations for energies less than about 500 eV.

3.4 Thin Film Growth Modes

In the range from submonolayer coverage to several monolayers, quantitative surface properties depend crucially on an accurate analysis of the adsorbed atoms, so it is important to distinguish the different possible growth modes of a thin film. Bauer[8] proposed a topological classification and the common three types of thin film growth modes are: (1) Frank-van der Merwe growth (layer-by-layer FM mode) in which the deposited film completes one monolayer of coverage, then the second, etc.; (2) Stranski-Krastanov growth (layer-plus-islanding SK mode) in which the first layer completely covers the surface of the substrate and subsequent layers from islands of deposited material; (3) Volmer-Weber growth (complete-islanding VW mode) in which the material immediately forms islands on the surface (figure 8). Consideration of the relative magnitudes of the adsorbate, substrate, and interfacial surface free energy leads to the above distinct growth modes[9]. To do so, consider the energy difference between the two epitaxial overlayer arrangements depicted in figure 8(b); let γ_o, γ_i and γ_s denote the surface free energy per unit area at the overlayer–vacuum interface, the overlayer–substrate interface and the substrate–vacuum interface, respectively. Without loss of generality, one may assume that the Volmer-Weber cluster occupies half the available surface area A. It follows immediately that:

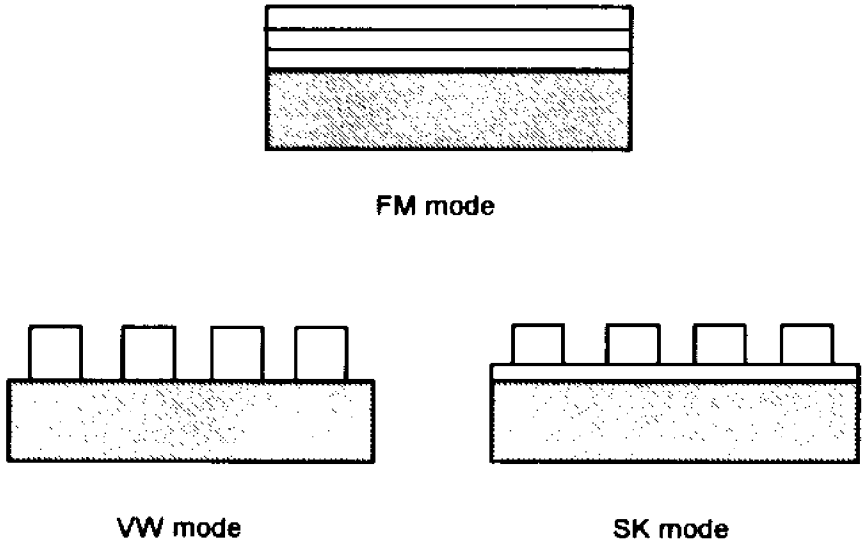

fig. 8(a)

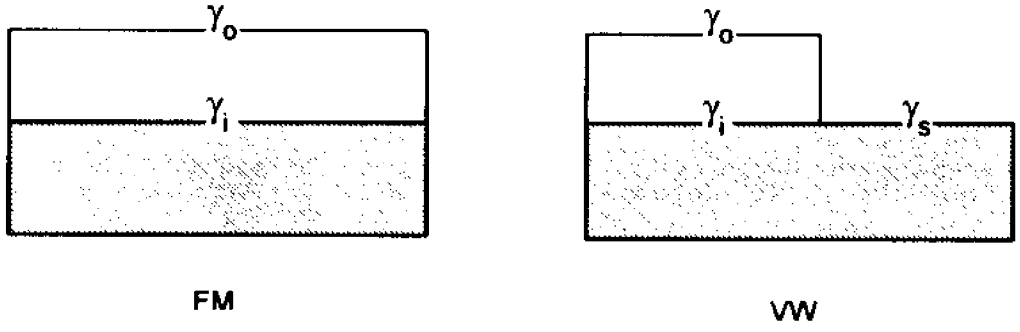

fig. 8(b)

Figure 8. (a) Schematic illustration of thin film growth modes, (b) Depiction of two epitaxial overlayer arrangements for FM mode and VW mode.

$$\Delta E = E_{FM} - E_{VW} = (\gamma_o + \gamma_i)A - \frac{1}{2}(\gamma_o + \gamma_i + \gamma_s)A$$

or $$\Delta E = \frac{1}{2}(\gamma_o + \gamma_i - \gamma_s)A \qquad (3.4.1)$$

Therefore, the condition $\Delta\gamma = \gamma_o + \gamma_i - \gamma_s < 0$ will favor the covering over of the substrate by spreading of the condensate (wetting or FM mode), $\Delta\gamma > 0$ will favor non-wetting (VW mode), and $\Delta\gamma = 0$ will favor the mixture case (SK mode). For SK mode, one assumes that $\Delta\gamma = 0$ is initially satisfied followed by $\Delta\gamma > 0$ at a certain thickness. Approximate values may be known for γ_o and γ_s but rarely for γ_i. When a high surface energy metal is deposited on a low surface energy metal, one way to minimize the system energy is certainly the agglomeration of the adsorbate to reduce the surface area of the high surface energy material, which is why the VW growth mechanism is usually assumed in such situation. The prediction of the type of growth mode from energetic considerations is a complex problem[58-61], which depends critically on the epitaxial relations between the two crystal lattices (misfit) and the degree of strain as described by Bauer and van der Merwe[8] and others[62]; it should be noticed that the above estimate is only qualitatively useful since we have completely neglected any effects that might arise from the anisotropy of the surface tension.

Experimentally the AES peak-to-peak heights of both the adsorbate and the substrate, recorded as a function of the exposure time or coverage is known to give information concerning the mechanism of the deposition processes[63,64]. The FM growth was first analyzed by Gallon[10] who showed that in layer-by-layer growth the signal from n completed absorbed layers, $I_A^{(n)}$, is given by:

$$I_A^{(n)} = I_A^{(\infty)}\left[1-\left(1-\frac{I_A^{(1)}}{I_A^{(\infty)}}\right)^n\right] \qquad (3.4.2)$$

The symbols in above expression with others for later use are defined as follows.

$I_A^{(1)}$: the total Auger signal from the first adsorbed monolayer;

$I_A^{(n)}$: the total Auger signal from n completed adsorbed layers;

$I_A^{(\infty)}$: the total Auger signal from a very thick (bulk) adsorbed layer;

$I_S^{(0)}$: the total Auger signal due to the clean substrate surface;

$I_S^{(n)}$: the total Auger signal due to the substrate covered with n completed layers of adsorbate;

$\alpha_A^{\wedge}$: the transition coefficient of attenuation of the adsorbate Auger peak through a monolayer of adsorbate (due to inelastic scattering of the Auger electrons as they traverse the overlayers, the intensity decreases);

$\alpha_S^{\wedge}$: the transition coefficient of attenuation of the substrate Auger peak due to the presence of a monolayer of adsorbate.

With above definitions, let us consider a film of n completed layers (in case of FM mode). The Auger signal contributed by each individual layer is: $I_A^{(1)}$ (from the top layer), $I_A^{(1)}\cdot\left(\alpha_A^{\wedge}\right)^1$ (from the second top layer), ···, $I_A^{(1)}\cdot\left(\alpha_A^{\wedge}\right)^{n-1}$ (from the bottom layer), etc. Therefore the sum of these terms gives the total Auger signal reaches the analyzer, i.e.,

$$I_A^{(n)} = I_A^{(1)} + I_A^{(1)}\cdot\left(\alpha_A^{\wedge}\right)^1 + I_A^{(1)}\cdot\left(\alpha_A^{\wedge}\right)^2 + \cdots + I_A^{(1)}\cdot\left(\alpha_A^{\wedge}\right)^{n-1},$$

or
$$I_A^{(n)} = I_A^{(1)}\cdot\left[1-\left(\alpha_A^{\wedge}\right)^n\right]\cdot\left(1-\alpha_A^{\wedge}\right)^{-1} \qquad (3.4.3)$$

and
$$I_A^{(\infty)} = I_A^{(1)}\cdot\left(1-\alpha_A^{\wedge}\right)^{-1} \qquad (3.4.4)$$

Combine equations (3.4.3) and (3.4.4), one gets (3.4.2). Similarly for the Auger signal, $I_S^{(n)}$ due to the substrate covered with n completed layers of adsorbate, one has:

$$I_S^{(n)} = \left(\alpha_S^A\right)^n \cdot I_S^{(0)} \qquad (3.4.5)$$

Let $\theta_{0,1}$ denote the fractional coverage as the first layer forms, then the coverage $\theta_{0,1}$ during the formation of the first layer can be expressed as:

$$\theta_{0,1} = \frac{I_A}{I_A^{(1)}} = \frac{I_S - I_S^{(0)}}{I_S^{(1)} - I_S^{(0)}}, \qquad (0 \le \theta_{0,1} \le 1) \qquad (3.4.6)$$

where I_A and I_S are the Auger peak signals corresponding to this coverage.

Similarly $$\theta_{1,2} = 1 + \frac{I_A - I_A^{(1)}}{I_A^{(2)} - I_A^{(1)}} = 1 + \frac{I_S - I_S^{(1)}}{I_S^{(2)} - I_S^{(1)}}, \qquad (1 \le \theta_{1,2} \le 2) \qquad (3.4.7)$$

where $\theta_{1,2}$ is the fractional coverage as the second layer forms. We can generalize above two formulae (3.4.6) and (3.4.7) for the formation of the n-th layers, as following:

$$\theta_{(n-1),(n)} = n - 1 + \frac{I_A - I_A^{(n-1)}}{I_A^{(n)} - I_A^{(n-1)}} = n - 1 + \frac{I_S - I_S^{(n-1)}}{I_S^{(n)} - I_S^{(n-1)}}, \qquad (n-1 \le \theta_{(n-1),(n)} \le n) \qquad (3.4.8)$$

The equation (3.4.8) describes the endpoints of a series of straight lines, each of which represents the growth of a single layer, changes of slope occur because each successive adsorbate layer causes more attenuation. The curves from (3.4.8) are shown in figure 9(a) which is called an AA–t plot. The breaks seen in the figure are only discernible if the sticking coefficient is constant. For changing values of the sticking coefficient with coverage the curves would be smooth and would not display the breaks when a monolayer is completed.

An alternative often used is to plot the ratio of the Auger peak intensities of the substrate and adsorbate as a function of coverage (the so called $I_S / I_A - t$ plot). From equations (3.4.3) to (3.4.5) we have (3.4.9) and (3.4.10) for the first two monolayers and generalized (3.4.11) for the n-th layers.

$$I_S = I_S^{(0)} - \frac{I_S^{(0)}}{I_A^{(1)}}\left(1 - \alpha_S^{\wedge}\right) \cdot I_A \ , \qquad (0 < \theta < 1) \quad (3.4.9)$$

$$I_S = \left[I_S^{(0)} \alpha_S^{\wedge} + I_S^{(0)} \frac{\alpha_S^{\wedge}}{\alpha_A^{\wedge}}\left(1 - \alpha_S^{\wedge}\right) \right] - \left[\frac{I_S^{(0)}}{I_A^{(1)}} \frac{\alpha_S^{\wedge}}{\alpha_A^{\wedge}}\left(1 - \alpha_S^{\wedge}\right) \right] \cdot I_A \ , \qquad (1 < \theta < 2) \quad (3.4.10)$$

$$I_S = I_S^{(0)}\left(\alpha_S^{\wedge}\right)^{n-1} + I_S^{(0)}\left(\frac{\alpha_S^{\wedge}}{\alpha_A^{\wedge}}\right)^{n-1}\left(\frac{1 - \alpha_S^{\wedge}}{1 - \alpha_A^{\wedge}}\right)\left[1 - \left(\alpha_A^{\wedge}\right)^{n-1}\right] - \left[\frac{I_S^{(0)}}{I_A^{(1)}}\left(\frac{\alpha_S^{\wedge}}{\alpha_A^{\wedge}}\right)^{n-1}\left(1 - \alpha_S^{\wedge}\right) \right] \cdot I_A$$

where $(n - 1 < \theta < n)$ (3.4.11)

This kind of $I_S / I_A - t$ plot will in general, also provide a series of curves with breaks at each completed layer but the cusps are harder to detect than the breaks in AA–t plots[10].

AES was used in this thesis to investigate the initial stages of thin film growth by recording the Auger signals from both the adsorbate and the substrate as a function of coverage (AA–t plot). The plot of peak-to-peak height versus the adsorbate coverage (AA–t curve) will show a series of straight lines with breaks for FM mode (figure 9a) and only one break followed by a smooth exponential curve for SK mode (figure 9b) and no break but a smooth curve for VW mode[10].

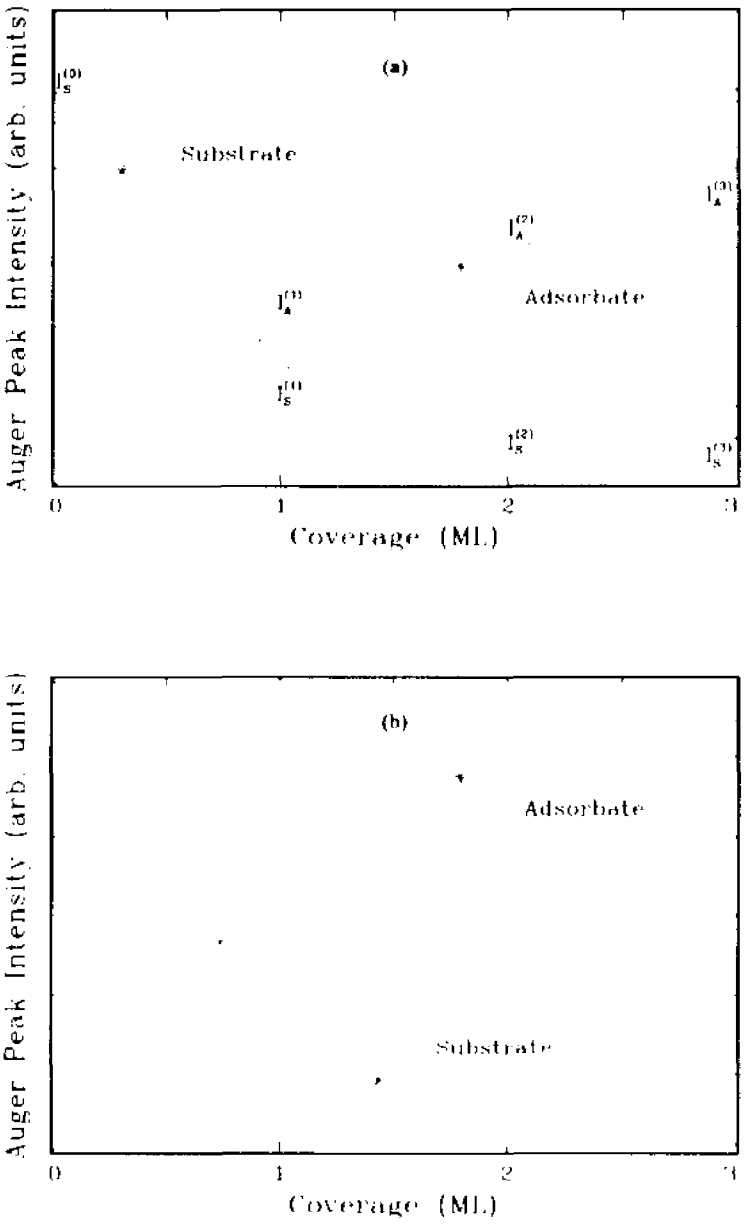

Figure 9. Schematic AA–*t* plots for the adsorbate and substrate, (a) layer-by-layer (FM mode), (b) layer-plus-islanding (SK mode).

Chapter 4. Results and Discussion

For abbreviations we will use the notations SP, BP, IP, and 2SP for Surface Plasmon, Bulk Plasmon, Interface Plasmon, and double Surface Plasmon respectively in this chapter and later discussions. Also introduced is the *first-pair* which stands for the first peak (SP1-loss) and the second peak (BP1-loss) of a plasmon loss spectrum.

First we will examine in detail a simple metal Al and a typical transition metal Ta. The nearly-free-electron metal, such as aluminum, provides us an ideal and easy system for studying plasmon effects because the cooperative excitations are well defined and weakly damped. It also gives us a chance to test the theoretical descriptions of plasmon excitation and effects in the thin films and interfaces; therefore aluminum was chosen to be studied first not only for practical reasons but also in the hope that its simpler electronic structure would be an advantage to understand the processes involved.

The pure aluminum (thick Al evaporated on a substrate metal), Nb (foil), Ta (foil) and Mo (foil)'s EELS plasmon loss spectra had been taken as well as the annealed Al/Nb system. The clean Sn, annealed Sn/Nb, Sn/Mo and Sn/Ta were also studied by using the same techniques. The surface plasmon energies are found to be 10.9, 10.2, 10.1, 11.5, 11.4 eV for Al, Sn, Nb, Ta, and Mo respectively. Those energies are not the same but are close to the theoretical values calculated from the formulae derived in section 3.2 (table 4) where the surface plasmon is predicted to occur at $\Delta E_b / \sqrt{2}$. Our experimental ratio $\Delta E_b / \Delta E_s$ is, respectively, 1.44, 1.36, 1.85, 1.62, 1.93 for Al, Sn, Nb, Ta and Mo; these are close to the predicted ratio, 1.41, for Al and Sn but differ for the transition metals.

For the vacuum–thin-film–metal sandwich's systems, the existence of the IP was predicted by Ferrell[44], and similar prediction and experimental observations in some semiconducting superlattice systems were given by Giulian and Quinn et al[7,65-69]. We studied the Al/Nb, Sn/Nb, Sn/Ta and Sn/Mo systems with the results that the IP-loss shows clearly in Al/Nb film and is observable in other films. The IP-loss energies of Al/Nb, Sn/Nb, Sn/Ta, Sn/Mo are found to be 16.5, 16.2, 15.8, and 15.6 eV. Only the first two IP-loss lines are visible in the spectra and we base our analysis on these first two peaks due to the signal intensities.

4.1 Characteristic EELS of Al and Ta

4.1.1 Al's characteristic EELS

In order to get the plasmon loss spectrum of clean aluminum, we grew an aluminum film of thickness 30 Å on the Nb substrate by thermal evaporation. The thermal deposition rate was typically 1 Å/s and the film deposition was controlled by a quartz monitor.

Figure 10 shows the characteristic plasmon loss spectrum from a clean Al surface using a beam of incident electrons of energy 601 eV and beam current 14 μA. A series of spectra at different incident beam voltages in the range 300–1500 eV were also taken; the comparison and discussion of these spectra are the topic of next section; we will analyse only a single spectrum (figure 10) in this section.

(i) the first-pair:

Our experimental results of clean aluminum show that the first BP- and SP-loss features rise at 10.9 and 15.7 eV respectively and followed by six peaks: 22.0, 26.6, 31.2, 42.1, 46.4, and 62.3 eV in the high energy loss region. From

section 3.2 if the BP-loss has an energy of 15.7 eV then by substituting $\varepsilon = 1$ and $\Delta E_b = 15.7$ eV into the formula $\Delta E_s = \Delta E_b / \sqrt{2}$, the theoretical SP-loss energy at the interface (here it is the Al–vacuum interface) should be 11.1 eV. The facts that the experimental measured BP- and SP-loss energies 15.7 and 10.9 eV are very close to the predicted values 15.8 and 11.2 eV (table 4) provides good support for the theoretical model[44] discussed in chapter 3 for the case of the nearly-free-electron-metal.

(ii) the high order loss peaks:

Table 5 lists the possible predicted plasmon peak positions along with the experimental observed values. In order to check the plasmon loss peak positions other than the *first-pair* which we just discussed, we need to find the possible combinations made up of ΔE_b and ΔE_s. Instead of using the theoretical values 15.8 and 11.2 eV as calculated in section 3.2, we use our experimental observed values 15.7 (BP-loss energy) and 10.9 eV (SP-loss energy) to build up the combinations. The results are listed in column 3 of table 5. First, from table 5 column 3, one might expect to observe the integral multiple plasmon losses at 10.9(SP1), 15.7(BP1), 21.8(2SP), 26.6(SP1BP1), 31.4(BP2), 32.7(SP3), 37.5(SP2BP1), 42.3(SP1BP2) and 47.1(BP3), etc., but only the following peaks show up: 10.9(SP1), 15.7(BP1), 26.6(SP1BP1), 31.2(BP2), 42.1(SP1BP2), 46.4(BP3).

One result that can be seen clearly from table 5, is that the combinations made up of integral multiple SP-losses are not observed, such as 37.5(SP2BP1) and 32.7(SP3); whereas the 2SP loss is seen as a shoulder instead of a real peak. We would expect that triple or quartic SP-losses superposed onto the main BP-loss would have very low relative intensities. The SP-losses are more likely to have high intensities for a single loss that happens near the metal–vacuum interface

while the main BP-losses may undergo some integral multiple losses deeper in the interior. This observation is very helpful in judging the IP-loss lines in later analysis of thin films.

Second, it can be clearly seen from figure 10 and table 5 that all the three peaks containing the SP satellite's loss, labeled as *a*, *d*, *f*, appears exactly at 10.9 eV measured from their previous main BP peak position. These three peaks (with SP satellites) can be decomposed as follows. *a*:10.9 (SP1); *d*:26.6=10.9+15.7 (SP1BP1); *f*:42.1=10.9+31.2 (SP1BP2); On the other hand, the multiple main BP-loss peaks are not observed at exactly the expected positions $n\Delta E_{b1}$. These three peaks *b*, *e*, *g* that are composed of only the BP-losses, do not show up at the exactly intervals of 15.7 eV (the measured BP-loss energy corresponded to the BP1-loss), instead, they show up (with shifts) at: *b*:15.7 (BP1); e:31.2=15.5+15.7 (≅BP2); g:46.4=15.2+31.2 (≅BP3). If we take into account the lower intensities of multiple SP-losses mentioned before imposed onto the main BP-loss, it may give us one reason why the main BP-losses (other than the very first) suffer a shift in position (from 15.7 to 15.5 and 15.2 eV).

Another cause of the shifting could be an oxide film on the aluminum surface. This is not the case, since for an oxide aluminum surface the ε is not equal to 1 (vacuum) any more but some other value larger than 1. If one takes $\varepsilon = 3.65$ (Stern et al[44]) for the oxide surface, then the shifted SP-loss energy will be 7.1 eV which is consistent with Pireaux's XPS experimental result, 7.2 eV[29]. But we clearly do not see the 7.2 eV peak in our spectrum, so the shift is not due to the oxide. In addition, the fact that the observed SP-losses do not show an oxide-shift means that the aluminum surface is clean during the experiment, and on the other hand this provides us with another method to monitor the possible contamination on the surface especially oxygen and carbon.

The SP-loss energy 10.9 eV measured in our laboratory is close to the predicted value 11.1 eV. The SP-loss energy obtained by Pireaux et al[29] by using X-ray excited photoelectron spectroscopy (XPS) is 10.3 eV, and by Seymour et al[70] using EELS is 10.5 eV.

Table 5. Plasmon loss positions of Al (eV)

Experimental Observed	Labels in Figure 10	Semi-theoretical Combinations	Explanation of Column 3*
10.9	a	10.9	SP1
15.7	b	15.7	BP1
22.0†	c	21.8	2SP
26.6	d	26.6	SP1BP1
31.2	e	31.4	BP2
no‡	–	32.7	SP3
no	–	37.5	SP2BP1
42.1	f	42.3	SP1BP2
46.4	g	47.1	BP3

† 22.0: observed as a 'shoulder' in the spectrum.

‡ no: not observed in the spectrum.

* notations for column 3:
SP: Surface Plasmon loss,
BP: Bulk Plasmon loss,
SP1: Single Surface Plasmon loss,
2SP: Double Surface Plasmon losses,
SP1BP1: single Surface Plasmon loss imposed on a main Bulk Plasmon loss.

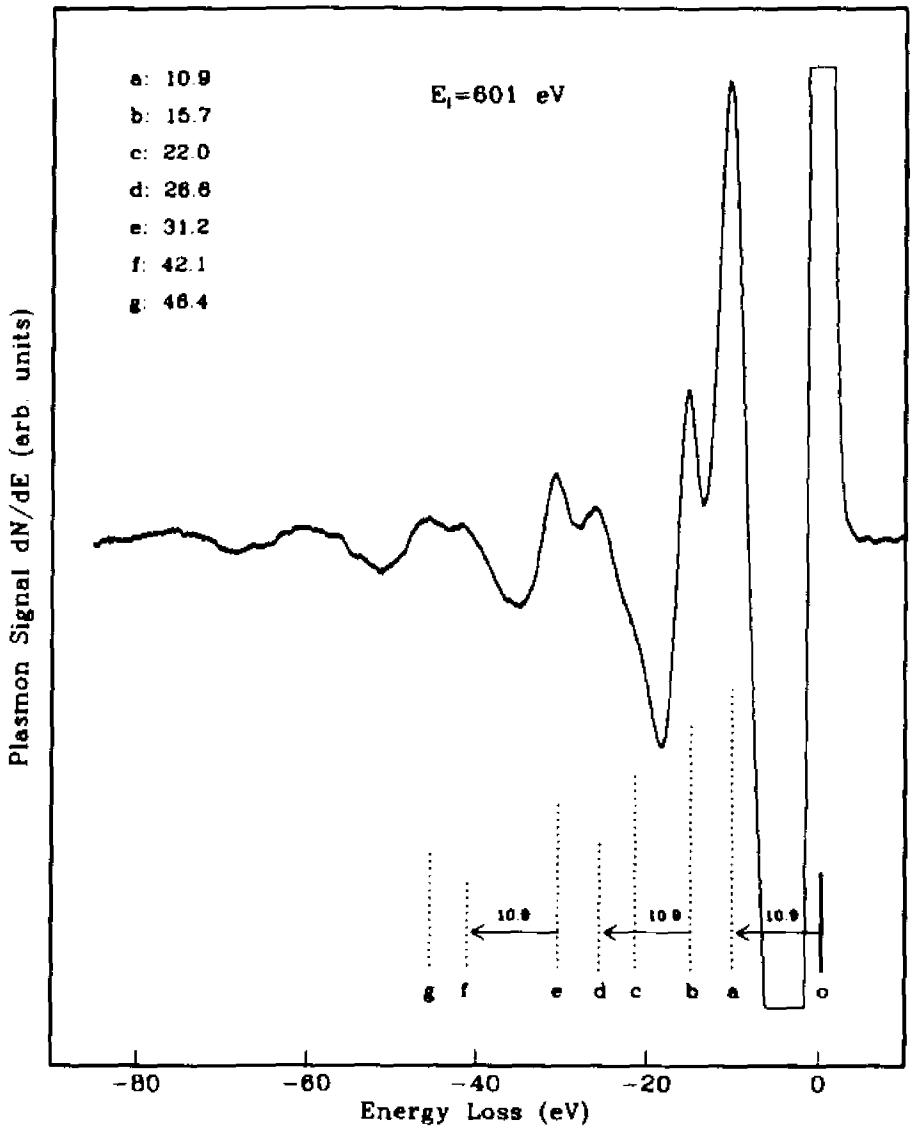

Figure 10. Plasmon loss spectrum of Al using a beam of incident electrons of energy 601 eV, where a, b, c, etc., are measured from the elastic peak position o; and the surface plasmon satellites are indicated by 10.9.

4.1.2 Dependence of the Plasmons Intensities on the Electron's Primary Energy

The SP-losses would be expected to become more prominent, relative to the BP-losses, as the incident electron's penetration decreases, or from figure 7 as the incident electrons beam voltage decreases. Also, the probability of exciting SP's increases with a decrease in the probability of exciting BP's for electrons moving near the surface and the probability of exciting SP's should be proportional to the electron momentum's component parallel to the sample surface[71].

To study the SP- and BP-losses' intensity dependence on the electrons' primary energy, Al was chosen due to its abundant and clear plasmon peaks. At several incident primary energies E_i, Al's plasmon loss spectra, as shown in figure 11, were taken for an experimental geometry with fixed angular orientation; so that the influence on the intensities of the angular dependence of SP- and BP-loss could be eliminated. Figure 12 shows the energy dependence of SP- and BP-loss intensities; where (a) is the plot of the *first-pair* of SP- and BP-losses' intensities versus the electrons primary energies; (b) shows the line-shapes of three typical SP- and BP-losses for the *first-pair* (the whole spectra are given in figure 11); and (c) plots the relative intensities of SP-loss to BP-loss versus the primary energies (as labeled in figure 12-b).

It can be seen clearly from figure 11 that at low primary energies the dominant peak is the SP1-line while for high primary energies it is the BP-lines that dominant the spectrum most. Also observed is that when the primary energy increases the number of multiple BP-loss lines increase due to the increase of electron's penetration depth. Similarly results can be obtained from figure 12 (a) and (b), where the SP-loss intensity is higher than the BP's when the primary

energy is lower than 850 eV, and it becomes lower for energy higher than 850 eV. The change point is at around 850 eV where the SP- and BP-loss almost have the same relative intensities with the same result gotten from (c) as indicated by the dashed line labeled as 0.0. That corresponding line-shape labeled as $E_i = 800$ eV is given in figure 12 (b).

The above observations can be attributed to the fact that the excitation process is an extrinsic process (associated with plasmon excitation by the outgoing electron) instead of an intrinsic process (where the excitation of the plasmon occurs simultaneously with the creation of a hole), and to the fact that electron's penetration depth is much shorter in low energy range therefore less BP-loss will occur. The detected electrons may have crossed the surface twice which will therefore raise the possibilities of the SP-excitation.

One would probably expect the same result for other higher order pairs of SP- and BP-losses, since theoretically each detected BP-loss has a chance of being accompanied by a SP-loss as the electron passes through the vacuum-surface interface; therefore the BP-losses would be expected to show up with SP-satellites and that is indeed observed. But the relative intensity of the *second-pair*, labeled as R.I.(2) in fig (c), shows something different from R.I(1), which designates the relative intensity of the *first-pair*. What we have is that when the primary energy increases the BP-loss' intensity increases, while the SP-loss' relative intensity does not decrease so quickly. In addition in the *second-pair* both lines are expected to be broader than the lines in the *first-pair*, besides the overlapping of these two lines with the 2SP-line will certainly also change their relative intensities. The overlapping of nearby peak lines with a main BP-line accompanied by its SP-satellite, makes the intensities study more complicated especially for the higher

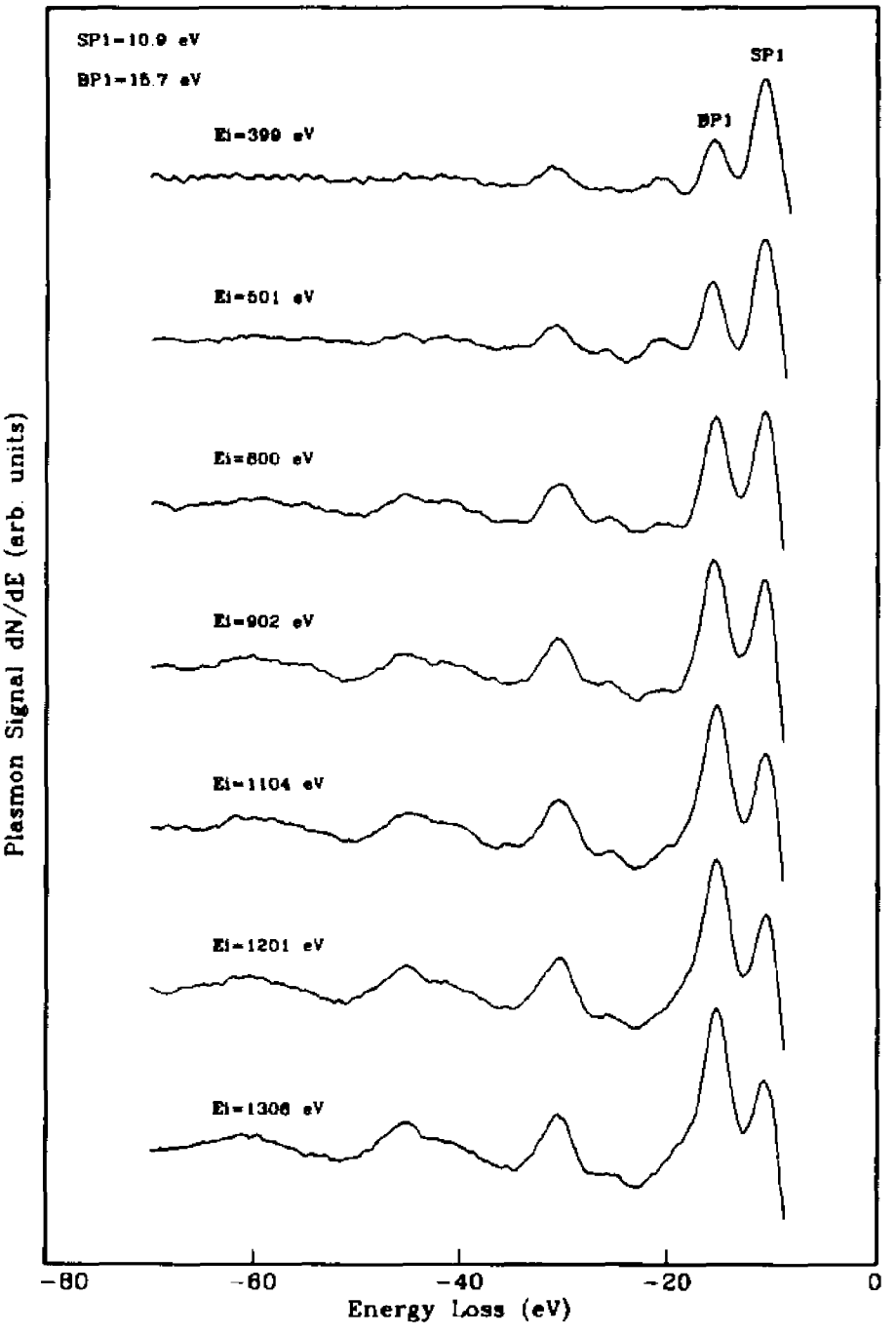

Figure 11. EELS spectra of a clean Al surface for different primary energies. All spectra are lined up to the SP1-loss peak (10.9 eV).

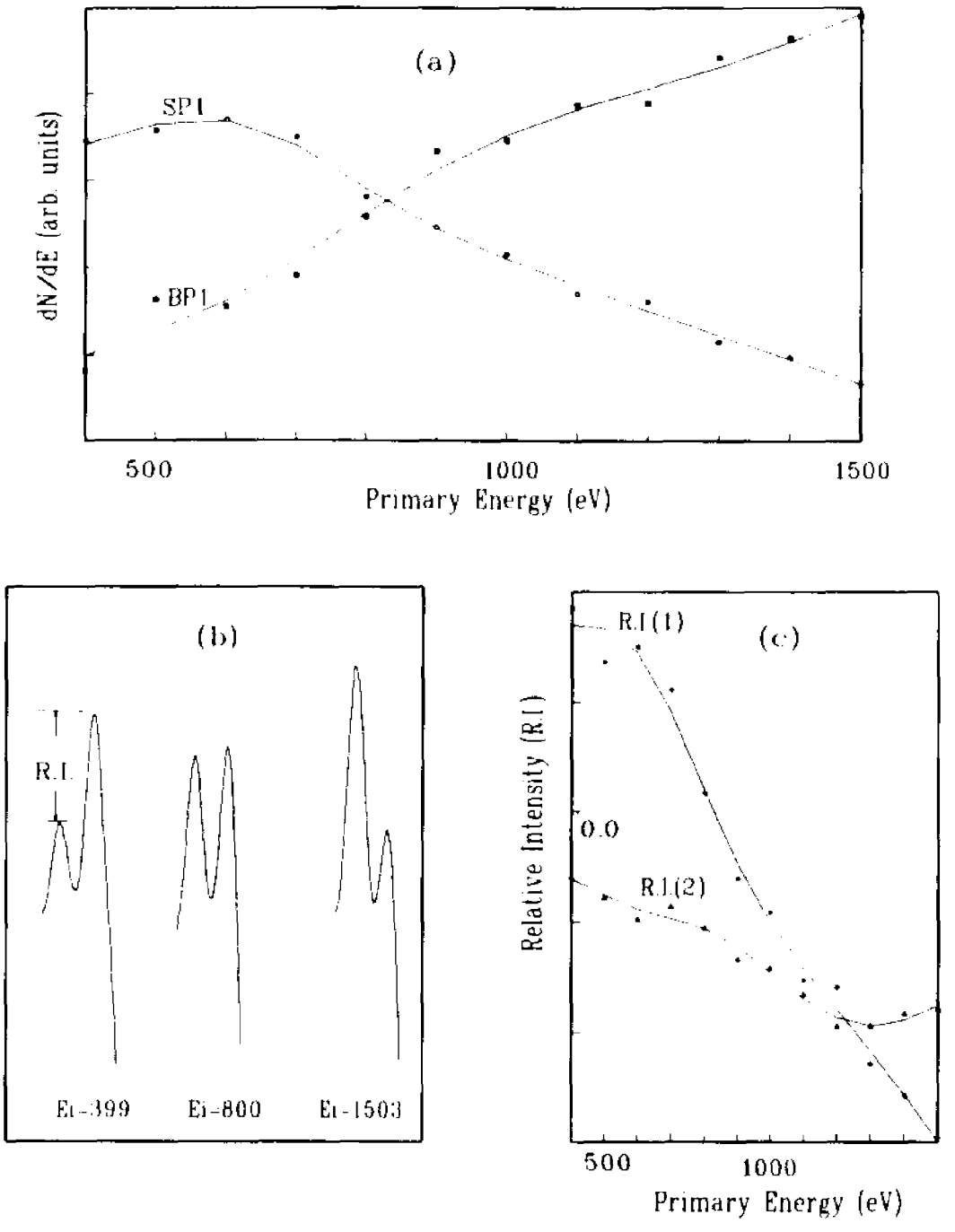

Figure 12. Plasmons intensities vs. the electrons primary energies; (a) SP- and BP-loss intensities of the first-pair, (b) several typical line shapes of the first pair, (c) the relative intensities of SP to BP for the first two pairs in the Al's plasmon loss spectra.

order losses where the overall intensities are themselves too weak to clearly separate the SP- and BP-lines.

4.1.3 Plasmon Loss Line Shape and Double Surface Plasmon Losses

Knowing the line shape of a single plasmon loss (example: from the analysis by Hedin[72] and Penn[73]), one could predict the full spectrum of plasmon losses by convoluting. Unfortunately since a real metal is so complicated or mathematically so many parameters are involved, it is impossible to predict exactly the full spectrum theoretically. Therefore instead of predicting the full spectrum people usually try to fit the spectrum by changing the parameters based on some models. As discussed in the previous section, the SP-satellite lines overlap with the BP-lines, hence change the line shapes; so that the first step of fitting the spectrum is to separate the SP-loss lines from the BP-loss lines.

Penn used a fundamental approach to calculate the BP-loss line shape from theory[73]; the line shape P(E,E') derived from the Lindhard dielectric function $\varepsilon(\omega,k)$ was given as :

$$P(E,E') = \frac{\nu(E)}{\pi\omega E}\int \frac{dk}{k} I_m\left(\frac{1}{\varepsilon(E-E',k)}\right) \qquad (4.1.1)$$

with $I_m[1/\varepsilon(\omega,k)] = \omega_p^2\,\omega\,\tau_k/[(\omega^2-\omega_k^2)^2+(\omega\,\tau_k)^2]$ where ω_p is the plasmon frequency for wave vector $k = 0$, τ_k is a measure for the lifetime which is related to the line width of the plasmons.

A different expression of the plasmon energy distribution function was given by Hedin[72] as follows:

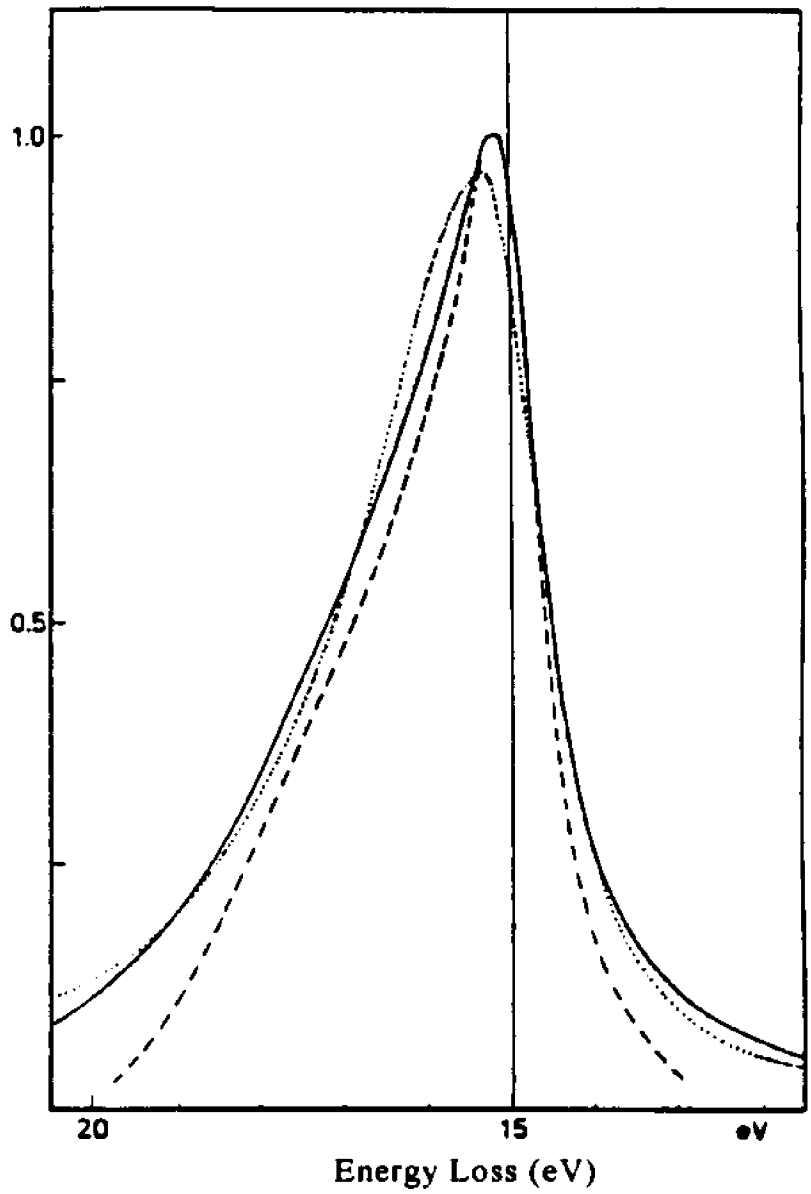

Figure 13. Plasmon energy distribution function calculated with the model of Penn [Exp. (4.1.1)] (dash line), the model of Hedin [Exp. (4.1.2)] (solid line). In both cases $\hbar\omega_p$ = 15.0 eV. Also shown is the asymmetric Lorentzian (dot line) fitted to the curve of Hedin[33].

$$D_n(E) = \frac{e^2}{\pi}\sqrt{\frac{m}{2}}\left(\frac{\omega_p}{\omega}\right)^2 \cdot \frac{\Theta(\omega-\omega_p)}{\omega\sqrt{\omega-\omega_p}} \qquad (4.1.2)$$

then this function was convoluted with a Lorentzian which has a line width dependence on ω_k described as below:

$$\Gamma(\omega_k) = 0.9 + 3.25k^2 \qquad (4.1.3)$$

$$\hbar\omega_k = \hbar\omega_p + 3.01k^2 \qquad (4.1.4)$$

where $\Gamma(\omega_k)$ is expressed in eV and k in $Å^{-1}$. Attekum et al[33] did a numerical calculation of Hedin's function with $\hbar\omega_p = 15.0$ eV (a typical BP-loss energy) and compared the result with Penn's mode and asymmetric Lorentzian mode. Their comparison of different modes for the plasmon loss line shapes is shown in figure 13[33] which indicates that the Lorentzian line shape is a nice approximation for the second and higher plasmon loss peak although it has little difficulty for the first peak due to its symmetry.

To analyse the plasmon line shapes we use a simpler analytical expression – the symmetric Lorentzian for computational reasons. Therefore the *n*-th SP- or BP-loss line P_n is obtained as follows:

$$P_n(E) = \frac{I_n}{1+[(E-E_n)/\Gamma_n(E)]^2} \qquad (4.1.5)$$

where E_n is the bulk- or surface-plasmon energy, I_n is the peak intensity, and Γ_n is half of the FWHH (full width at half height). Due to the large uncertainty in the background especially under the peaks near the primary energy, the background correction was taken into account for the theoretical line shape analysis and was approximated by:

$$B_{base}(E) = c_1\left(1 - c_2 e^{\frac{(E-E_0)}{c_3}}\right) \qquad (4.1.6)$$

where E_0 is the primary energy, c_1, c_2, and c_3 are parameters. Combine expression (4.1.5) with (4.1.6) we have a fit-curve described by N(E) as follows:

$$N(E) = B_{base}(E) + \sum P_n(E) \qquad (4.1.7)$$

Since our original data is in the derivative form, dN(E)/dE, take the derivative of above expression; that yields:

$$dN(E)/dE = \left(\frac{c_1 c_2}{c_3}\cdot e^{\frac{(E-E_0)}{c_3}}\right) - \sum \frac{2I_n\cdot(E-E_n)/\Gamma_n^2}{\left[1+(E-E_n/\Gamma_n)^2\right]^2}$$

Without losing the generality, the above expression can be rewritten as:

$$dN(E)/dE = p_1\cdot\left(1 + p_2\cdot e^{\frac{(E-E_0)}{p_3}}\right) - \sum_{n=1}^{m} \frac{2I_n\cdot(E-E_n)/\Gamma_n^2}{\left[1+(E-E_n/\Gamma_n)^2\right]^2} \qquad (4.1.8)$$

where p_1, p_2, and p_3 are parameters to be fitted for the base line. Expression (4.1.8) is the one we used for the curve fit; for case of aluminum $m = 7$ (7 lines) was used. The best values of the parameters for fitting the spectrum were determined with a least squares fitting procedures[74] with the requirements that the first two pairs of plasmon losses, including the 2SP-shoulder, should be fitted best. The Lorentzian line shape is symmetric yet the real line shape may not be, therefore the least squares fitting procedure was restricted a little bit. Even so several nice fitted curves of EELS were obtained for clean Al (thick film), Ta foil, and Al/Nb film.

Figure 14 gives the best fit of figure 10 which is the Al's plasmon loss spectrum with an incident energy of E_0 = 601 eV. The parameters used for the fit are listed in table 6. In figure 14, (a) is the overlay of the data and its fit; where it is hard to see which is which, so that the decomposition of the plasmon loss lines is given in (b); part (c), the insertion in (b), shows the 2SP-loss line shape. After background corrections were made as shown in figure 14(b), SP-loss lines (SP*n*), labeled as 'SP LINES' were clearly discerned apart from BP-loss lines (BP*n*), labeled as 'BP LINES' graphically. The extra 2SP-line shown in figure 14(c) has to be introduced to fit the *first-* and *second-pair* as well as the shoulder labeled as '*c*' in figure 10. Without introducing the 2SP-line one would get a nice fit neither for the *first-pair* nor for the *second-pair*. Since the 2SP-line is sited between the first two pairs, it will effect both pairs' line shapes even though it has a weak intensity relative to the SP1-line. Another consideration was that the SP-satellite peak lines, such as SP1BP1 and SP1BP2, should also have lower intensities. The relative intensity ratio for SP- and BP-lines is, respectively, $R_s^{(1)} = I_{2SP} / I_{SP1} = 0.23$, $R_s^{(2)} = I_{SP1BP1} / I_{BP1} = 0.24$, $R_b^{(1)} = I_{BP2} / I_{BP1} = 0.44$, and $R_b^{(2)} = I_{BP1} / I_{BP2} = 0.37$. The ratios in table 6 are the average values.

Several points are noteworthy. (i) the theoretical curve was fitted to the original spectrum which was neither smoothed nor treated by any other pre-treatment; (ii) the 2SP-line had to be introduced in order to get a nice fit; (iii) the final fitted curve shown as solid line in figure 14(b) was the one after taking into account of the elastic peak which changes the right tail of the SP1-line[75]; (iv) the base line presumably due to the inelastic scattering of the electrons other than the plasmon excitations has to be included. The reliability of the above treatments and results however are supported by the good fit obtained.

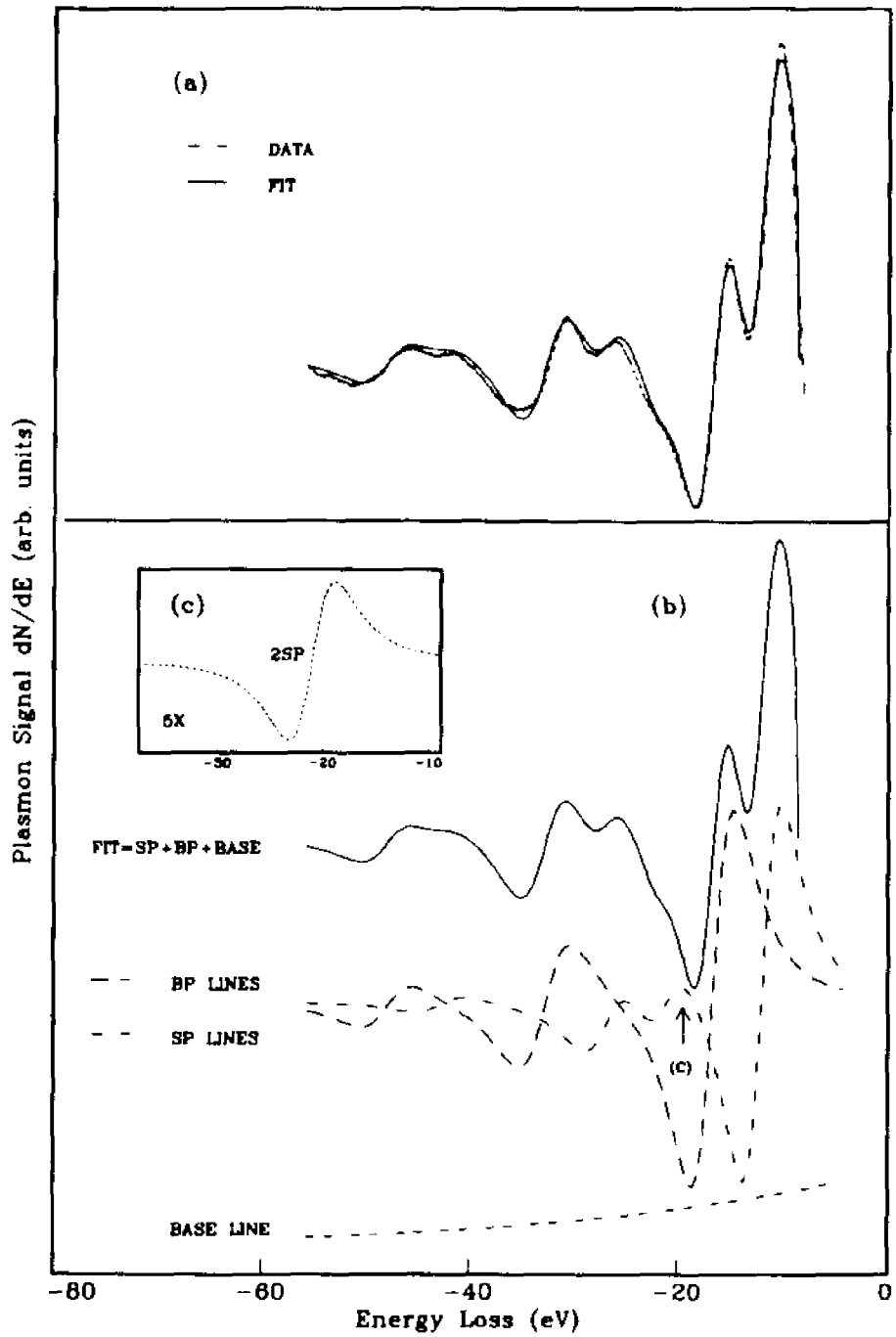

Figure 14. Al plasmon losses lines. In (b), BP LINES are the bulk plasmon losses: BP1+BP2+BP3, and SP LINES are the surface plasmon losses: SP1+2SP+SP1BP1+SP1BP2. In (c), 2SP is the double surface plasmon losses line.

Table 6. Best parameter value for the plasmon loss of Al (E_i = 601eV)

Line Name†	E_n(Semi-Th.)	E_n(Exp.)	E_n(Fitted)	Γ_n(eV)	I_n
SP1	10.9	10.9	10.9	3.1	1.00
BP1	15.7	15.7	15.6	3.5	1.05
2SP	21.8	22.0	20.0	3.8	0.23
SP1BP1	26.6	26.6	25.7	4.0	0.25
BP2	31.4	31.2	31.7	4.3	0.46
SP1BP2	42.3	42.1	41.7	4.4	0.06
BP3	47.1	46.4	46.9	4.5	0.17
Base Line	p_1 / I_1 = 6.10%	p_2 = 1.40	p_3 = 30.0		
Intensity Ratio	R_s = 0.24	R_b = 0.41	R_s / R_b = 0.59		

4.1.4 Characteristic EELS of Ta

The Ta's characteristic plasmon loss spectrum was obtained in the same way as described in above section with the exception that the Ta foil[16] was used. The spectrum, obtained by using a beam of primary energy of 503 eV and beam current of 15 μA, is shown in figure 15. The SP- and BP-loss energies measured from the spectrum are found to be 11.5 eV and 18.6 eV respectively and they are lower than the theoretical values of 13.9 eV and 19.6 eV, that can also be seen

†Meaning of the symbols is given in the text.

from the ratio $\Delta E_b/\Delta E_s$=1.6 instead of the predicted 1.4. Similar results (12.5, 20.5 eV, and $\Delta E_b/\Delta E_s$=1.6) were also gotten by Schubert[76] et al. The possible combinations made up of 13.9 eV and 19.6 eV (the predicted values) are listed in table 7.

The plasmon loss spectrum of Ta (figure 15) has many features in common with those we get for Al (figure 10). First the order of appearance of the plasmon-losses' combination is exactly the same for both metals with the SP1-line comes first followed by BP1-, $2SP^{\dagger}$- (or SP1BP1-), BP2-, and SP1BP2-lines. These peaks are labeled as *a*, *b*, $c^{\dagger}$, *d*, *e* respectively in the figures and their corresponding tables. For the SP-loss (or SP1BP1-loss) at $2SP^{\dagger}$ ($c^{\dagger}$), it only shows a shoulder instead of a real peak in both spectra but the important information we get is that the $2SP^{\dagger}$ ($c^{\dagger}$) 'shoulder/peak' is much clearer in Ta's spectrum than in Al's. That agrees with the fact there does exist the possibility of high order SP-losses even though they have much lower intensities than the single SP-loss.

The particular rich structures of the Ta' EELS are worthy of more examinations. Line shape analysis of figure 15 was studied by using a Lorentzian line shape fit; the first two pairs of 5 lines were fitted ($m = 5$ in expression 4.1.8). The best parameters of fitting are listed in table 8 and the fit curve along with the components of the BP-, SP-, and Base-lines are shown in figure 16. After careful examination of the SP-lines apart from the BP-lines it becomes clear that the shoulder labeled as '*c*' in figure 15 is indeed due to the double-SP-loss; the same result gotten for the case of Al.

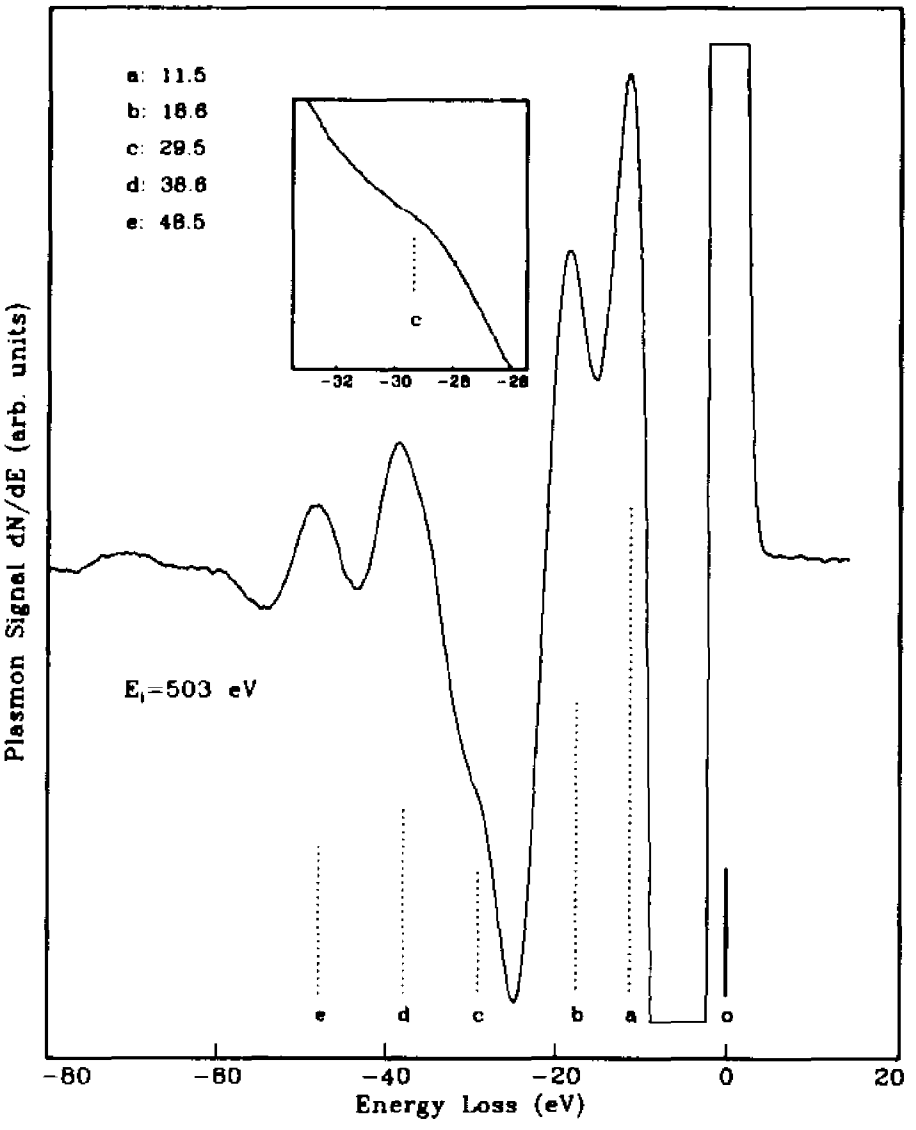

Figure 15. Plasmon loss spectrum of Ta using a beam of incident electrons of energy 503 eV, where a, b, c, etc., are measured from the elastic peak position o.

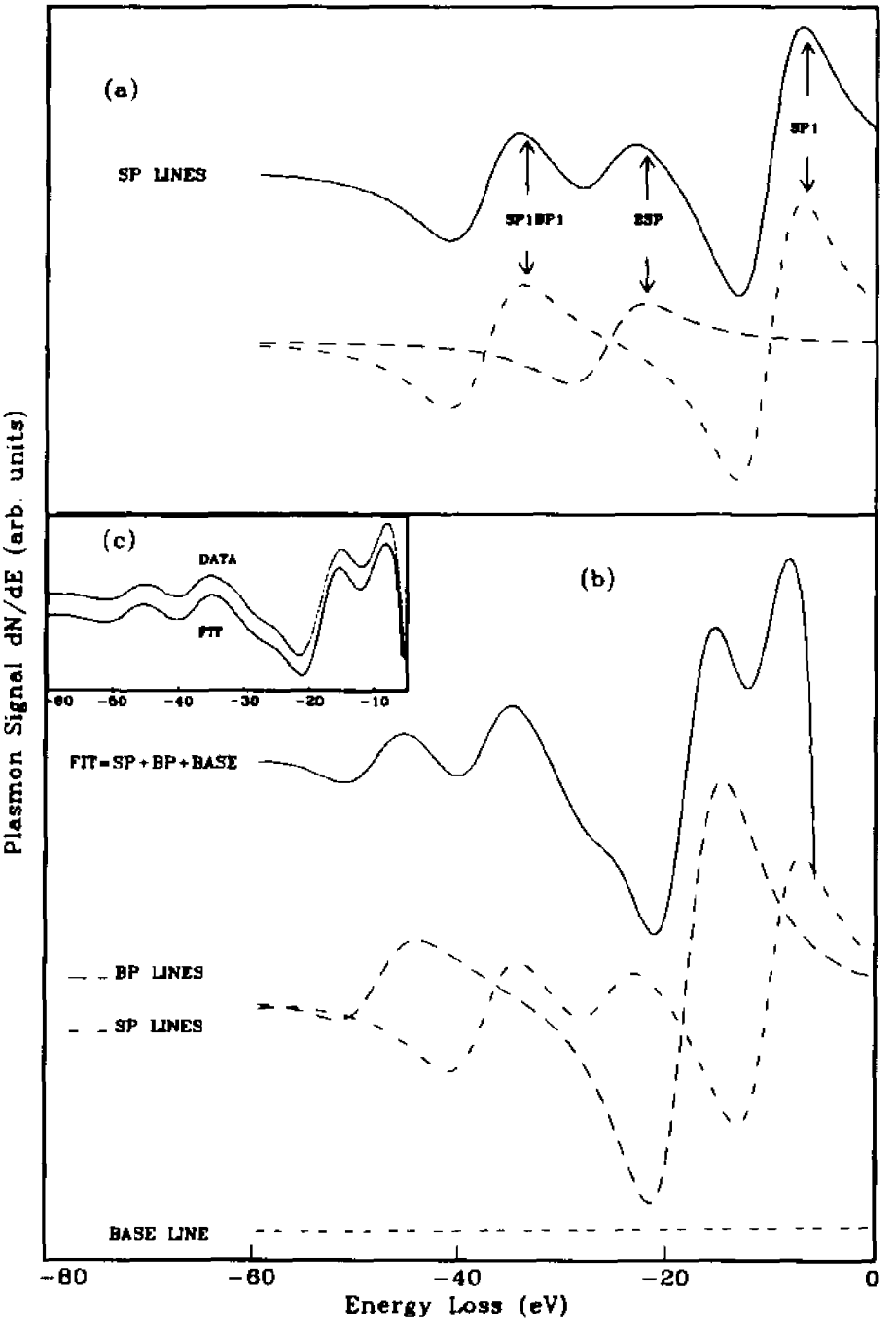

Figure 16. Ta plasmon losses lines. Where BP LINES are the bulk plasmon losses: BP1+BP2, and SP LINES are the surface plasmon losses: SP1+2SP+SP1BP1. In (a), 2SP is the double surface plasmon losses line; (c) is the data and fit.

Table 7. Plasmon loss positions of Ta (eV) (E_i = 503eV)

Experimental Observed	Labels in Figure 15	Theoretical Predicted	Explanation of Column 3*
11.5	a	13.9	SP1
18.6	b	19.6	BP1
29.5†	c	27.8	2SP
29.5†	c	33.5	SP1BP1
38.6	d	39.2	BP2
no‡	–	41.7	SP3
no	–	47.4	SP2BP1
48.5	e	53.1	SP1BP2

Table 8. Best parameter value for the plasmon loss of Ta (eV)

Line Name	E_n(Th.)	E_n(Exp.)	E_n(Fitted)	Γ_n(eV)	I_n
SP1	13.9	11.5	11.1	5.4	1.00
BP1	19.6	18.6	19.1	6.0	1.70
2SP	27.8	29.5†	26.7	6.2	0.33
SP1BP1	33.5	29.5†	26.7	6.2	0.33
BP2	39.2	38.6	38.4	6.3	0.53
SP1BP2	53.1	48.5	48.6	6.9	0.66
Base Line	$p_1 / I_1 = 1.5\%$		$p_2 = 0.89$		$p_3 = 50$
Intensity Ratio	$R_a = I_{2SP} / I_{SP1} = 0.33$		$R_b = I_{BP2} / I_{BP1} = 0.31$		$R_a / R_b = 1.1$

*, †, and ‡ : same as in table 5.

Due to the interband transitions[42,46], the higher order plasmon loss lines are expected to broaden and that will consequently shift the line position because of the overlapping of nearby SP-satellite's line with BP-lines. That effect, especially for the line 2SP is indeed observed in the Ta's spectra (figures 15 and 16). The other observations, that the higher order plasmon loss peaks show position shift, were also reported by Simmons and Scheibner[45] in other transition metals such as Titanium, Vanadium, and Chromium. It is clear that in the transition metals the special effects contributed by the *d*-band electrons must be taken into account in order to get a complete theoretical description. Even though, the semi-classical theory still provides us a very reasonable guide for the plasmon loss line studies.

It can be concluded that the characteristic energy loss spectrum for Al (Ta) in the range 0–32 eV (0–49 eV) is composed of at least five plasmon loss lines including the double-SP-loss line. Nice agreement between theory and experiment is obtained for Al and moderate agreement for Ta. For the case of Al a free electron model is a good approximation. While for the case of Ta, which is a transition metal, it is difficulty to separate the terms in expression (3.2.2) as well as to distinguish between density of the free electron and the more tightly bound core electrons and to calculate interband transitions. This may account for the observed result that the relative peak height of '*d*' (BP2) is much higher than '*e*' (SP1BP2) for Al but opposite for the Ta.

4.2 EELS of Al Films on Nb

In our experiment we did observe the IP-loss peaks (IP1-, SP1IP1- and IP2-loss peaks) for the annealed Al/Nb films; the measured IP-loss energy is 16.5 eV in average that is slightly less than the semi-theoretical value of 17.3 eV, using our experimental measured BP-loss energy 15.7, 18.7 eV for Al and Nb respectively, and the predicted value 17.8 (table 4). We choose Al/Nb to investigate first because of some interesting characteristics of this system. Both elements exhibit nearly the same atomic radius, but crystallize in different structures, aluminum crystallizes in the fcc structure whereas niobium is a bcc metal.

4.2.1 Plasmon Loss Spectrum of Pure Niobium

Before analyzing the Al/Nb system, first we take a look at the Nb's characteristic plasmon loss spectrum, since Nb is used later as the substrate. Niobium foil was used to get its plasmon loss spectrum which is shown in figure 17. The very first SP1-loss peak shows up at 10.1 eV followed by the BP1-loss peak 18.7 eV. For comparison, Schubert and Wolfl[76] obtained experimental value of 9.6 and 20.8 eV. The possible combinations made up of 19.6 eV and 13.9 eV (the predicted values, table 4) are listed in table 9. The orders of the appearance of the plasmon loss peaks are exactly the same as those of Al and Ta discussed in previous section. We will use figure 17 as our reference spectrum of clean Nb when we study the annealed Al/Nb system in the following section.

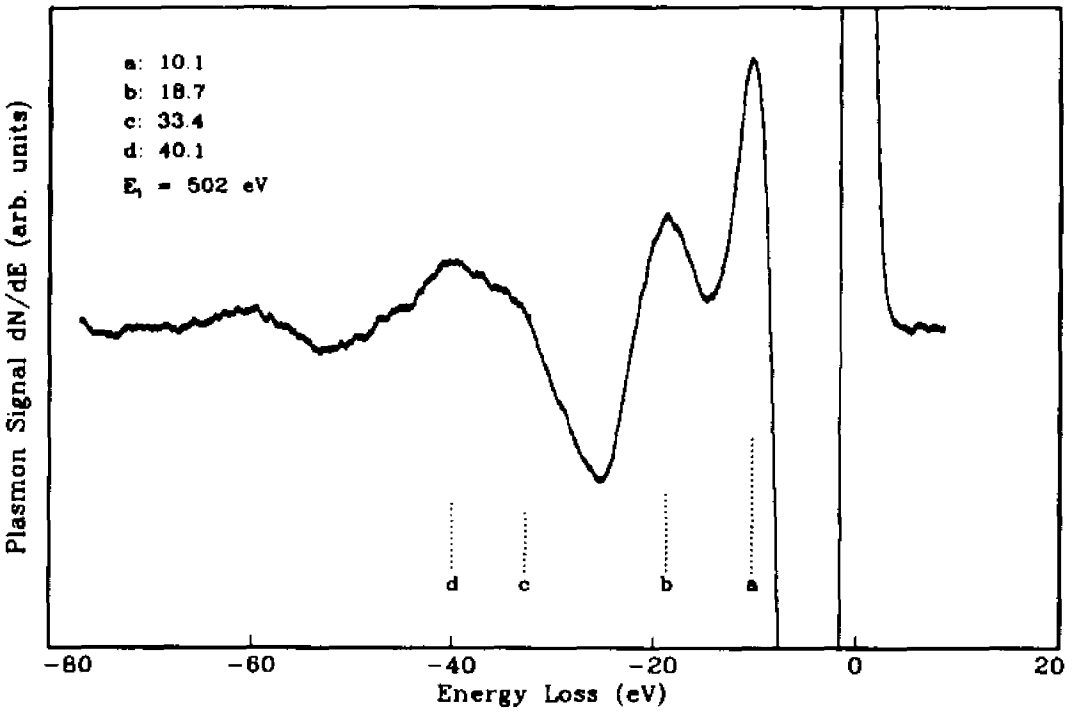

Figure 17. Plasmon loss spectrum of Nb.

Table 9. Plasmon loss positions of Nb (eV)

Experimental Observed	Labels in Figure 17	Theoretical Predicated	Explanation of Column 3*
10.1	a	13.9	SP1
18.7	b	19.6	BP1
no‡	–	27.8	2SP
33.4	c	33.5	SP1BP1
40.1	d	39.2	BP2

*and ‡: same as in table 5

4.2.2 Interface Plasmons of Al/Nb Films

Al layers of various thicknesses were grown on Nb at room temperature and annealed at stepwise increasing temperatures up to 1500 K for about 100 seconds. The orientations of the films were fixed during the anneals, so the influence of geometry on the EELS measurements could be ignored. Figure 18 and 19 show the spectra of the annealed Al/Nb film where in the figure 19 only the spectra within the energy range of the SP1-, IP1-, and BP1-losses are shown, and in figure 20 the whole spectra of fresh Al, three of Al/Nb, and clean Nb are shown. As shown in the above figures, when the anneal temperature increase and the overlayer changes; the plasmon loss spectrum of the system (initially labeled as 'Fresh Al' in figure 19 and 20) shows line shape changes and in addition the plasmon loss energies shift; when the temperature reached 1400 K, the spectrum becomes characteristic of the Nb surface (labeled as 'Clean Nb' in the figures). The fact, that the multiple plasmon losses overlap with the near by peaks and therefore change the peak shape, as discussed before, makes the analysis and peak position measurements more difficult. We will concentrate on the second loss peak in the following discussion. The peaks indicated by the arrows in figure 19 clearly show the plasmon energy shift starting from the fresh Al's BP1-loss of 15.7 eV to some new values among 16.0 eV ~ 17.5 eV and finally to the clean Nb's BP1-loss of 18.7 eV. In figure 20 both peaks of 16.4 eV and 16.7 eV indicated by one-direction arrows are expected to be the IP-losses. Those values are about 5% less than 17.3 eV which is the semi-theoretical IP-loss energy of Al/Nb calculated from expression (3.2.10) by using $\Delta E_{b1(Al)} = 15.7eV$ and $\Delta E_{b1(Nb)} = 18.7eV$. The second group of the loss peaks also show clearly peak shape changes as indicated by the two-direction arrow in figure 20. Figure 21,

which shows the Lorentzian fit of an Al/Nb spectrum, suggests that these twin peaks are probably the IP2- and SP1IP1-loss lines. The expected IP-loss peak positions are also indicated by the dash lines which are labeled as 16.4, 27.3, and 32.8 in figure 18. The other strong evidence of supporting the interpretation of the observed intermediate peaks being the IP-losses is the consequence of the vanishing of the higher order plasmon loss lines (labeled as 'Al-high' in figure 20). Those higher order plasmon loss lines can be clearly observed in both the Al and the Nb's characteristic EELS spectra. During the anneal these lines also show drastic line shape changes, especially their peak heights. From inspections of the middle three curves labeled as 'Al/Nb' in figure 20, it is obvious that those higher order plasmon loss lines are almost unobservable in the high energy loss region. It is also at this time that the first two pairs of the IP-losses become visible in the spectra (labeled as 16.4 and 16.7 for the *first-pair* and indicated by the two-direction arrow for the *second-pair*). This kind of curve change, that the IP-loss lines start to show up (only) when the higher order plasmon loss lines vanish from the spectrum, is also observed in other films such as Sn/Nb, Sn/Mo and Sn/Ta. In later discussions of those films we will use this feature as an evidence for judging if the intermediate loss peak is due to an IP-loss of the film or to a BP-loss of the substrate.

To get a deeper understanding of the intermediate loss spectra (some of the lines are interpreted due to the IP-losses of the Al/Nb film), the spectrum was decomposed into the individual loss lines using the Lorentzian line shape technique. The corresponding decomposed spectrum is given in figure 21, and the best parameters for fitting are listed in table 10. In table 10, column 2 gives the combinations made up of 11.2 and 17.8 which are the predicted values, column 3 gives the combinations made up of 10.9 and 16.4 those are the semi-theoretical values, and columns 4, 5, 6 and the row Base-Line give the values determined from the curve fit. We see that the fitted values for the E_n for the second pair of peaks (column 4) are within a few percent of the calculated values in columns 2 and 3; so we ascribe this pair of peaks to the double losses SP1IP1 and IP2.

Table 10. Best parameter value of the Lorentzian line fit for the EELS of the Al/Nb film (E_i = 501 eV)

Line Name	E_n(Th.)	E_n(Semi-Th.)	E_n(Fitted)	Γ_n(eV)	I_n
SP1	11.2	10.9	10.9	3.3	1.00
IP1	17.8	16.4	16.4	4.8	1.35
SP1IP1	29.0	27.3	26.2	6.2	0.33
IP2	35.6	32.8	33.4	6.2	0.38
Base Line		p_1/I_1=0.64%	p_2=16.6	p_3=123	

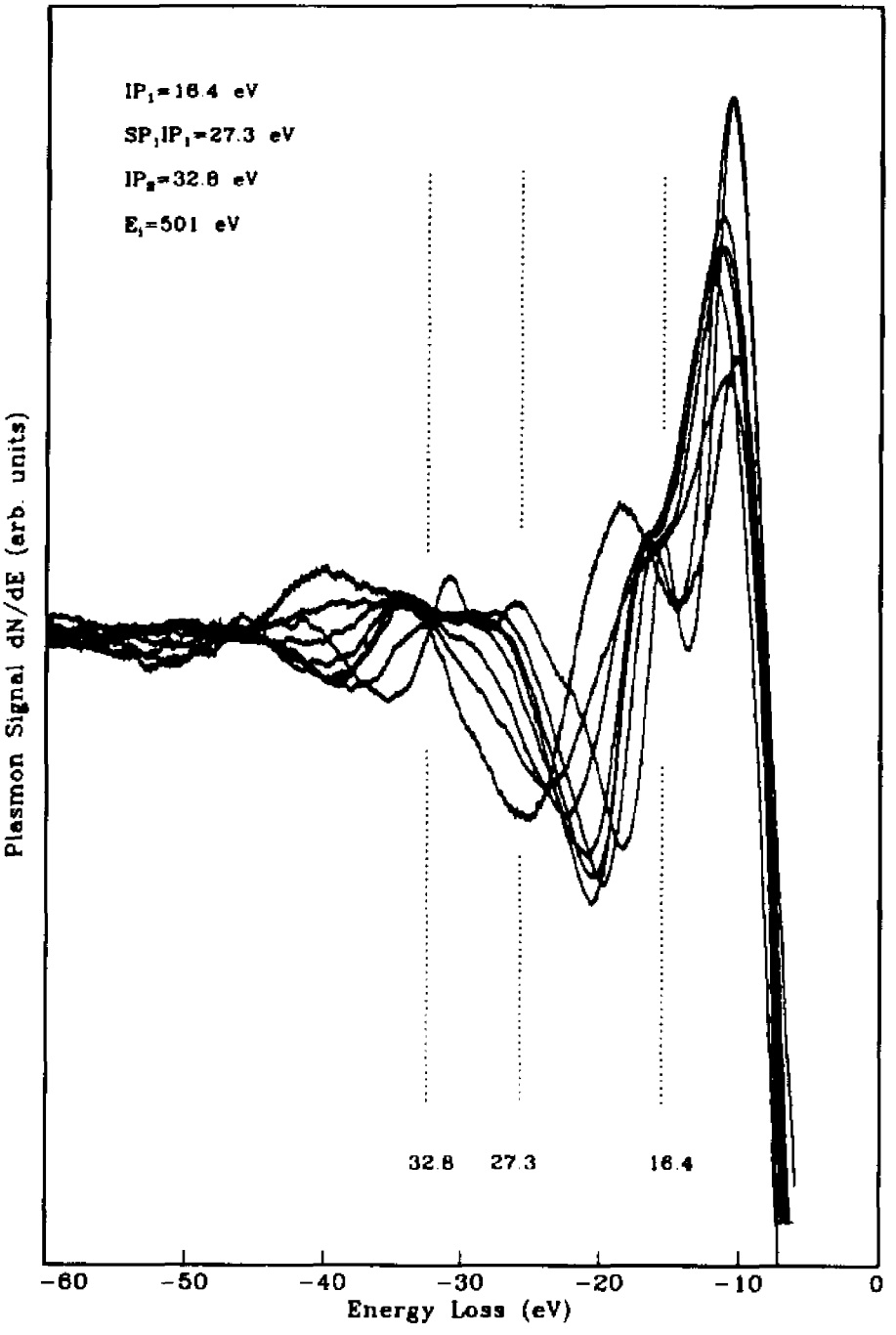

Figure 18. The full spectra of Al/Nb film, zoom-view of the first-pair plasmon losses is given in figure 19.

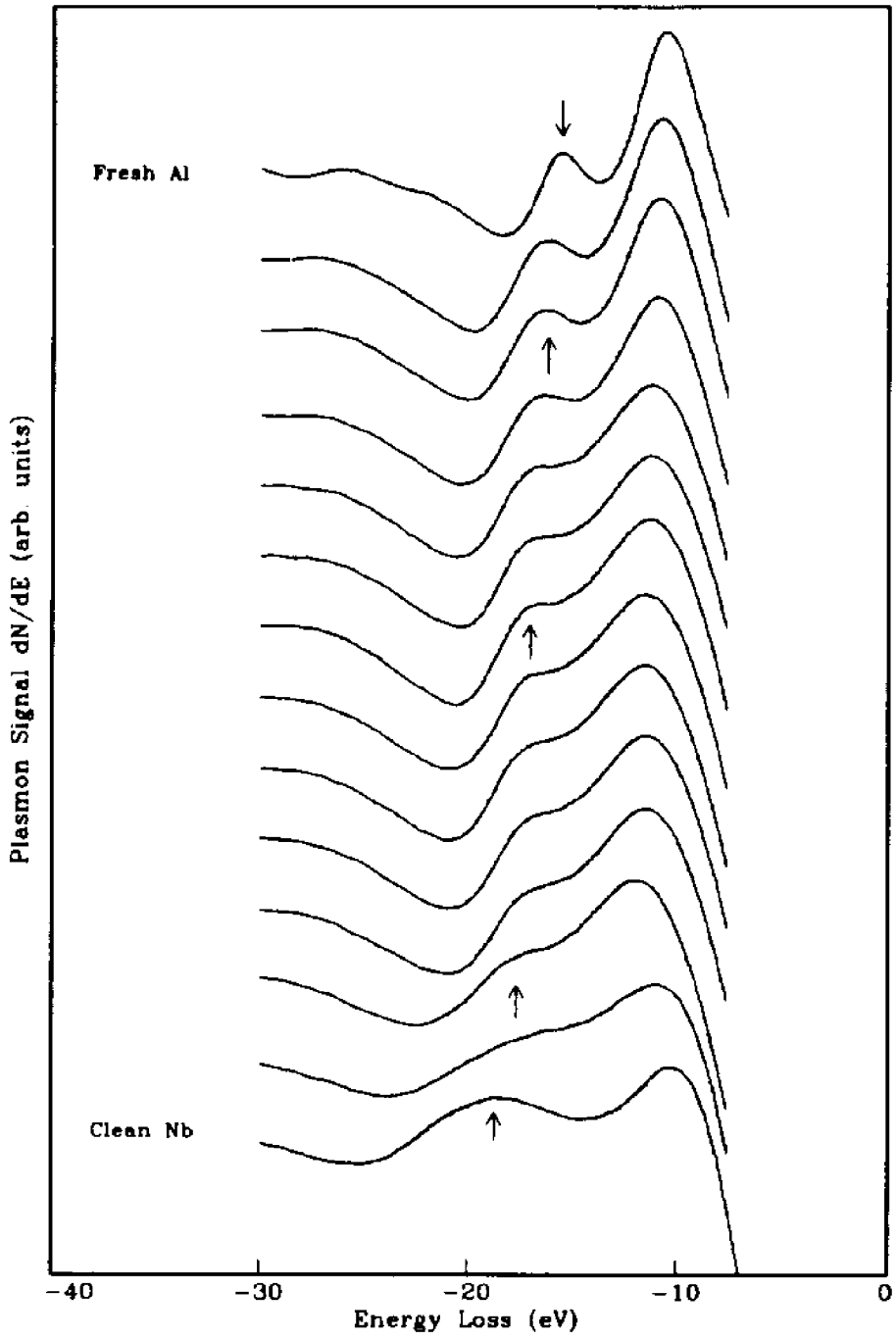

Figure 19. Interface plasmon spectra of Al/Nb film using a beam of incident electrons of energy 501 eV. The film was annealed at stepwise increasing temperatures up to 1500 K.

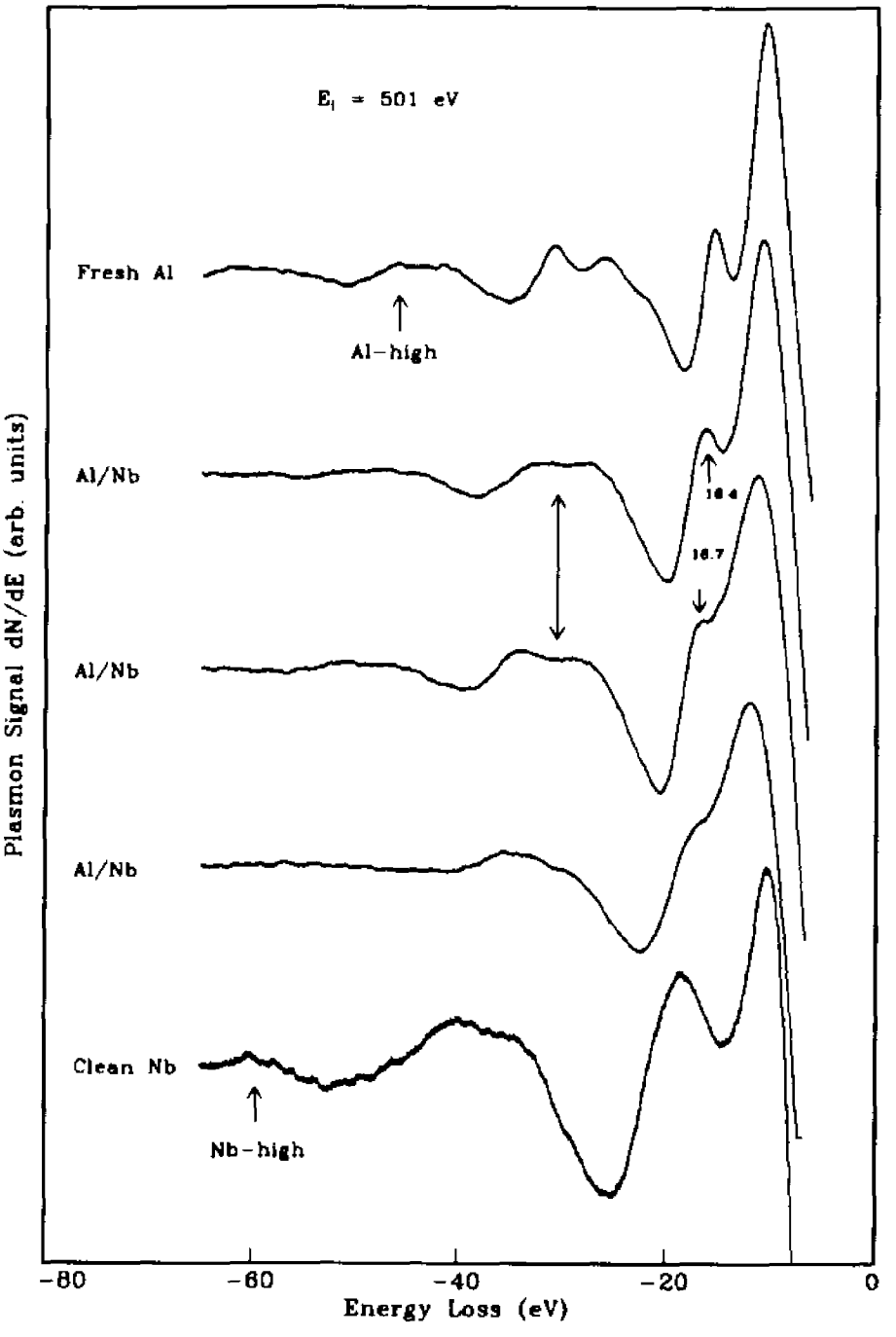

Figure 20. Interface plasmon of Al/Nb, where the interface plasmon loss energies are 16.4eV and 16.7 eV as indicated by the one direction arrows.

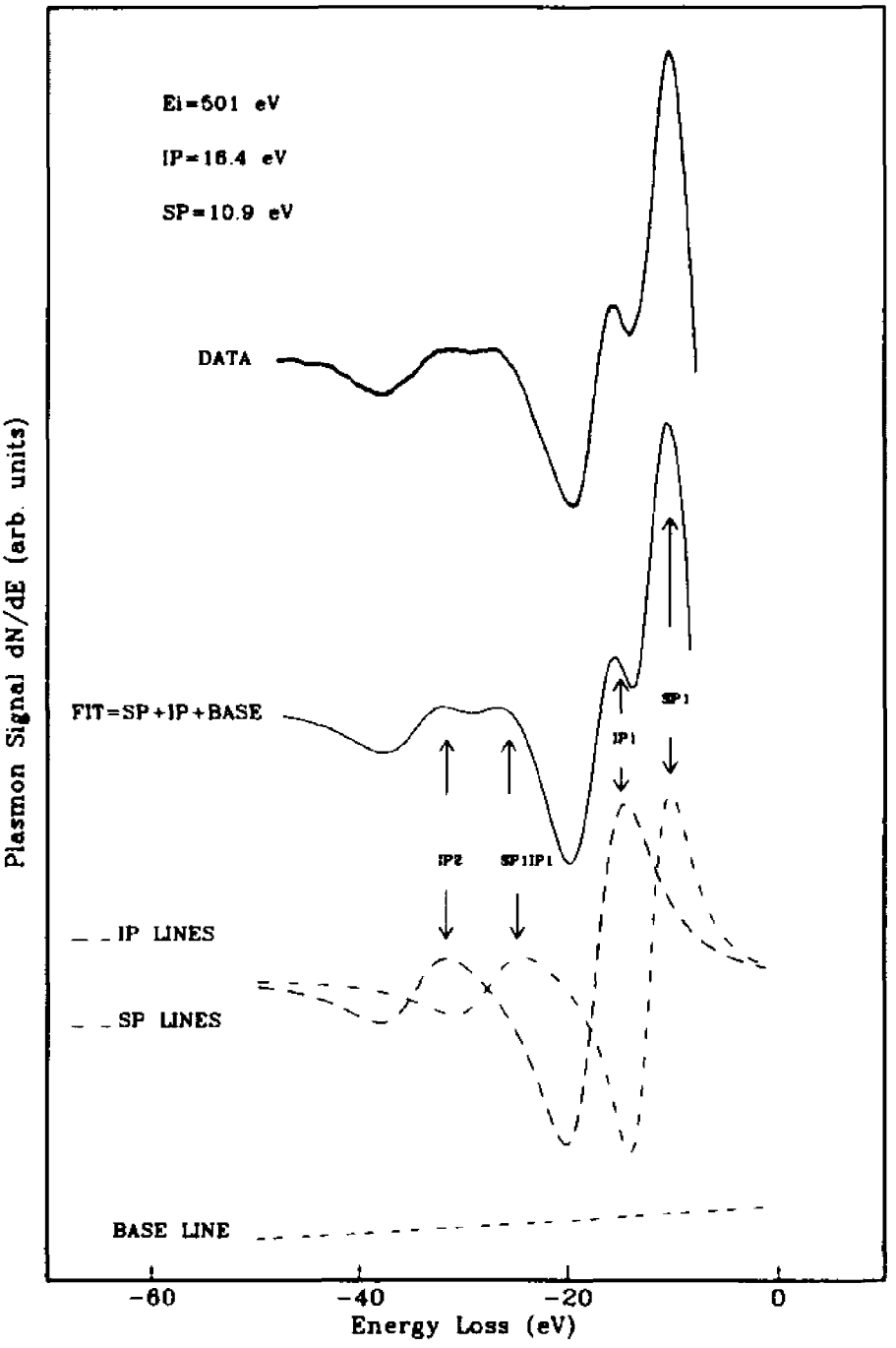

Figure 21. Interface plasmon loss lines of Al/Nb film. Where IP LINES are the IP-losses: IP1+IP2, and SP LINES are the SP-losses: SP1+SP1IP1. The right tail of the FIT line is treated by taking into account the elastic peak.

4.3 Sn Films on Nb, Ta, and Mo

Sn films on Nb, Mo, and Ta have been studied. This section is organized according to the substrate used. In each subsection, the study of the thermal stability of the film is presented first, followed by the discussion of the EELS of the film. One point worth pointing out is that some of the loss peak values mentioned in this section are measured from their corresponding dominant loss peak, i.e., the SP1-loss peak. If not thus specified, the value has the common meaning and is measured from the elastic peak position.

Before the discussions of the films, let us take a look at the EELS of the Sn. The characteristic plasmon loss spectrum of Sn (a 6.0 ML film) is given in figure 22; the corresponding BP- and SP-loss lines' composition are listed in table 11. Our results show that the first BP- and SP-loss features rise at 10.2 and 13.9 eV respectively and followed by the 25.9 and 39.0 eV peaks in the high energy loss region. The results, 10.2 and 13.9 eV for BP- and SP-loss energy, are reasonably close to the predicted values of 8.96 and 12.7 eV (table 4) although the agreement is not as good as in case of Al. The double and triple BP-loss peaks (25.9 and 39.0 eV) are within a few percentages ($< 2.5\%$) of the theoretical values. For the shoulder labeled as *c* in figure 22, it is hard to decide whether to attribute it to the 2SP-loss or to the SP1BP1-loss, or to a combination of both of these. The above observation is reasonable, since the theoretical values for these two peaks, 17.9 and 21.7 eV, are close to each other (table 11, column 3), and the observed value 20.2 eV is between them. The theory discussed in section 3.2 is perfect for nearly-free-electron metals (such as Al); even though it is not so perfect for other metals (example: the transition metal Ta), it still provides us a very reasonable

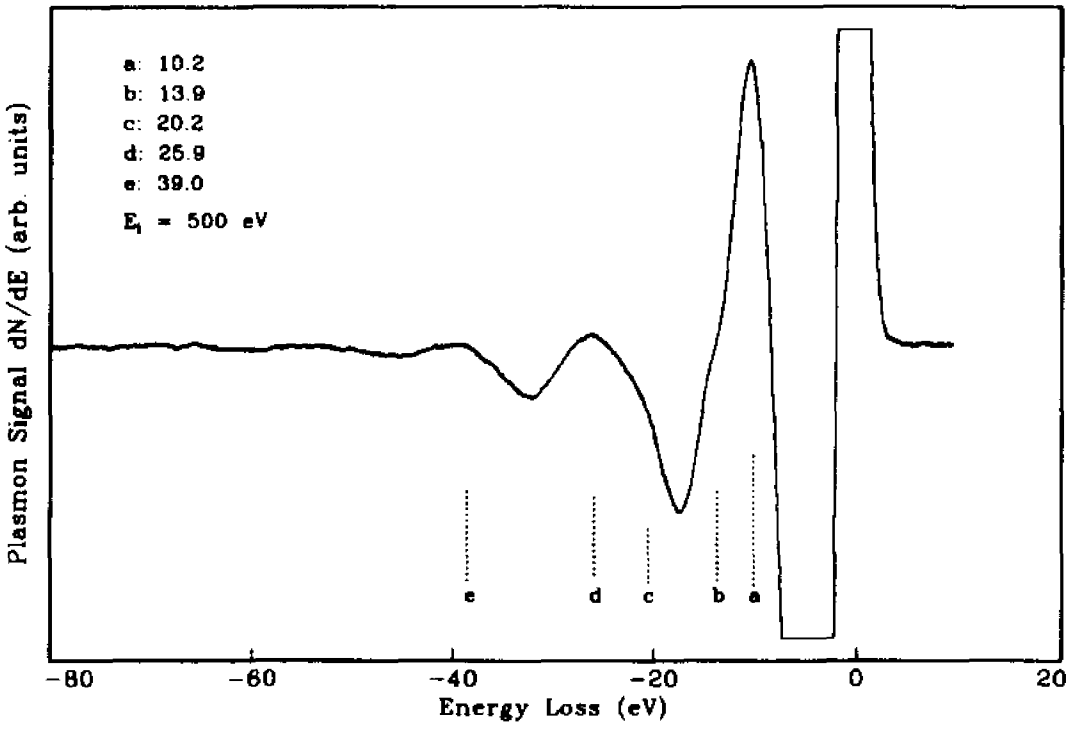

Figure 22. Plasmon loss spectrum of Sn.

Table 11. Plasmon loss positions of Sn (eV)

Experimental Observed	Labels in Figure 22	Theoretical Combinations	Explanation of Column 3*
10.2	a	8.96	SP1
13.9‡	b	12.7	BP1
20.2‡	c	17.9	2SP
20.2‡	c	21.7	SP1BP1
25.9	d	25.4	BP2
no†	–	25.9	SP3
no	–	30.6	SP2BP1
no	–	39.0	SP1BP2
39.0	e	38.1	BP3

*, † and ‡: same as in table 5.

guide. For exact agreement, this means that each individual metal needs its own careful theoretical description due to the different electronic structures.

4.3.1 The Sn/Nb films

4.3.1-1 The Thermal Stability

Sn layers of various thicknesses were grown on Nb at room temperature and annealed at stepwise increasing temperatures up to 1500 K for about 100 seconds. The films' orientations were fixed during the anneals therefore the influence of geometry on the AES peak intensities could be ignored. The Auger amplitude changes of both Sn 430 eV and Nb 161 eV transitions during the processes are presented as a function of annealing temperature; in the hope of that they will provide us information about the films' thermal stability and the possibility of compound formation or alloying. The Sn films were examined by using AES in its derivative form dN(E)/dE.

The results are given in figures 23 to 27. Figures 23 and 24, which are pretreated by the smooth technique mentioned in section 2.5.2 with a smooth range of 101 points, are the plots of several selected Sn and Nb Auger peak shapes during the anneal of a 4.5 ML Sn film. Figure 25 shows the AES peak heights as a function of annealing temperature for a 4.5 ML Sn film on Nb, an eye-aide line is drawn just for easily view reason, and figure 26 shows the effects of temperature on the Nb and Sn AES signal intensities for several Sn film thicknesses.

From inspection of figures 25 and 26, stepwise changes of Auger peak signals for both Sn and Nb are evident. From figure 26 it is clear that the AES signals of

all the films studied show similar thermal stability and changes. Above 1500 K the Sn's AES signal is not detectable. The anneal can be observed as a four-stage process described as follows (figure 25):

(i) the first stage: starts from 300 K extends up to 900 K.

In this region the Sn adlayers are fairly stable. Clearly the AES signals are almost the same at temperatures 300 K and 950 K (figures 23 and 24).

(ii) the second stage: from 900 K to 1170 K.

The Sn's AES amplitude first shows a little increase followed by a sharp drop beginning at approximately 1040 K and continuing until 1170 K. The little bump in the second stage is probably due to an initial disordered (3D-islands) type growth of the film, else more the Sn atoms are inferred to be moving laterally across the sample surface since the sample sides could not be dosed due to sample mounting constraints. Another possible reason for this little increase could be due to the introduced impurities during the deposition of Sn, but our AES finger print did not show any evidence of impurity. So we attribute this initial slow increase to the rearrangement of the Sn atom adlayer, which presumably decreases the number of islands, therefore causes the increase of Sn adlayers' AES signal (in plain language, we may call this effect 'surface smoothing'). A detailed investigation of the growth mode of the Sn films on Nb is given in section 4.4. Following that is a drastic change of both the Sn and Nb AES signals, starting at 1015 K. The rapid drop of Sn AES signal at point 1015 K may due to the formation of either the 3D-clusters of film or to the alloying of the Sn film with the Nb substrate and formation of an ordered Nb–Sn structure.

(iii) the third stage: from 1170 to 1250 K.

In this plateau stage, the decrease of Sn's AES signal is much slower than in the second stage and the Nb's AES signal is almost unchanged during the anneal.

If we consider that the rapid drop in the previous stage represents the start of alloying then the corresponding relatively stable surface alloy may account for the thermal stability of this region.

(iv) the last stage: from 1250 up to 1500 K.

Another drastic reduction of Sn AES signal, accompanied by a slow increase of Nb AES signal, is observed in this stage. Those are due to the alloy decomposition with fast Sn desorption and interdiffusion that occurs above temperature 1250 K.

Very similar four-stage annealing behaviors are also observed for different Sn films thicknesses (1.2, 3.0, 4.0 ML). The results are given in figure 26, where to avoid confusion, no eye-aide lines are drawn. Figure 26 shows a systematic shift to higher temperatures as the thickness of the film increases. In a thicker film there are more Sn atoms, so at a given temperature more time is required for each rearrangement of the structure. The mobility of atoms increases rapidly with temperature, therefore the break point, for changing from the first stage to the second stage, shifts to a higher temperature as the film's thickness increases. Similar temperature-shift effects are also observed for the other three stages from the same figure. The above observations are consistent with Dickey et al's earlier studies of the superconducting properties of Sn films on Nb[4].

The annealing effects on the magnitude and the energy of the films' characteristic plasmon losses (EELS) were also investigated with the results shown in figure 27, where the upper (lower) part shows the annealing effect on the first two loss amplitudes, the initial coverage being used as a parameter. In the lower temperature region (< 900 K), both loss amplitudes show a flat behavior, which is the same as that shows in the plots of the AES heights (the first

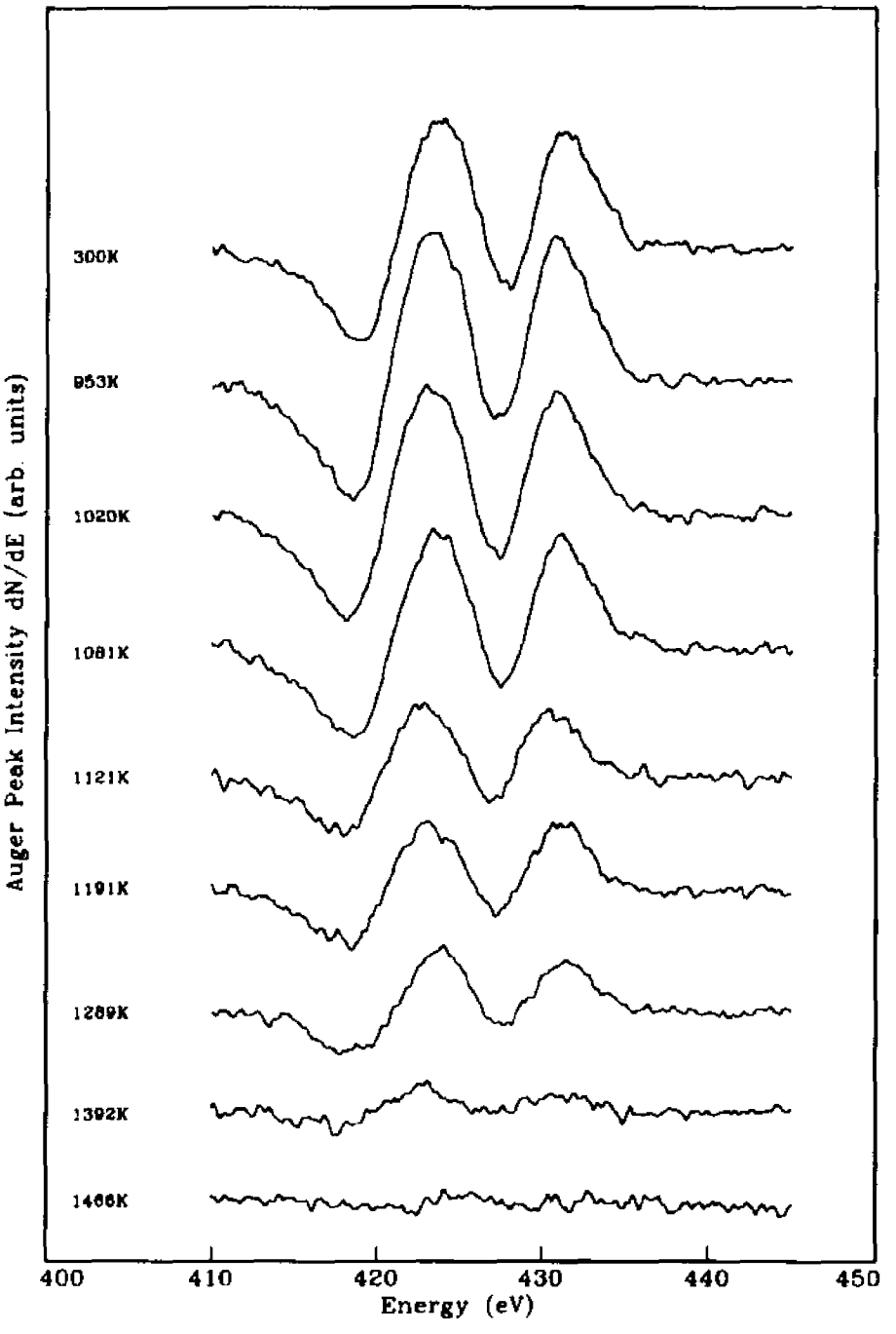

Figure 23. Auger peak shapes of the Sn 430 eV and 425 eV transitions of a 4.5 ML Sn/Nb film during the annealing.

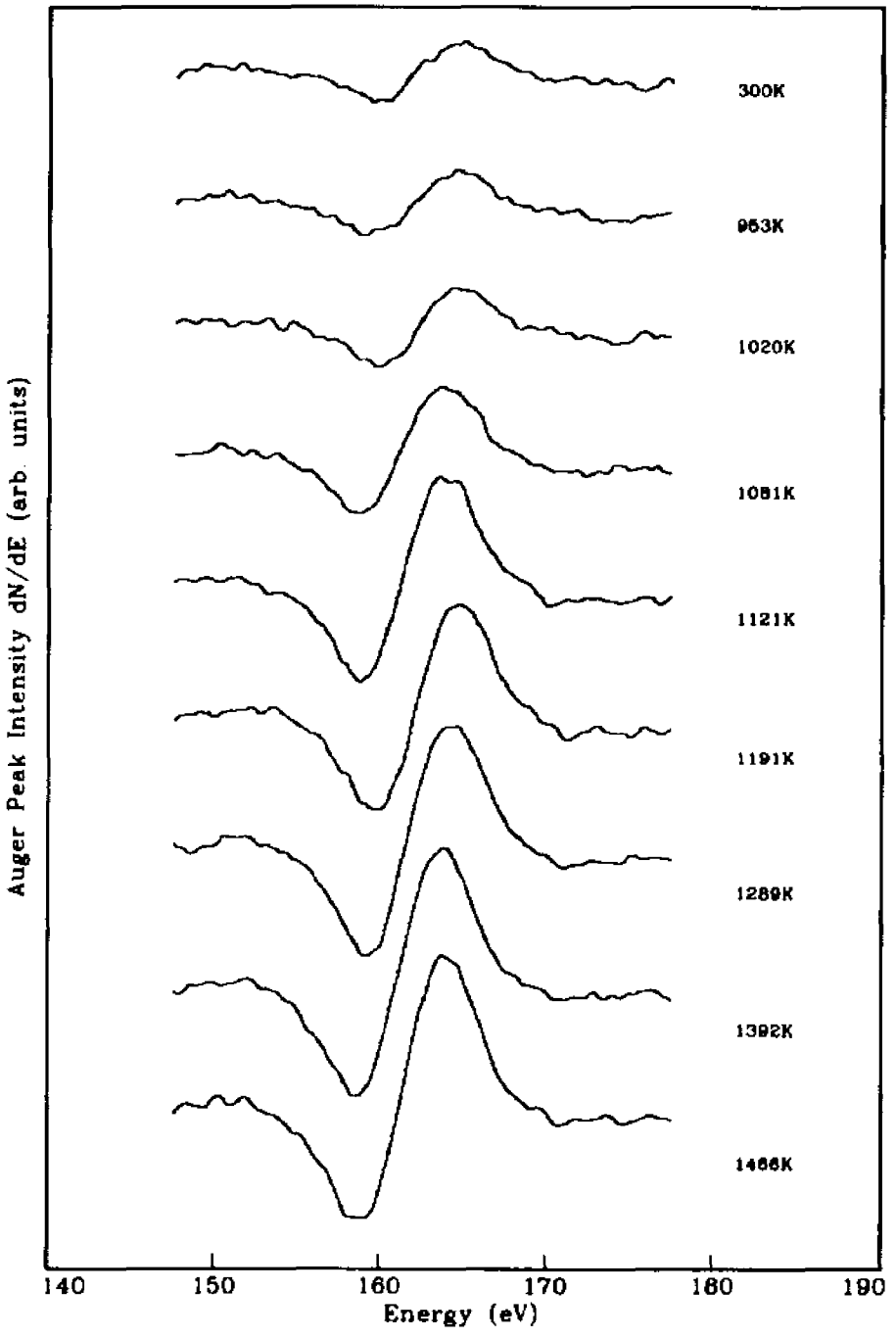

Figure 24. Auger peak shapes of the Nb 161 eV transition during the annealing of a 4.5 ML Sn film on it.

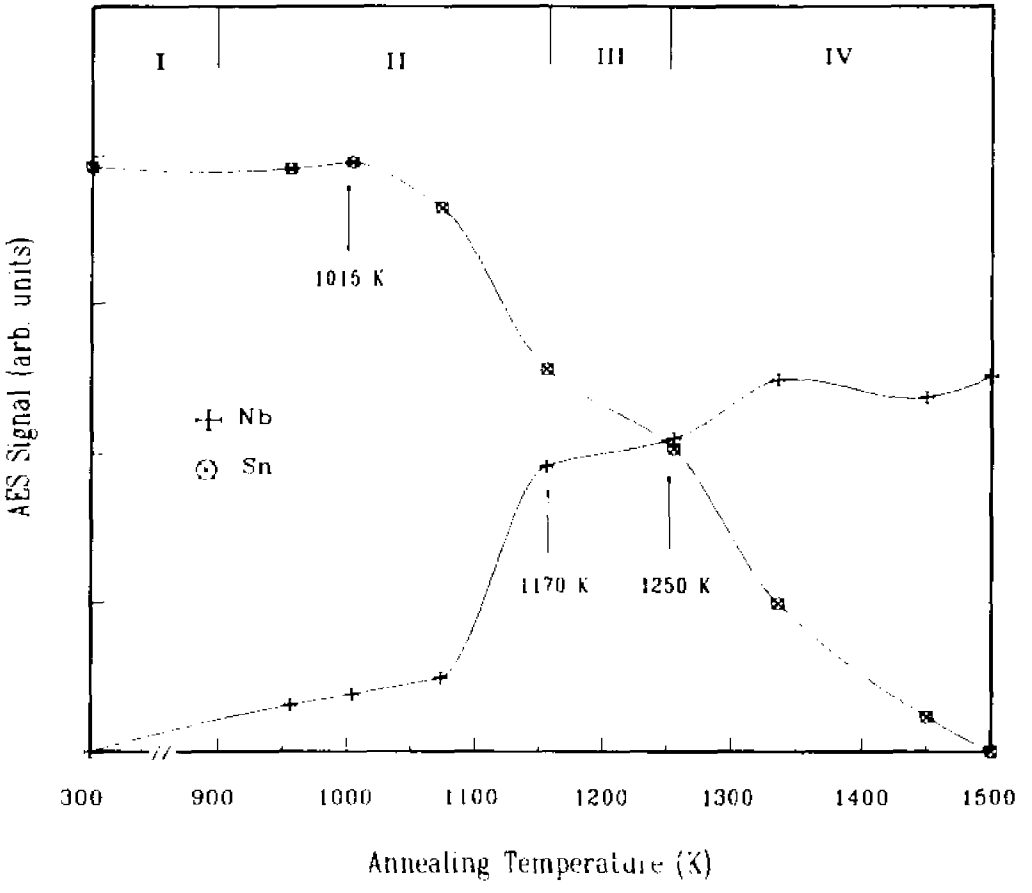

Figure 25. Change of the Sn and Nb Auger amplitudes of a 4.5 ML Sn layer as a function of annealing temperature (100 seconds).

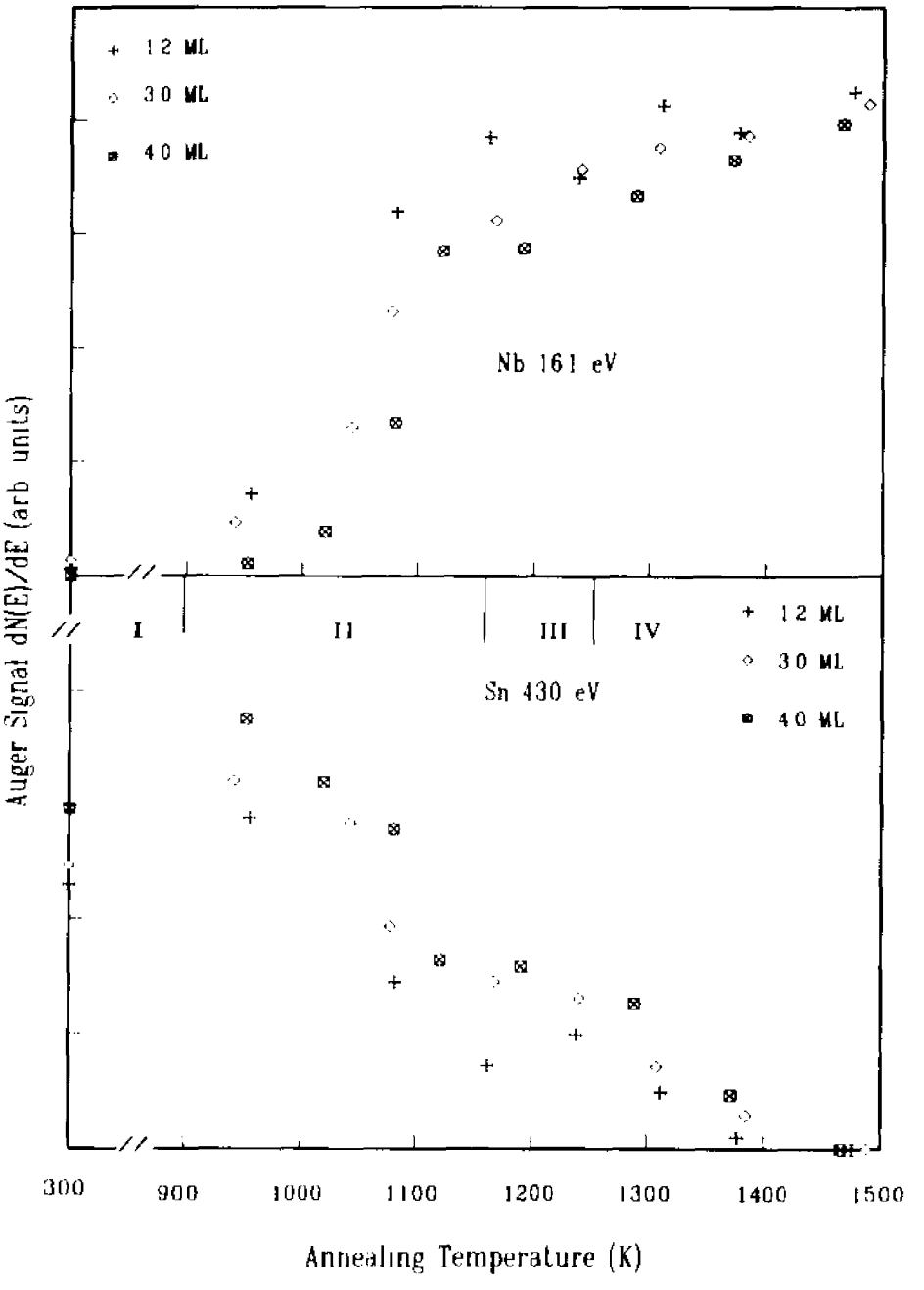

Figure 26 The Sn 430 eV and Nb 161 eV AES signal intensities as a function of the annealing temperature for three Sn films

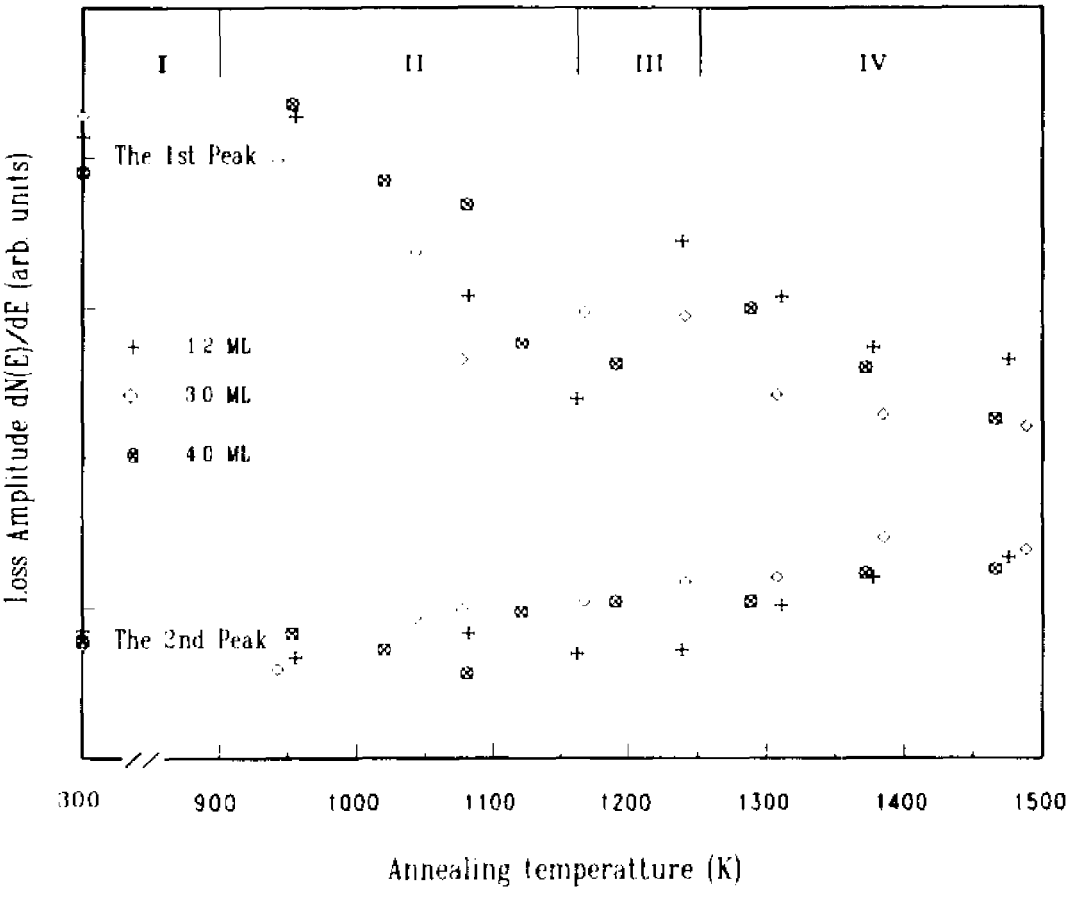

Figure 27 The effect of the annealing on the heights of the dominant loss peaks (Sn/Nb films).

region in figure 25). That feature supports the interpretation of the first stage. The SP-loss shows behavior similar to figures 25 and 26, which gives us further evidence of the four-stage anneal process' interpretation, especially for the second stage (the stage with the little bump in figures 25 and 26). In figure 27, similar bumps also show up around the same temperatures as in the figures 25 and 26. Since the SP1-loss is very sensitive to the surface and our interpretation was that the bump corresponds to the removing of the disordered islands and the rearrangement of the surface layers, the changes of the SP1-loss heights are not surprising.

Overall by carefully investigating the changes in Auger signals of both the Sn and Nb, we can get some information concerning structure changes of the film and possible alloying during anneals.

4.3.1-2 Interface Plasmons of Sn/Nb films

Interface plasmon losses are observed in Sn/Nb films. The experimental IP-loss energy is detected at 16.2 eV and is very close to the predicted value 16.5 eV (table 4).

Our EELS results of a 4.5 ML Sn/Nb film during the anneal are given in figures 28–30. For comparison and completion, the whole spectra of the Sn/Nb film are given in figure 28. In figure 29, which is the zoom view of the *first-pair* of the plasmon loss, the arrows indicate the plasmon loss line shape changes during the anneal. In figure 30, the symbolized shoulders, IP1, are the expected IP1-loss peaks, and the SP1IP1 peaks labeled as 16.3 and 16.1 are clearly observed. In figure 30, in contrast to the case of Al/Nb film, we did not observe the IP1-loss line as an individual real peak but just as a shoulder. The reason may

be that the relative intensity of IP-loss line is much lower than the SP-loss lines' and the IP1-line is buried inside the SP1-loss peak. The amazing thing is that even though we do not observe the individual IP1-loss peak we still see the satellite-accompanied SP1IP1-loss peak which appears at 16.3 and 16.1 (measured from the first loss peak). The 16.1 and 16.3 eV lines are attributed to the SP1IP1-losses, owing to the fact that the higher order loss peaks (labeled as 'Sn-high' in figure 30) in their corresponding spectra are totally vanished. By judging in the same way, we interpret that the 19.4 eV loss line is due to a BP-loss in the Nb substrate instead to an IP-loss of the Sn film, since the higher order loss lines are visible in the corresponding spectrum (labeled as 'Nb-high' in figure 30). In figure 28, the expected IP1- and SP1IP1-loss line positions are pointed by the dash lines marked as 16.2 and 26.4 which are measured from the elastic peak instead of the SP1-loss peak.

During the growth of Sn films on Nb, the EELS measurements were also made. Figure 31 shows a few typical spectra of the characteristic energy loss of the electrons bombarding the Sn/Nb film with an energy of E_i = 501 eV, where the Sn's coverage is taken as a parameter for the curves. The insertion part is the plot of the dependence of the dominant loss peak heights on the coverage. The effect of coverage variation on the magnitude and energy of the characteristic losses can be observed. Besides in the curve symbolized as 0.3 ML the extra structure, which is more likely due to the related IP-loss, is clearly viewed. At a coverage higher than 1.5 ML the spectrum becomes the characteristic EELS spectrum of the bulk Sn.

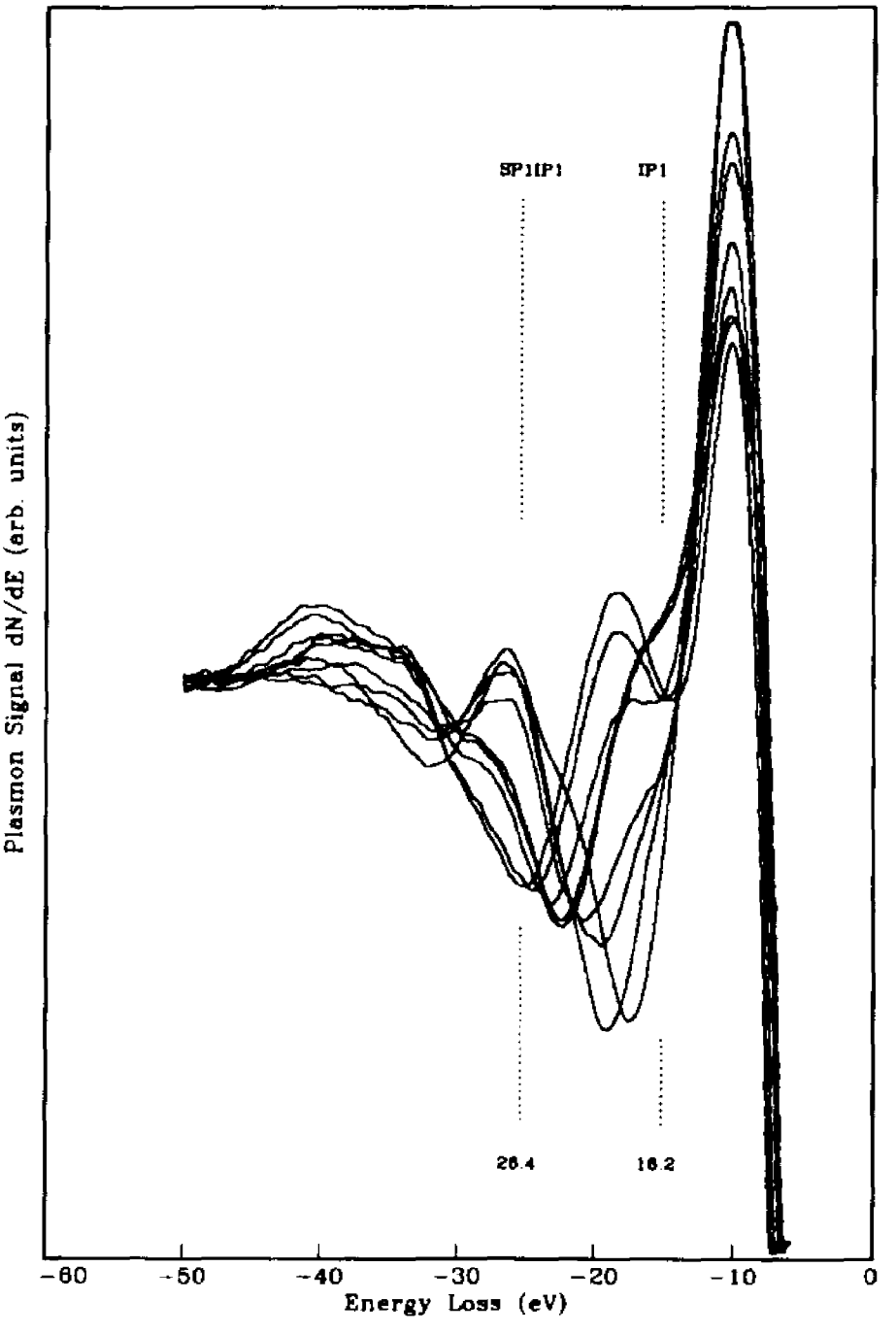

Figure 28. The full spectra of a 4.5 ML Sn/Nb film.

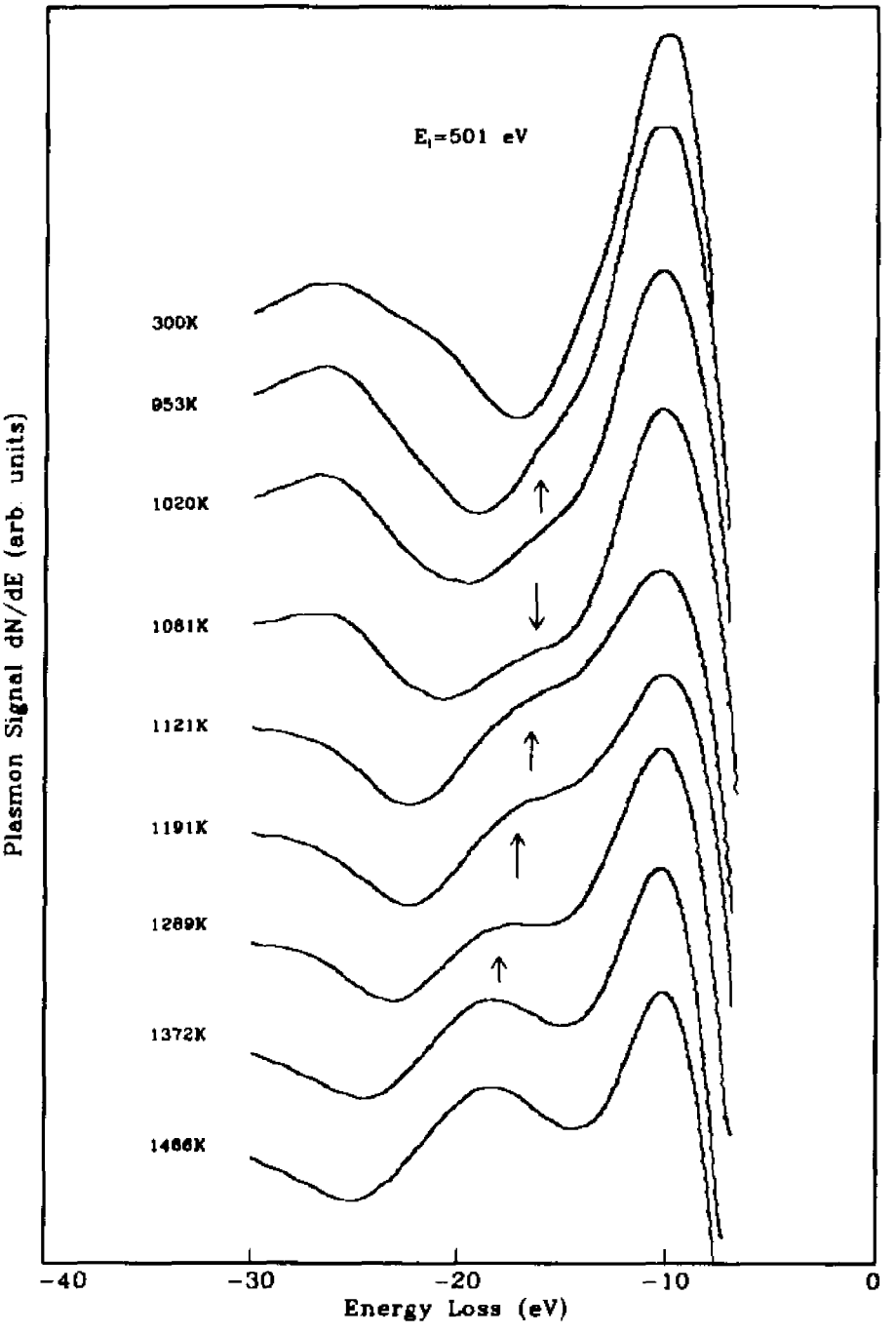

Figure 29. The zoom view of selected curves from figure 28, the arrows designate the line shape changes.

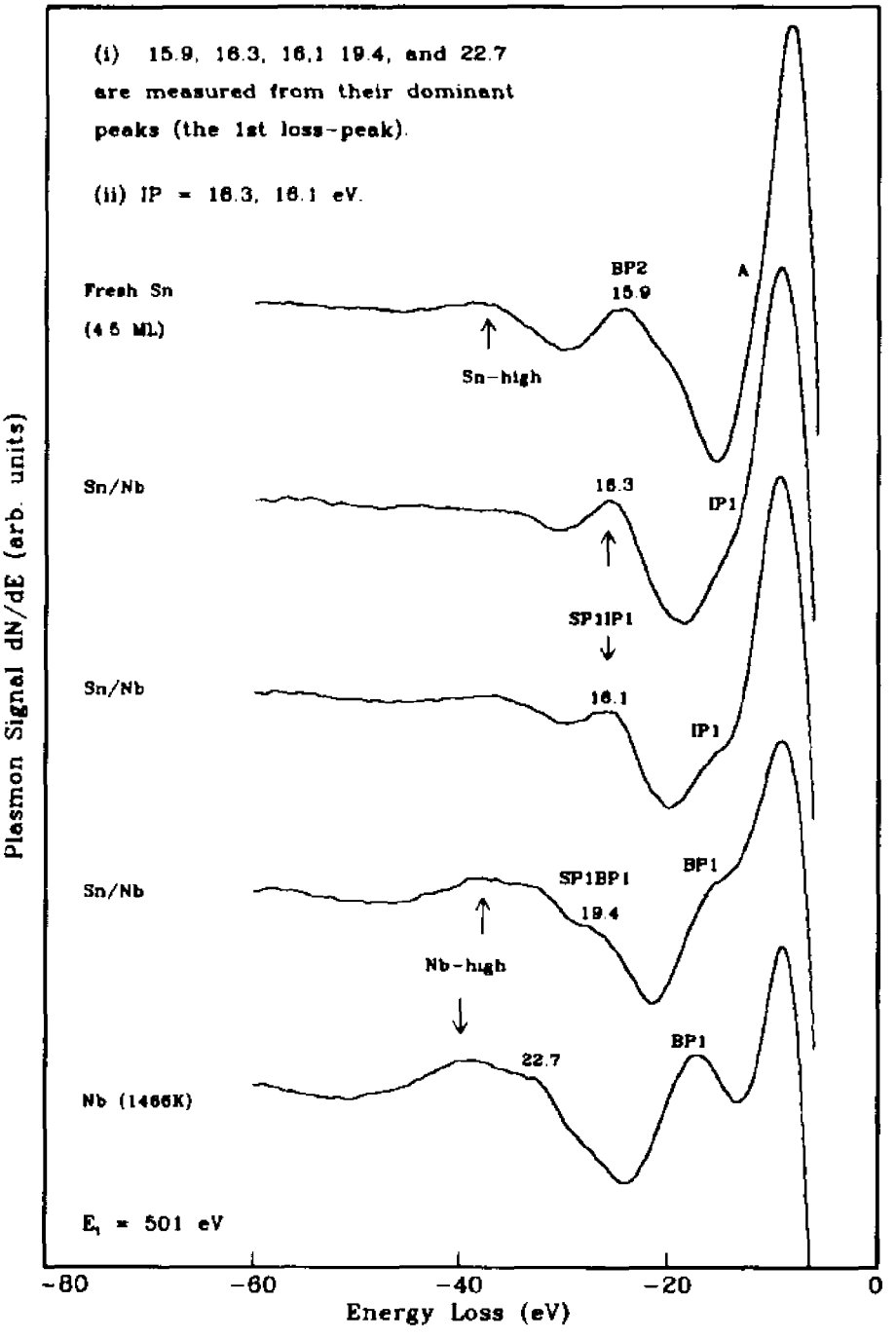

Figure 30. Interface plasmons of the Sn/Nb film, where the measured interface plasmon energy is IP=16.2 eV.

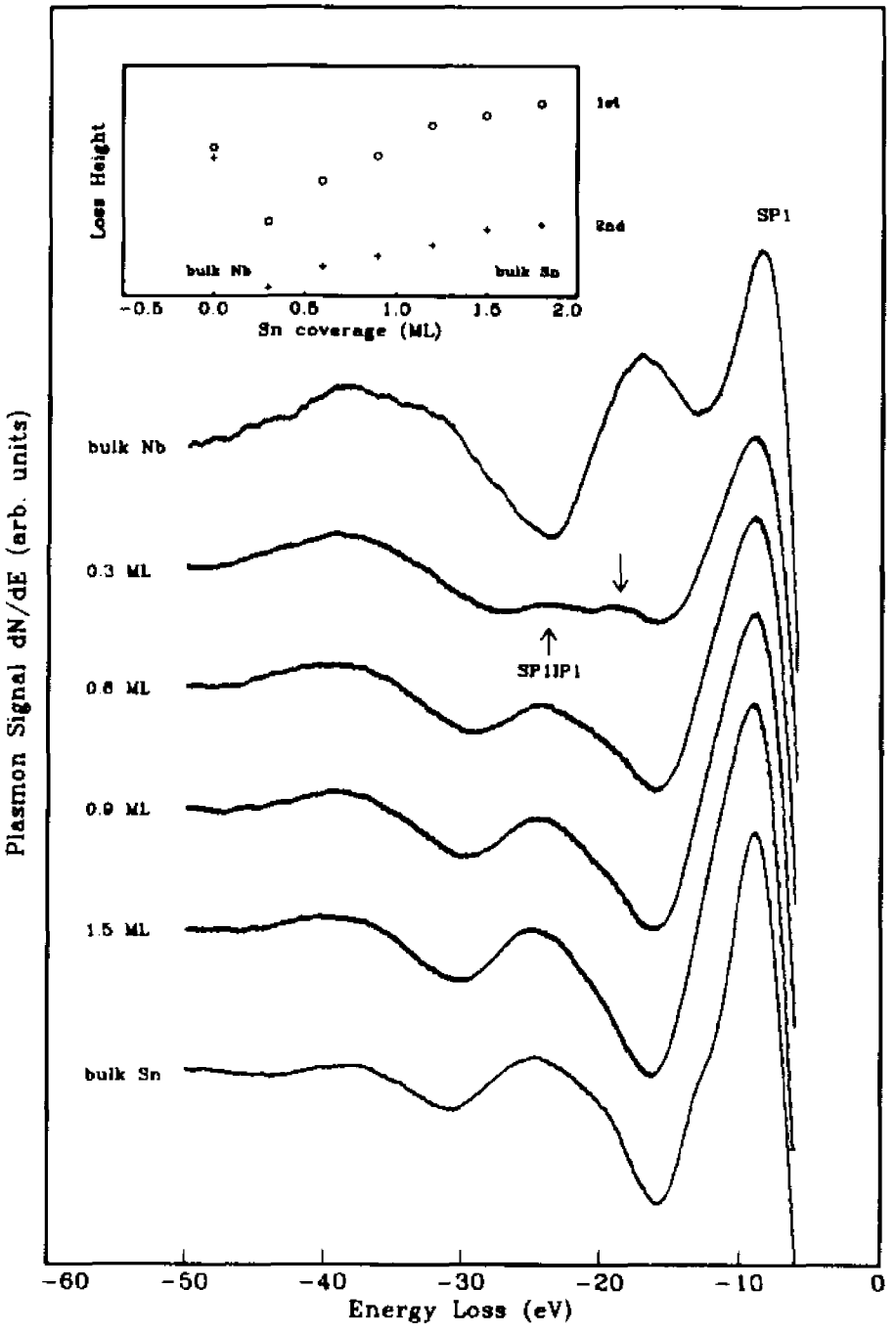

Figure 31. The typical EELS spectra of the dominant peaks during the growth of an 1.8 ML Sn film (on Nb).

4.3.2 The Sn/Mo Films

4.3.2-1 Thermal Stability

Exactly the same measurements as those for Sn/Nb films were also made for the Sn/Mo films. Sn layers of various thicknesses were grown on Mo at room temperature and annealed at stepwise increasing temperatures up to 1500 K for about 100 seconds. The Auger amplitude changes of both Sn 430 eV and Mo 186 eV transitions during the anneals are plotted as a function of temperature. The films were studied in AES' derivative form.

Figures 32 through 36 present the corresponding results. Figures 32 and 33 are the plots of the Sn 430 eV and Mo 186 eV Auger line shapes during the anneal of a 6.0 ML Sn film on Mo. Figure 34 presents the AES peak heights as a function of annealing temperature, in fact that this figure is a zoom view of figure 35 (section *a*) of the 6.0 ML film. The temperature effects on the Sn and Mo AES signal intensities for several Sn film thicknesses are given in figure 35. Also given is the annealing effect on the *first-pair* loss intensities for two thicknesses films (figure 36). Stepwise changes of Auger peak signals for both the Sn and Mo are evident by inspecting figure 34 and 35. As can be seen from figure 34 (or figure 35 section *a*), for the thick layer (6.0 ML), the major changes in the Auger signals of both Sn and Mo may be divided into four stages: 300 to 800 K, 800 to 1120 K, 1120 to 1190 K, and 1190 to 1400 K (in fact that the first and second stages are not well separated). No AES signal of Sn was detected above 1400 K. The AES signals of all the films show similar thermal stability and changes in figure 35, even though it is little hard to see that for the very thin film (0.9 ML). We now examine the four stages one by one (figure 34).

(i) the first stage: 300 K to 800 K.

The Sn adlayers are fairly stable in this region. This becomes apparent by inspecting figure 32 and 33, where both the AES signal heights of the Sn (430 eV) and the Mo (186 eV) are nearly unchanged from 300 K up to 728 K.

(ii) the second stage: 800 K to 1120 K.

The second stage can be attributed to the simple coalescence of islands into a continuous layer (rearrangement to a new structure). The Sn's AES amplitude first shows a little increase starts at around 970 K, followed by a sharp decline beginning nearly at 1030 K and continuing until 1120 K. We interpret that the little bump in this stage is due to the smoothing of initially disordered islands on the substrate. Since no evidences of impurities were viewed in the AES finger prints during the anneal, the rearrangement of the Sn atom adlayer is the preferred interpretation. The rearrangement presumably decreases the number of islands, which in turn causes the increase of the AES signal of the Sn adlayers. Succeeding the bump are the extreme changes of both the Sn and Mo AES signal starting at 1030K. The alloying of the Sn film with the Mo substrate and formation of an ordered Mo–Sn structure or the loss of Sn by vaporisation may be the possible reasons which cause this hasty drop of the Sn AES signal.

(iii) the third stage: 1120 to 1190 K.

In this stage, both the Sn and Mo's AES signal shows an almost flat behavior, where a little decrease (increase) of Sn's (Mo's) signal is observed. If we attribute the hasty drop in the prior stage to the beginning of alloying, then the corresponding relatively steady surface alloy may account for the thermal stability of this region.

(iv) the forth stage: 1190 up to 1400 K.

The clearly visible feature in this region is the bold reduction of Sn's AES signal, accompanied by a very slow increase of Mo's AES signal. The explanation for these changes is most likely due to the alloy decomposition with quick Sn desorption and interdiffusion that occurs above 1200 K.

For comparison and completion, different Sn films thicknesses (2.7 and 0.9 ML) were also analyzed and the results are shown in figure 35. Four-stage annealing behaviors are also observed in these films. When the thicknesses of the films increase, the curves show systematic shifts to higher temperatures. The thicker the film the more the Sn atoms, consequently the more time is required for each rearrangement of the structure at a given temperature. Since the mobility of the Sn atoms increases exponentially with temperature, the shift of the break point, for changing from the first stage to the second stage, is expected. The very thin film, (0.9 ML), probably does not correspond to a complete layer of Sn on the Mo, and so is a special case and does not reveal all the four stages so clearly (figure 35 section *c*). The above observations are very similar to the Sn/Nb films which were just discussed.

In order to get confirmation of the former descriptions about the anneal process, the annealing effects on the magnitude and the energy of the EELS were also examined. The EELS results are shown in figure 36, where the initial coverage is used as a parameter of the plot. In each section of the figure, the upper (lower) curve corresponds to the annealing effect on the first loss (second loss) of the *first-pair* loss peaks. A very flat behavior of both the loss amplitudes is observed in the lower temperature region (< 800 K), which is consistent with the observation of the AES plots (the first region in figure 34 and 35) that no changes occur at these low temperatures. In the higher temperature region (> 1200 K), where the desorption of the Sn happens, the amplitude of the second

loss peak increases with the temperature. The above observed features provide us other evidences for the previous interpretations of the first stage and the last stage. The SP1-loss shows behavior similar to figures 34 and 35, which gives us further support for the four-stage anneal process' interpretation, especially for the second stage (the stage with the little bump in figures 34 and 35). In figure 36, these bumps, indicated by the two-direction arrows with the corresponding temperatures, can be clearly viewed. One would expect that the SP1-loss be very sensitive to the surface and if the little bump corresponds to the removing of the disordered islands and the rearrangement of new structures, the changes of the SP1-loss heights confirm the earlier interpretation of this stage. However, the SP1-loss heights do not show so clear behaviors as that observed in the AES plots at the two end regions, since one end (at lower temperature) of the SP1-loss plot corresponds to the Sn's dominant peak while it is the Mo's SP1-loss that dominates the spectrum on the other end (at higher temperature). Overall, figure 36 provides a side evidence for the anneal process just discussed, and confirms the interpretations of the first stage where nothing happens, the second stage where the structure changes, and the last stage where the loss of the Sn happens. In the next section we examine the EEL spectra in detail.

One point worthy to mention is that very similar results are obtained for the Sn films on Nb and Mo. The Sn films go through the same sequence of changes although at slightly lower temperatures for Mo than for Nb. The similarity is not unexpected since Nb and Mo are neighbours in the periodic table and their electronic configurations differ by just one *d* electron (Nb: $4s^2 4p^6 4d^4 5s^1$, Mo: $4s^2 4p^6 4d^5 5s^1$).

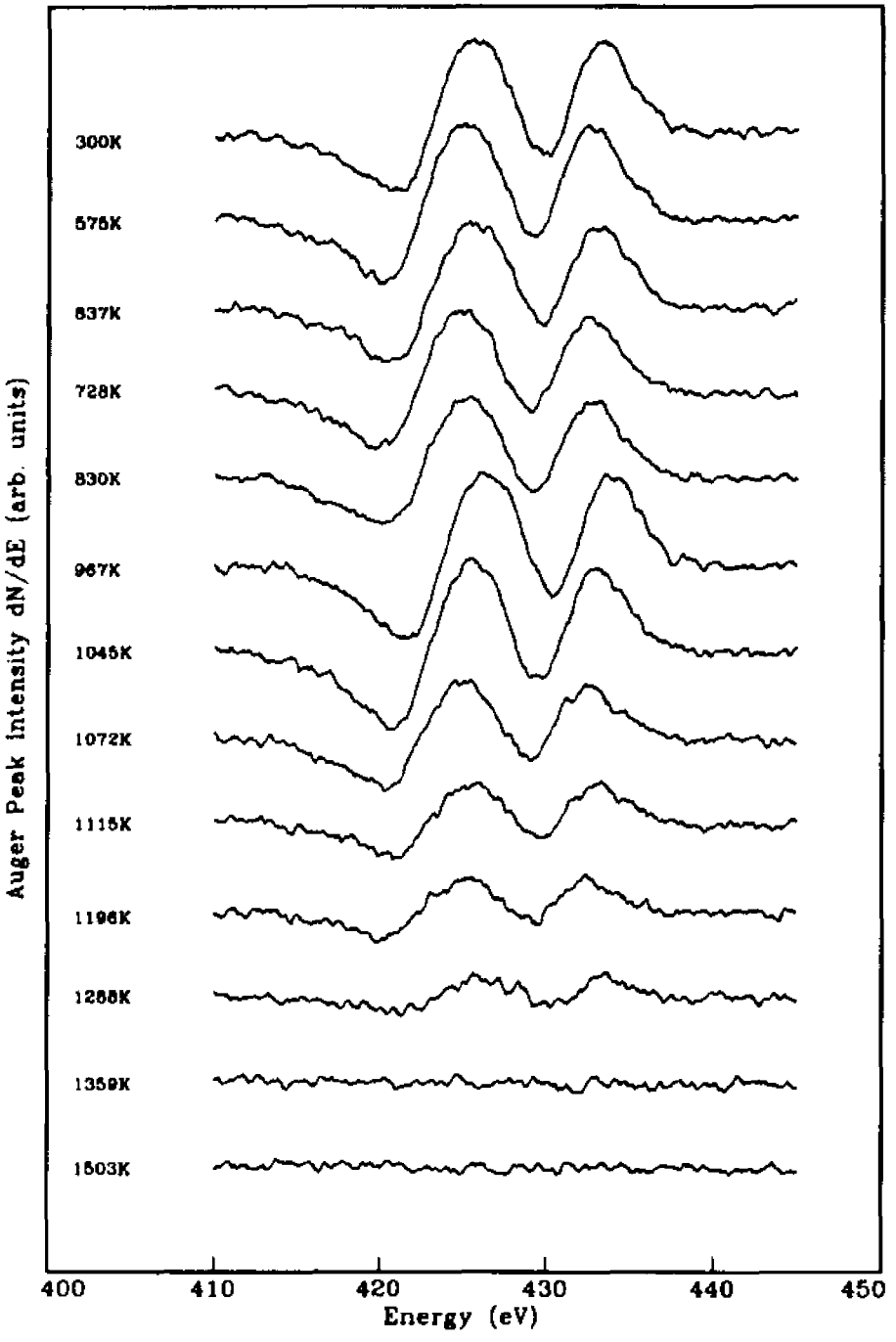

Figure 32. Auger peak shapes of the Sn 430 eV and and 425 eV transitions from a 6.0 ML Sn/Mo film during the anneals.

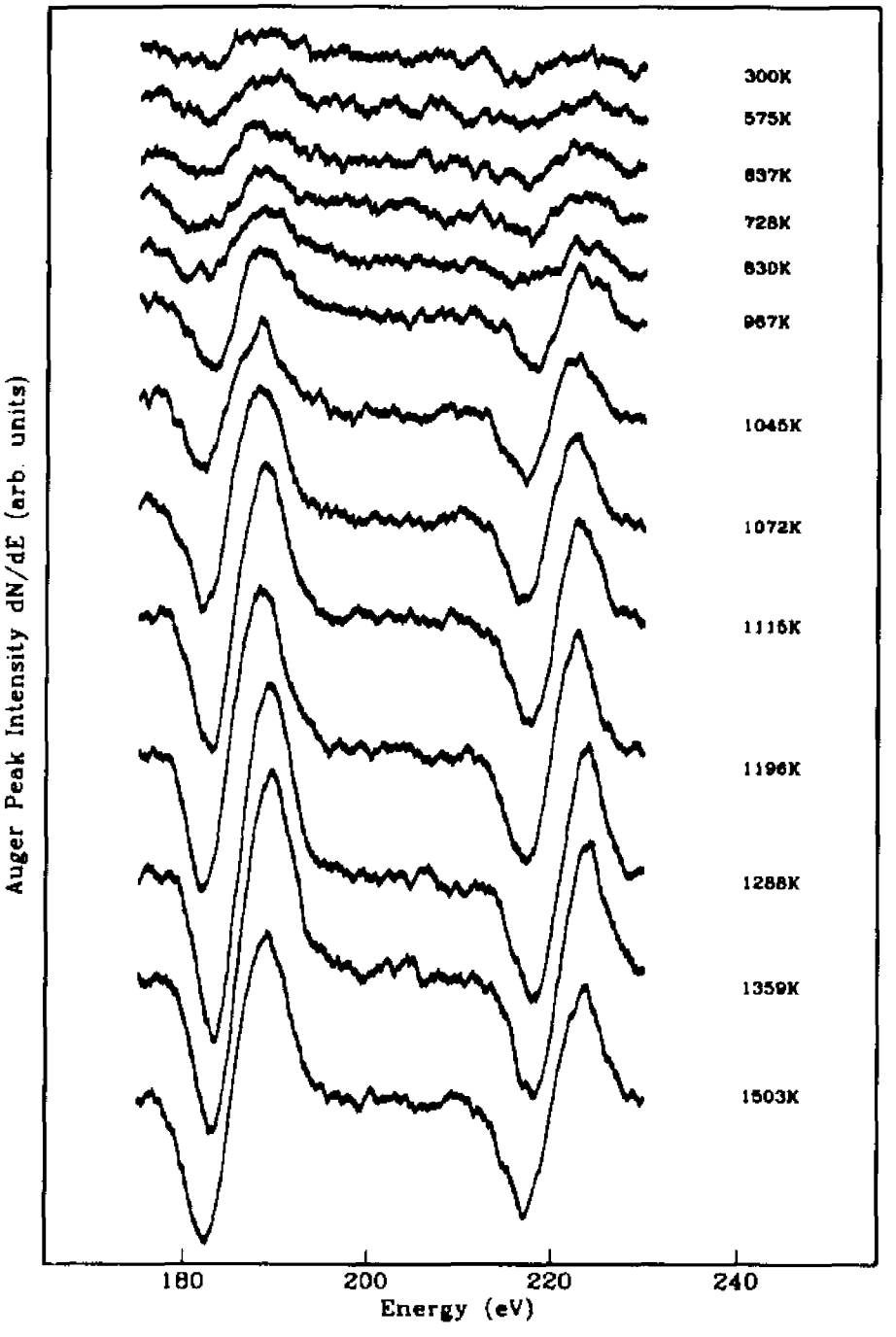

Figure 33. Auger peak shapes of the Mo 186 eV transition during the anneal of a 6.0 ML Sn film on it.

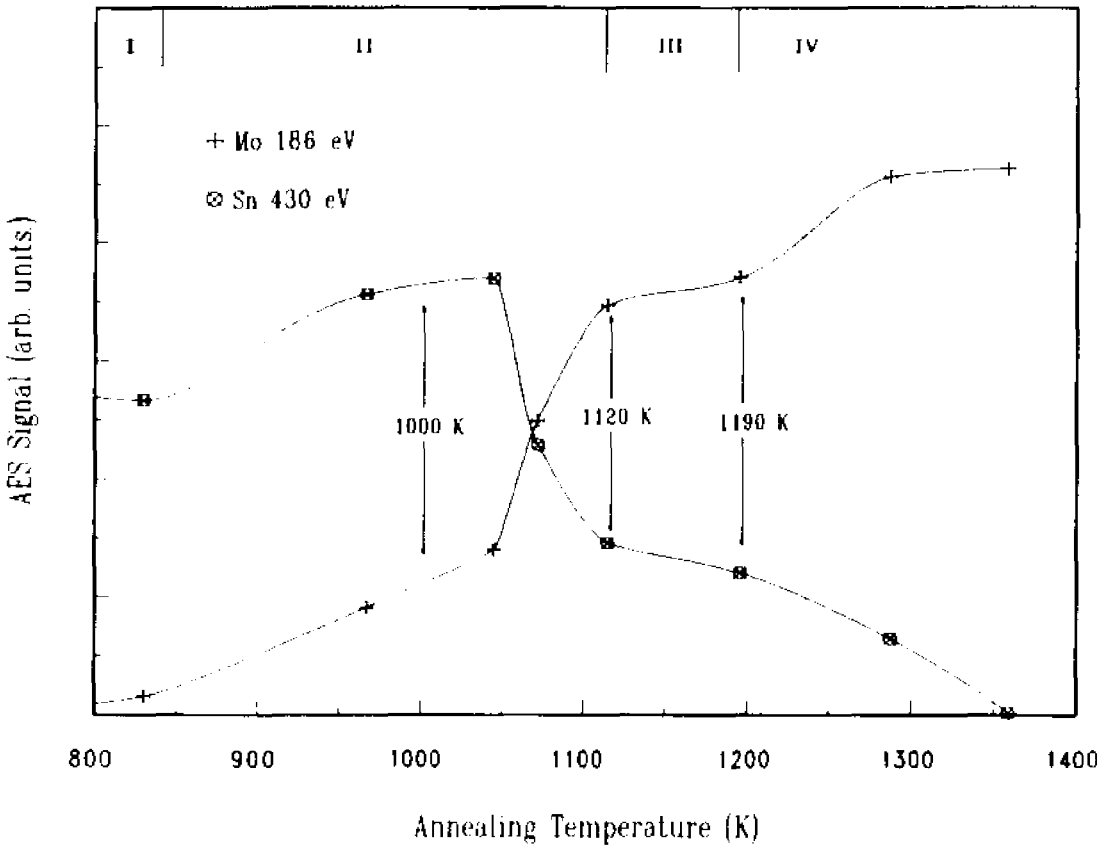

Figure 34 Changes of the Sn and Mo Auger amplitudes of a 6.0 ML Sn layer as a function of annealing temperature

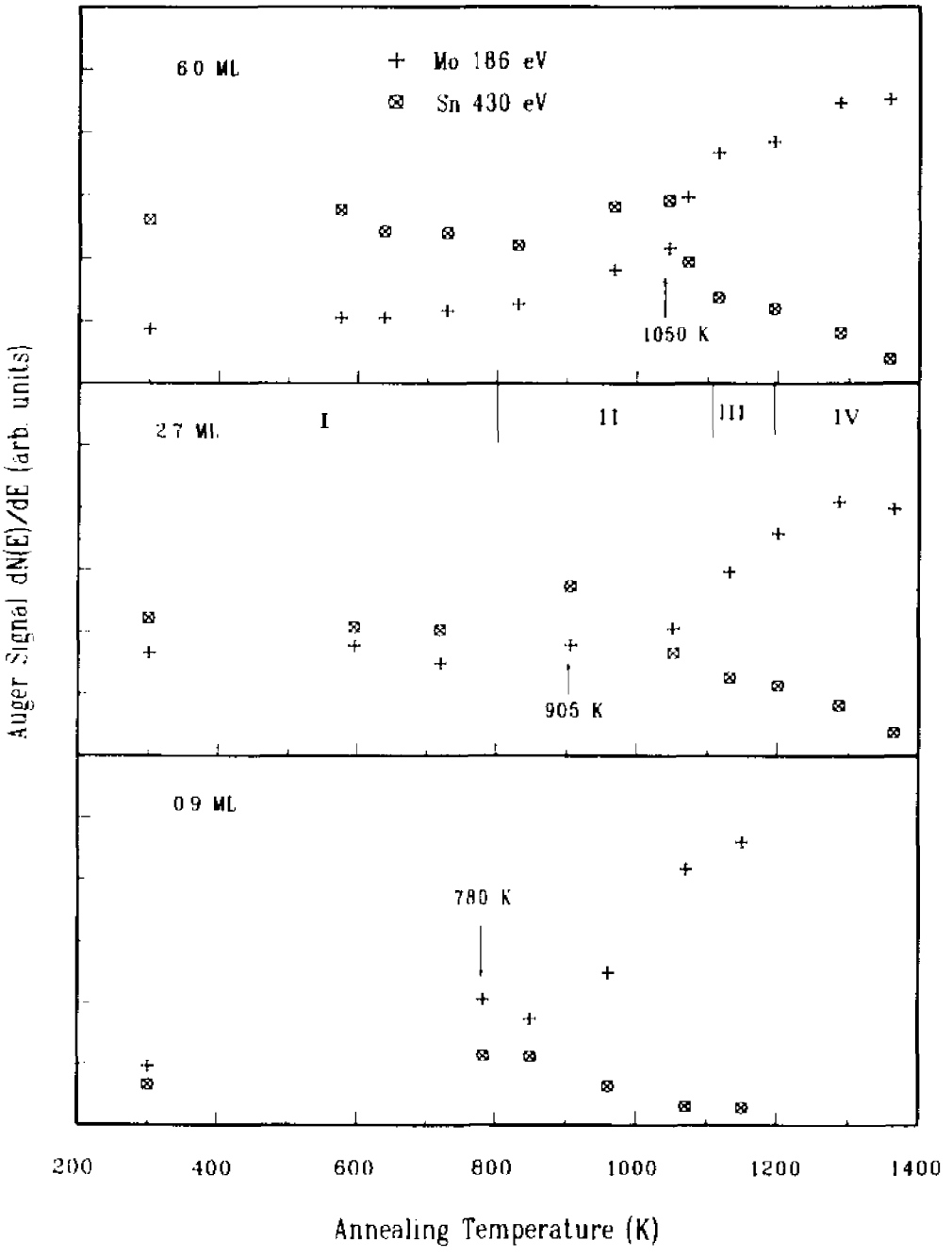

Figure 35. The Sn 430 eV and Mo 186 eV AES signal intensities as a function of annealing temperaure (three thicknesses Sn films).

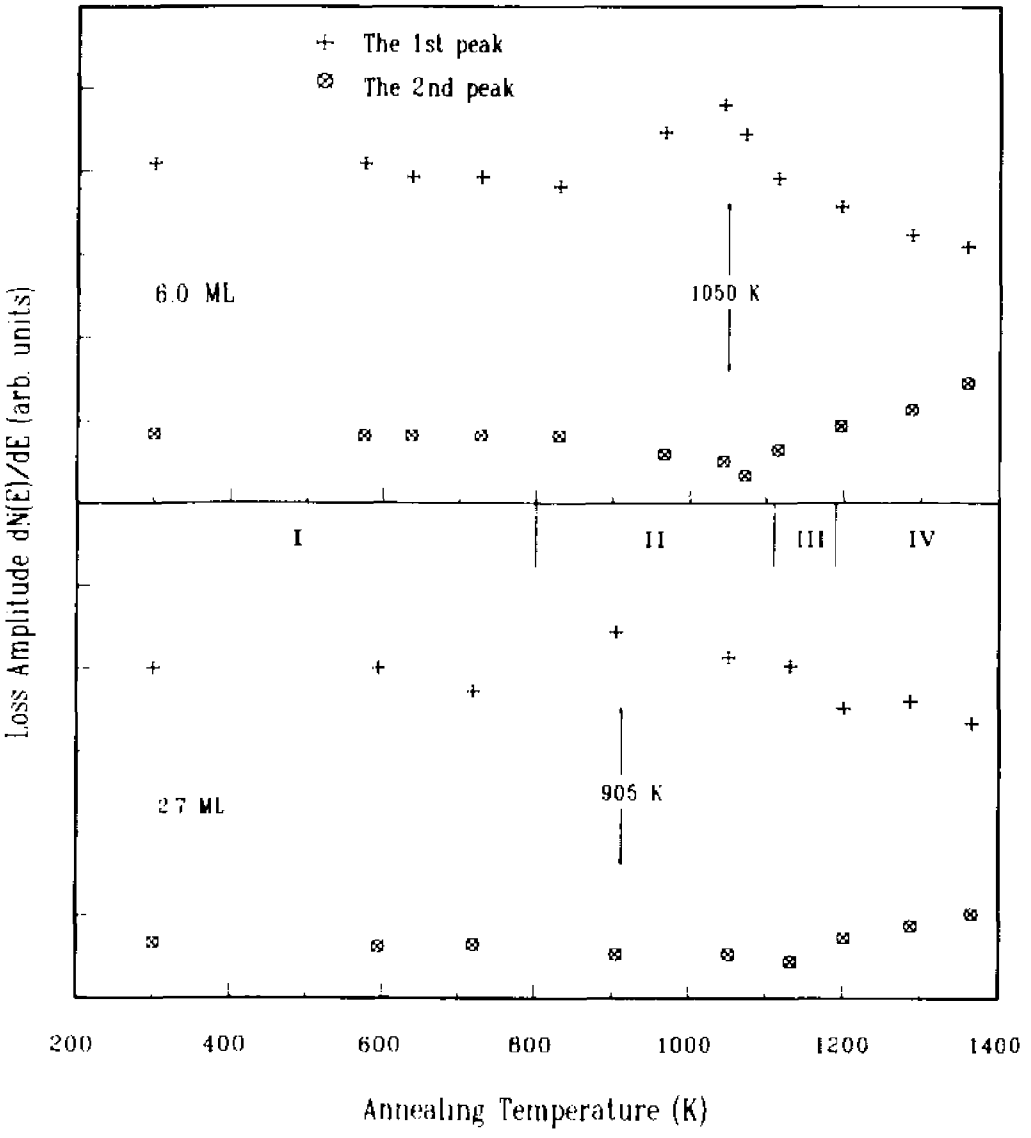

Figure 36 The annealing effect on the heights of the dominant loss peaks (two thicknesses Sn films).

4.3.2-2 Interface Plasmons of Sn/Mo films

(i) EELS *of Mo*: The characteristic EELS of the Mo (foil)[116] is shown in figure 37; the relevant BP-loss, SP-loss, and the possible combinations for multiple losses are enumerated in table 12. Exactly the same techniques are used with similar experimental parameters as for the earlier metals. Our results bear out that the first BP- and SP-loss features rise at 11.4 and 22.0 eV separately and followed by the 44.3 and 67.2 eV peaks in the high energy loss region. Unlike the previous metals the spectrum does not have a shoulder to the right of the BP2-loss peak (labeled as *c*), however this peak is unusually broad which may imply the existence of hidden 2SP- and SP1BP1-losses. The values predicted by the simple free electron model are 16.3 and 23.1 eV for SP- and BP-loss respectively. The values for the bulk plasmons are close, however for Mo, while the observed SP1 values are smaller than predicted.

(ii) Interface plasmons of Sn Mo films: Interface plasmon losses are observed in Sn/Mo films as well. The experimental IP-loss energy is 15.6 eV in average and is reasonably close to the calculated value 18.6 eV (table 4).

Our EELS results of a 6.0 ML Sn/Mo film during the anneal are given in figures 38–40. For comparison, the intact spectra of the Sn/Mo film during the anneal are given in figure 38, where the anticipated IP1- and SP1IP1-loss positions are pointed out by the dash lines marked as 15.6 and 25.8 which are measured from the elastic peak. In figure 39, which is the zoom view of the first two pairs of the spectra, the series of arrows (labeled as 'A', 'B', and 'C') indicate the line shape changes during the anneal. The arrows 'A' indicate the changes of the shoulders, which are classified as the Sn's BP1-loss. The arrows 'B' designate, respectively, the line shape changes of: the 2SP- (or SP1BP1-) loss of the Sn, the

2SP-loss of the film and the BP1-loss of the Mo. The arrows 'C' point the changes of the BP2-loss of the Sn and the SP1IP1-losses of the film. The same sequence of the changes is also symbolized separately as 'A', '2SP', and 'BP2' (also 'SP1BP1') in figure 40, where several typical spectra during the anneal are shown. The detailed description of the loss lines and their corresponding explanations are given as follows:

ii-1) The Sn's EELS *spectra* (the first two curves in figure 40):

Certainly, the first curve is the Sn's characteristic EELS, where the two shoulders labeled as 'A' and '2SP' are attributed to the BP1- and 2SP- (or SP1BP1-) losses. The second curve is also very similar to the Sn's characteristic EELS, since the higher order losses (indicated by 'Sn-high'), as well as the two shoulders, especially the one labeled as 'A', are all clearly seen in the spectrum. The BP2-loss is higher in the first curve, which is the spectrum of the fresh film, than in the second one, which corresponds to an annealed film. On the contrary, the 2SP-shoulder becomes even clearer in the second than in the fresh one. Because of the migration of Sn atoms, when the temperature increases the film becomes thinner, consequently the BP-losses become weaker while the SP-losses presumably remain unchanged; as a result of the fact that the intensity of the BP-loss depends on the film thickness, whereas the SP-loss intensity is independent of the thickness. In addition, this observation also strongly supports the classification of the second shoulder as a SP-loss related (symbolized as '2SP'), even though it is a little hard to decide whether attribute it to the 2SP-loss or to the SP1BP1-loss or to both of them (table 11 row 4 and 5).

ii-2) The interface plasmons (the third and the forth curves in figure 40):

In the third and the fourth curves, new structure is apparent. We interpret that the peaks, 15.5 and 15.7, are due to the SP1IP1-losses of the film. An evidence

for this categorizing is that neither the Sn's nor the Mo's higher order plasmon loss lines are visible in the spectra. The other evidence is that the shoulder labeled as 'A', which is classified as the BP1-loss of the Sn, is not observed in these two curves. In contrast, the 15.7 peak, especially the 16.0 one (in the first two curves), is attributed to the Sn's characteristic BP2-loss line instead of the SP1IP1-loss of the film; because as just discussed, both spectra are similar to the Sn's characteristic EELS.

The other peaks marked as '2SP' are attributed to the 2SP-loss of the film. This loss peak is higher in the fourth curve, which corresponds to an annealed film at higher temperature, than in the third one; while the corresponding SP1IP1-loss line behaviors just in the opposite way. As the temperature increases the thickness of the film becomes thinner due to lose of Sn atoms, so the height of the SP1IP1-loss, which likely depends on the thickness of the film, decreases. On the other hand the height of the 2SP-loss, which presumably is independent of the thickness, remains unchanged.

Now back to figure 38, if the above interpretations about the IP-losses of the film are accepted, then the question why the IP1-loss is not observed, could be answered as follows. As one can clearly see in the figure, the anticipated IP1-loss line lies near the valley of the SP1-loss line which unfortunately has a much higher intensity and consequently buries the expected IP1-loss line. Similar observations are obtained for the Sn/Ta films which will be discussed next.

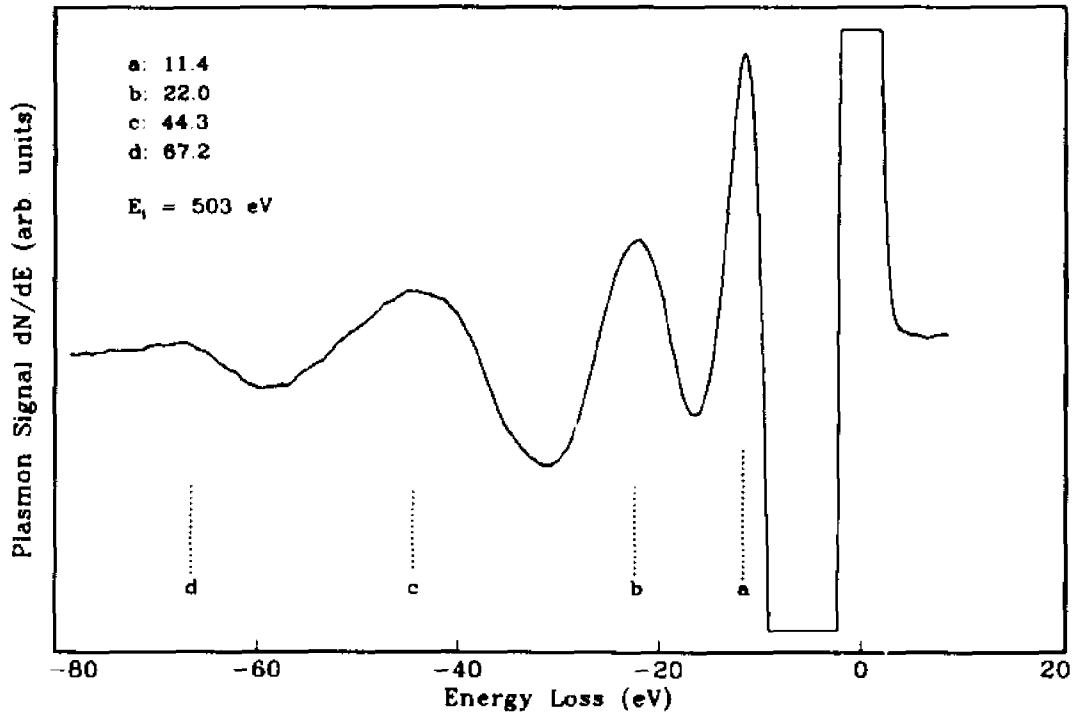

Figure 37. Plasmon loss spectrum of Mo.

Table 12. Plasmon loss positions of Mo (eV)

Experimental Observed	Labels in Figure 37	Theoretical Combinations	Explanation of Column 3*
11.4	a	16.3	SP1
22.0	b	23.1	BP1
no‡	–	32.6	2SP
no	–	39.4	SP1BP1
44.3	c	46.2	BP2
no	–	48.9	3SP
no	–	62.5	BP2SP1
67.2	d	69.3	BP3

* and ‡: same as in table 5.

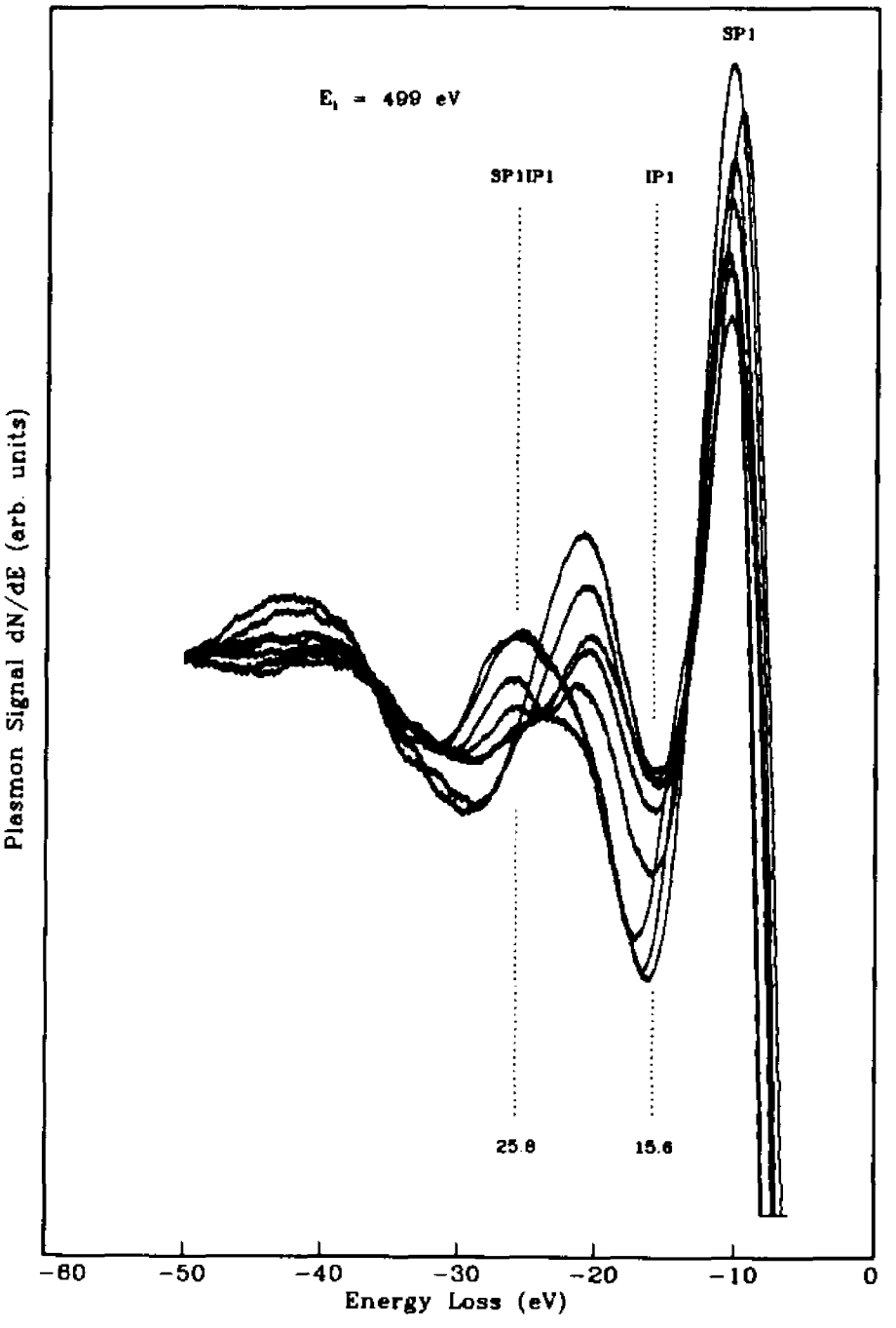

Figure 38. The full spectra of a 6.0 ML Sn/Mo film, the zoom view of the plasmon losses is given in figure 39.

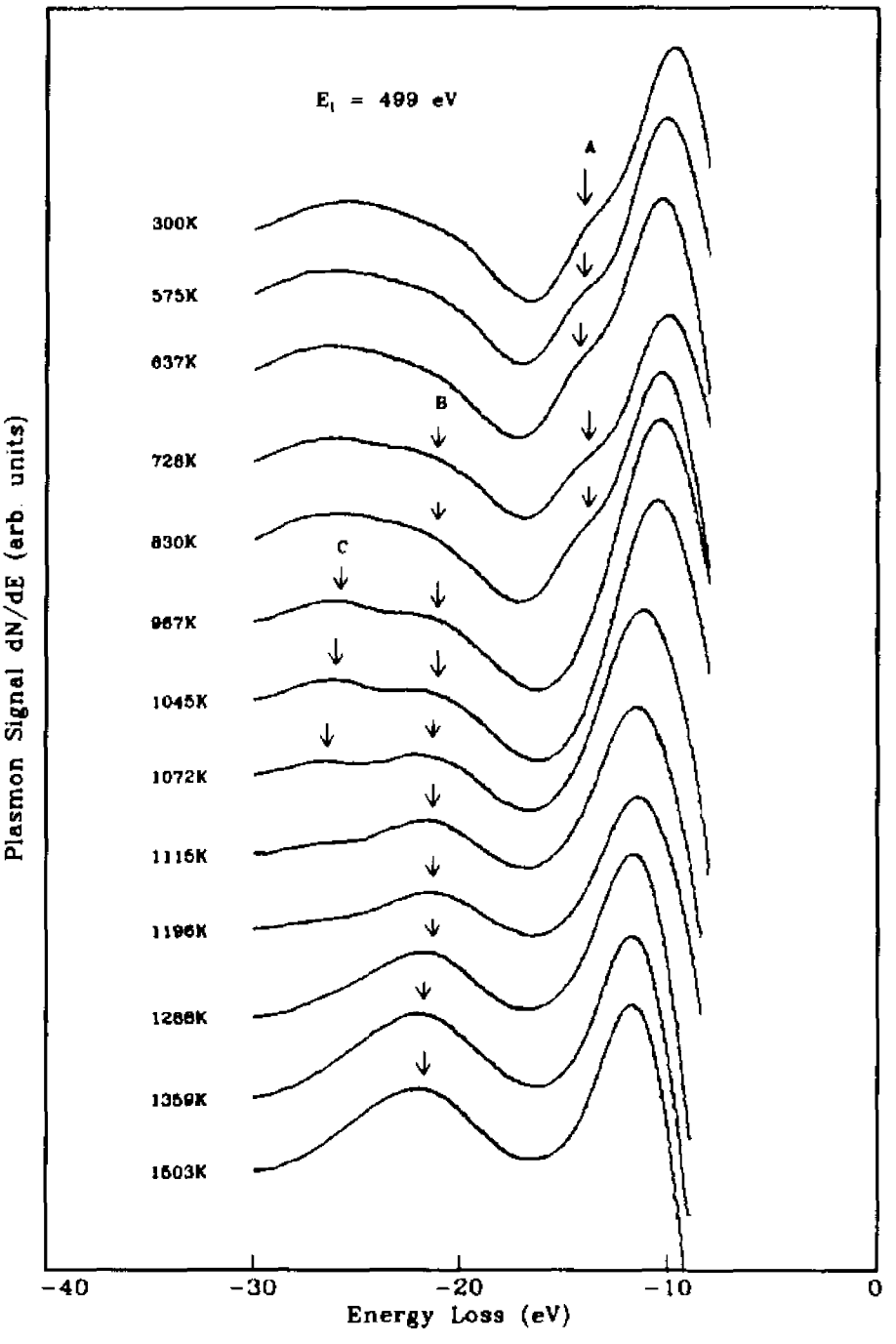

Figure 39. The EELS spectra of a 6.0 ML Sn/Mo film during the anneal, arrows indicate the line shape changes.

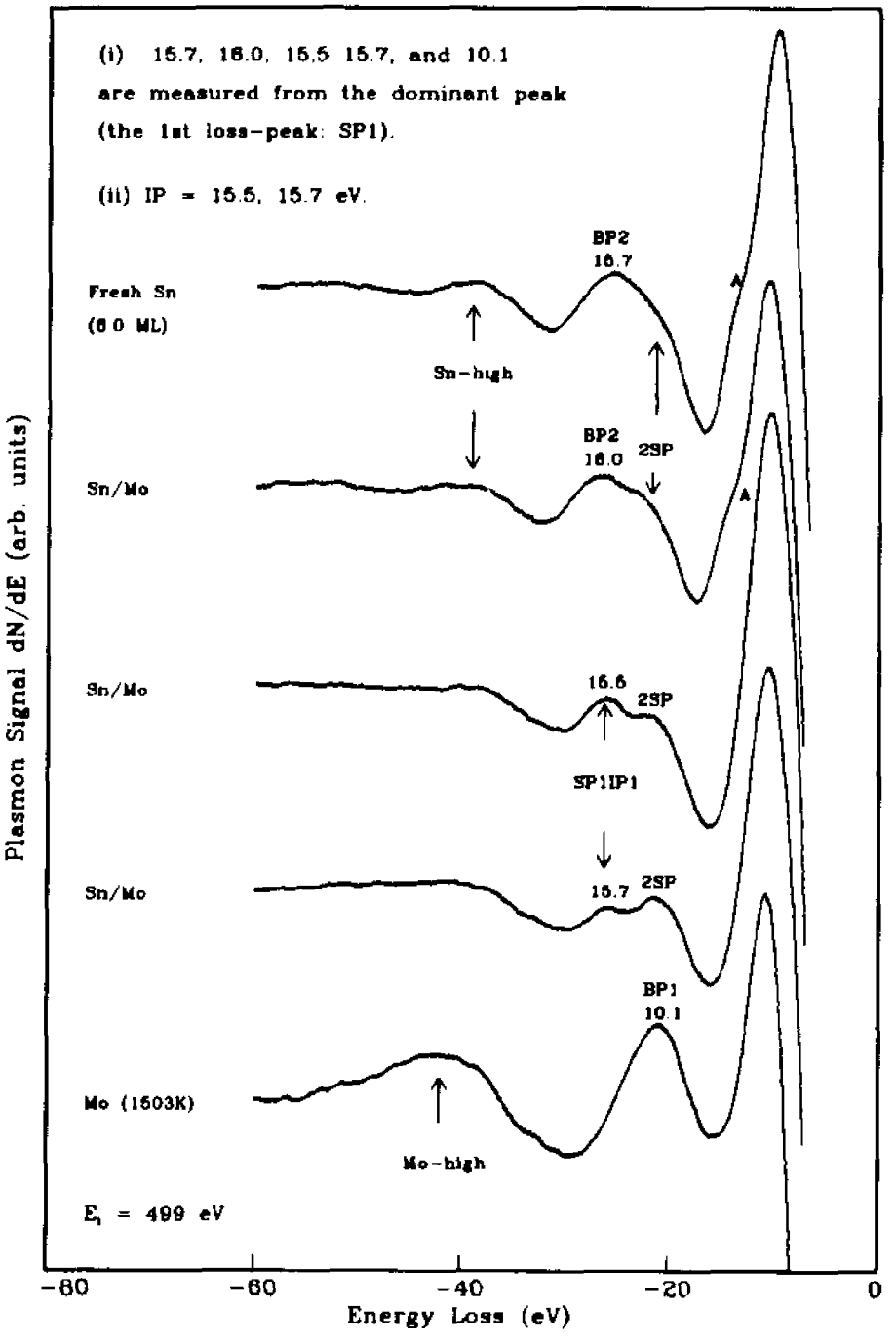

Figure 40. Interface plasmons of the Sn/Mo film, where the measured interface plasmon energy is IP=15.6 eV.

4.3.3 Interface Plasmons of Sn/Ta films

We also analyze the EELS of Sn/Ta films and the probable interpretation of the plasmon loss features is presented. The experimental measured IP-loss energy is 15.8 eV in average which is very close to the calculated value 16.5 eV (table 4). The SP1IP1-loss manifests itself as a real peak; while the IP1-loss line is faintly visible, presumably it is buried by the SP1-loss or the 2SP-loss or both of them. The SP1IP1-loss lines are recognized and interpreted by using the same judgment as that used for other films, i.e., the loss lines are distinguished as the relevant IP-losses only when neither the Sn's nor the Ta's higher order plasmon loss lines are visible.

Sn layers of various thicknesses were grown on Ta at room temperature and annealed at stepwise increasing temperatures up to 1500 K for about 100 seconds. The orientations of the films were fixed during the anneal. Figures 41 through 43 show our EELS results of a 2.0 ML Sn/Ta film during the anneal. Figure 41 shows the complete spectra of the Sn/Ta film, where the anticipated IP1- and SP1IP1-loss positions are pointed by the dash lines marked as 15.8 and 26.0 which are measured from the elastic peak. Drastic line shape changes, owing to the significant difference between the characteristic EELS of the Sn and Ta, can be clearly seen in this figure. In figure 42, which is the zoom view of figure 41, the arrows indicate the plasmon loss line shape changes during the anneal. The double-arrows point the line shape changes of the 2SP-loss (the peaks symbolized as '2SP' in figure 43). The single arrows are for the BP2- or the likely SP1IP1-loss lines (which correspond to the dash line named as 26.0 in figure 41, and the peaks 15.8 and 15.9 marked as 'SP1IP1' in figure 43).

In figure 43, the spectra symbolized as 'Bulk Ta' and 'Bulk Sn' are, separately, imported from different runs of a clean Ta foil and a fresh Sn film (20 Å), and are used as references. In the fourth curve, the peak 17.5 is attributed to the SP1BP1-loss of the Ta, because all the Ta's higher order plasmon loss lines are clearly observed. Therefore this curve is similar to the Ta's characteristic EELS spectrum (curve 5), but differs a little due to the very small amount of Sn remaining in the film.

Next, we will concentrate on the second and the third curves which reveal new structures. As can be seen from these two curves, the SP1IP1-loss line, labeled as 15.8 and 15.9 becomes visible after the vanishing of the Sn's higher order BP-loss lines (indicated by 'Sn-high' for the first curve) and before the showing up of the Ta's high order BP-loss lines (indicated by 'Ta-high' for the last two curves). We classify these two peaks, 15.8 and 15.9, as the SP1IP1-loss of the film. However, the expected IP1-loss line is too indolent to reveal itself. It is most likely that the IP1-loss is hidden by the 2SP-loss and the SP1-loss which has a tremendous height. The following observations support the above classifications. (1) The Sn's and the Ta's higher order BP-loss lines are not visible in the corresponding spectra. (2) The first peak is not accompanied by a shoulder on its left, but the fresh Sn's EELS has a shoulder (marked as 'A' in the first curve). (3) The last proof can be obtained is by inspecting the position of the first loss peak. The fresh Sn's SP1-loss appears at 10.2 eV (the first three curves) while the Ta's arises at 11.5 eV (the last two curves).

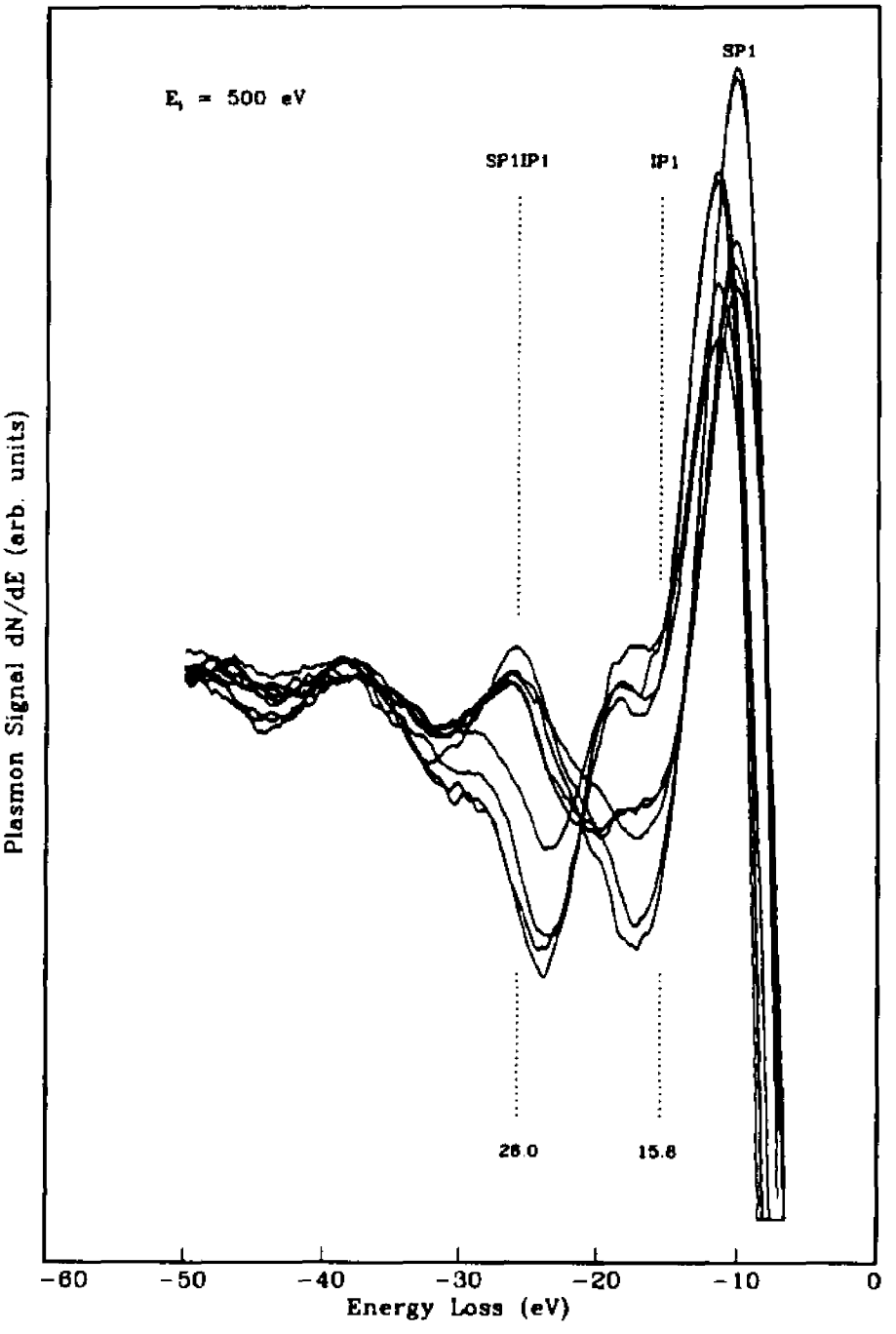

Figure 41. The EELS spectra of a 2.0 ML Sn/Ta film, the zoom view of the plasmon losses is given in figure 42.

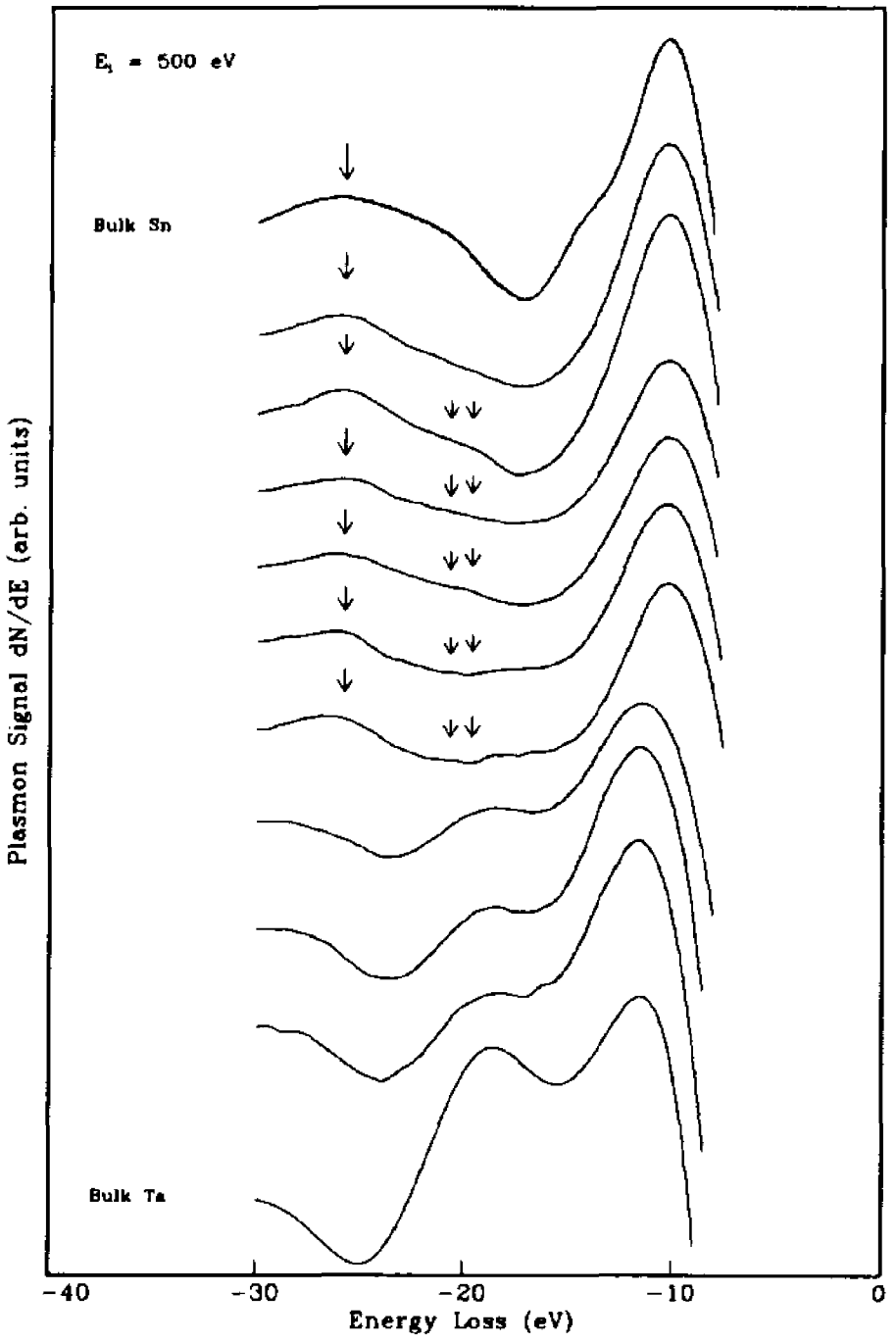

Figure 42. The EELS spectra of a 2.0 ML Sn/Ta film, single film traces after annealing at progressively higher temperatures (up to 1500 K).

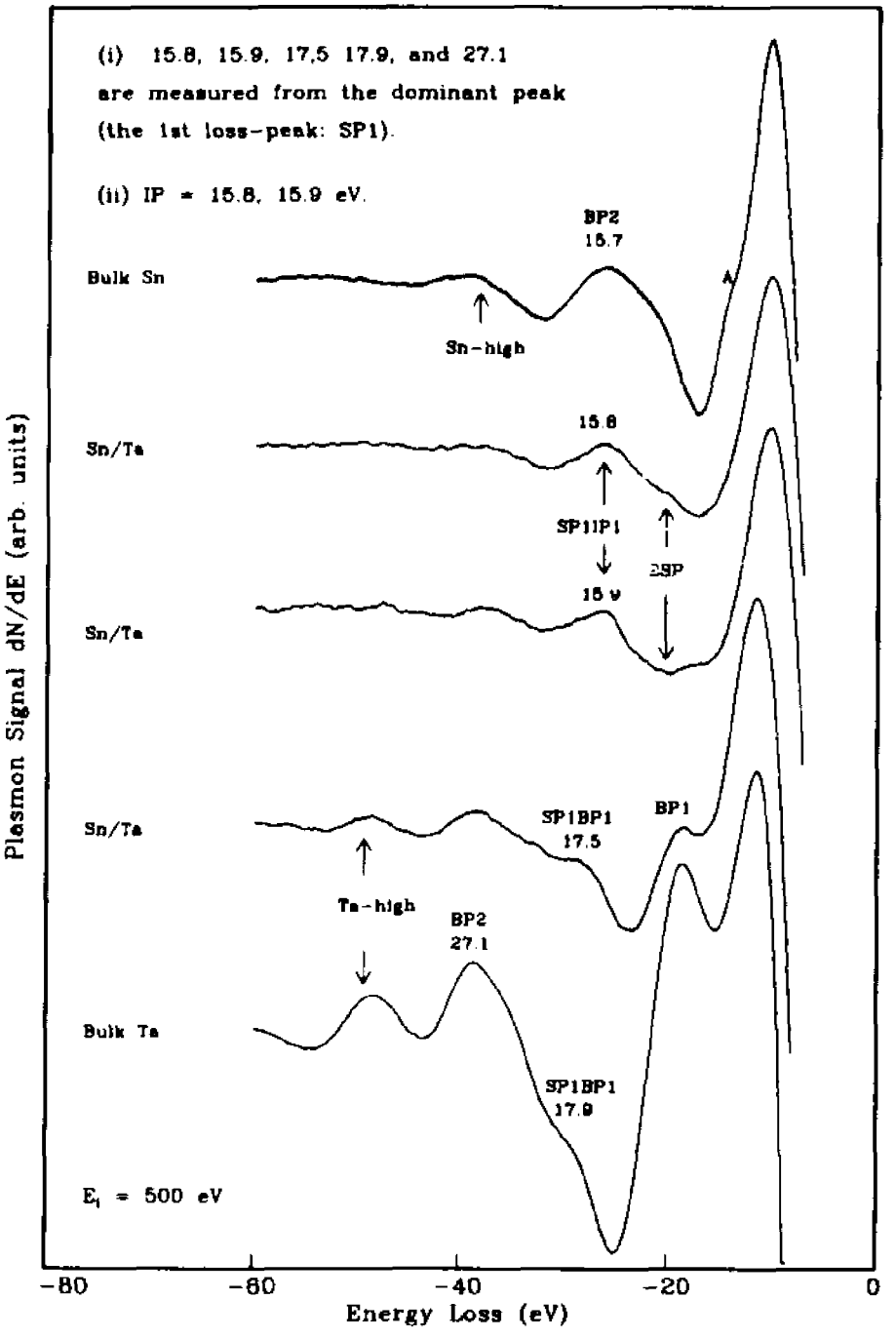

Figure 43. Interface plasmons of the Sn/Ta film, where the measured interface plasmon energy is IP=15.8 eV.

4.3.4 Comparison of plasmon loss energies between the experimental and the predicted values

Overall the IP-losses are observed in all the Sn films which we analyzed as well as the Al/Nb films. The corresponding EELS spectra of the pure metals and the films (IP-loss part) are shown in figures 44 and 45. The arrows in figure 45 point to the experimental observed loss peaks which have been discussed in the previous sections. In case of the Al/Nb film, both the *first-pair* and the *second-pair* of the IP-loss is clearly seen. For all the Sn films, only the *second-pair* of the IP-loss is clearly observed. In case of the Sn/Nb film, the SP1IP1-loss appears as a real peak and the IP1-loss shows up as a shoulder. In case of the Sn/Mo and the Sn/Ta film, the SP1IP1-loss manifests itself as a real peak but the IP1-loss is invisible. All the measured IP-loss energies of the films are fairly close to the values calculated from the semi-classical theory. Or to say it in another way, the semi-classical theory is good for providing a rough guide for the thin film systems and this model is convenient, even though, only Al is a nearly-free-electron type metal.

As discussed in section 3.2, the theoretical ratio $E_b : E_s$ has a well-known value of $\sqrt{2}$, but no common ratio is defined for the interface plasmon loss energies. In order to compare our experimental results with the predicted values, let R, which will be served as a more general ratio, be defined as follows:

$$R \equiv \frac{E_{b1} + E_{b2}}{E_I} \qquad (4.3.4\text{-}1)$$

Where E_{b1}, E_{b2}, and E_I are, respectively, the BP-loss energy of the substrate metal, the BP-loss energy of the adsorbate and the IP-loss energy of the

film–metal interface. Definition of (4.3.4-1) will reduce to the well-known ratio $\sqrt{2}$ by taking $E_{b1} = 0$ (for vacuum), $E_{b2} = E_B$ and $E_l = E_S$ (SP- and BP-loss energy of the metal respectively). By using expression (3.2.10), which is derived in section 3.2 for calculating the IP-loss energy, the ratio R can be expressed as:

$$R = \sqrt{2}\left[1+\left(\frac{2E_{b1}E_{b2}}{E_{b1}^2+E_{b2}^2}\right)\right]^{1/2} \qquad (4.3.4\text{-}2)$$

With a little examination of equation of (4.3.3-2), the maximum ratio $R = 2$, for $E_{b1} = E_{b2}$, will be obtained. All the interfaces, especially the thin–film-metal ones, should have special features which depend on the metals used, therefore the details of the EELS of the films may be different from each other. However the ratio R, calculated from the measured values, can be used as a guide value for comparing the experimental and the theoretical results. Table 13 lists our experimental SP-, BP-, and IP-loss energies along with the theoretical values. In part (a), column 4 is the ratio $E_b:E_s$ and in part (b), column 4 (5) is the experimental (theoretical) ratio defined by the expression (4.3.4-2).

Figure 46(a) is the plot of the SP-loss energies versus the BP-loss energies for the metals studied, where the dash line gives the predicted ratio $1/\sqrt{2}$. An excellent agreement between the experiment and the semi-classical theory can be clearly seen for Al, thus providing an experimental support for the theoretical description of the nearly-free-electron metals. For the transition metals Nb, Mo and Ta, the experimental BP-loss energies are very close to the predicted values and the SP-loss energies are reasonably close to the anticipated values. One would expect that in the transition metals the electrons in the *d*-band would make the situation more complicated. The interband transitions and the electron

screening effects near a surface must be taken into account in order to obtain better agreement between the theory and the experiment.

Figure 46(b) is the plot of the IP-loss energies of the films versus $(E_{b1} + E_{b2})/2$, where the dash line shows the theoretical minimum of the ratio $2/R$ $(2/R_{max} = 1)$. For the vacuum–thin-film–metal sandwich interfaces, we obtain nice results for the Sn/Nb and Sn/Ta films, and reasonable results for the Al/Nb and Sn/Mo films. For the sandwich films, the situation becomes even more complicated than the metal–vacuum interface, so that the above experimental results are indeed in the expected ranges.

In solids, electrons may be generally categorized as core electrons and valence electrons. The inner core electrons are tightly bound to the nuclei; therefore they are well localized and will not affect the behavior of other electrons. At the opposite extreme, the valence electrons overlap with other electrons, hence lose any identification with a specific atom. The perfect metal in this category is Al, which has been well studied in all fields of the solid state physics in both theory and experiments. The simple theory, discussed in section 3.3, works perfectly for Al; which is also confirmed by our results about the SP-, BP- and IP-loss energies' measurements. The more difficult and certainly more interesting case is the so called *d*-band metals (transition metals). The *d* electrons are not so tightly bound by the nuclei and overlap their neighbours; but neither can they be treated as free electrons. Thus the *d* electrons should be treated from a band viewpoint, and this *d*-band is partially filled and overlaps the *s* band which in turn makes the behavior even more complicated. Considering the situation of the surface, a calculation of changes in the band structure is needed for a complete theoretical description.

In the theory section 3.2 about the plasmons, we treated the collective excitations of the electron gas by means of the nearly-free-electron model. When

the energy is sufficiently high, transitions can take place between states in different bands. Since the allowed and forbidden energy bands in metals are discrete, this will result in a discrete structure for these excitation processes, the so called interband transitions. The interband transitions correspond to the excitations between the occupied and the unoccupied levels of the atoms, therefore complete description of the resulting $\varepsilon(\omega,k)$ function requires summation over all possible individual excitations (the last sum-term in expression 3.2.2). In fact it is this sum-term makes the situation more complicated for the transition metals, such as Nb, Mo, and Ta and also possibly Sn, which we have studied.

One point worth mentioning is that several investigators[76-78] interpret the higher order peaks in the EELS of transition metals (TM) as the excitation and the decay of localized *d* electrons. The peak positions in the higher energy region of the EELS are also in reasonable agreement with the theoretical X-ray energy levels. However the interpretations are not completely consistent and require a more accurate calculation of the band structures and a quantitative theory of many-body interactions[31]. Moreover, in our EELS spectra of the thin films, the higher order losses almost vanish under appropriate conditions (figure 30, 40, 43 for Sn films and figure 20 for Al/Nb film), which we would not expect if they are attributable to the localized *d* electrons. Therefore we prefer to interpret the higher order losses as the combination of the plasmon losses especially for the thin films.

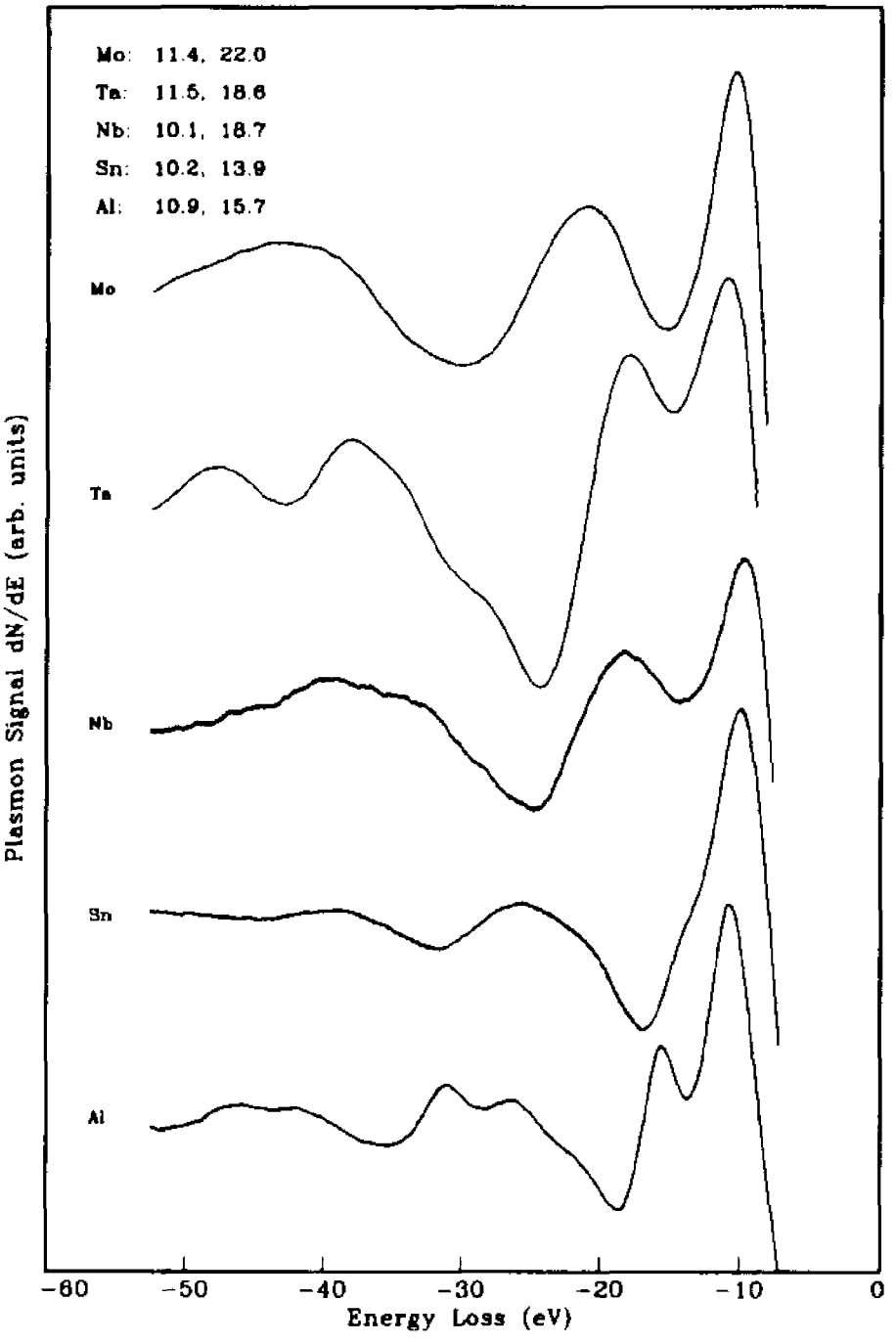

Figure 44. The SP- and BP-losses of different metals: Mo, Ta, Nb, Sn, and Al. On the top left, the first and the second number is, respectively, the SP- and BP-energy.

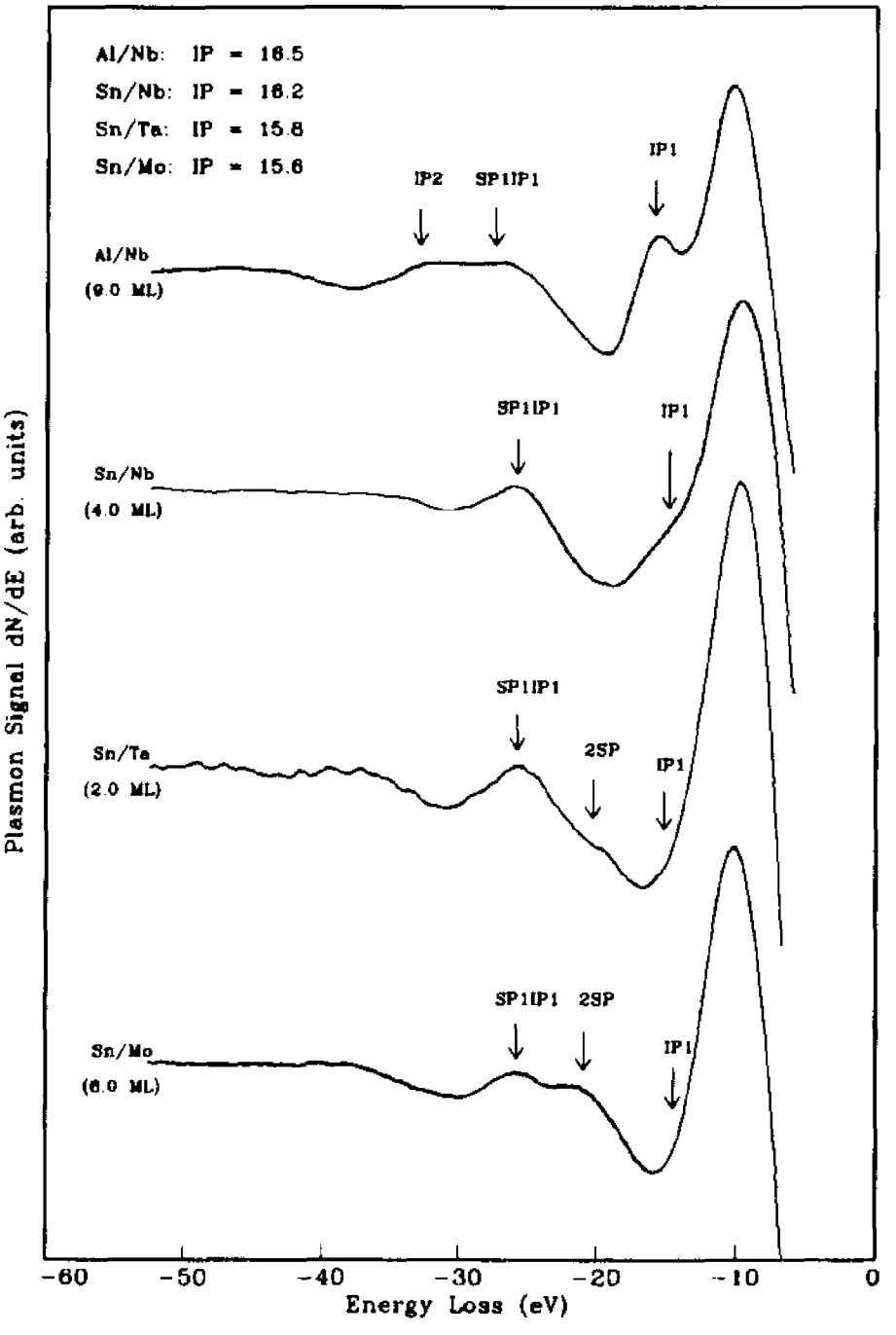

Figure 45. Interface plasmon losses of different films: Al/Nb, Sn/Nb, Sn/Ta, and Sn/Mo; where the arrows indicate the observed and the expected IP- or SP1IP1-loss lines.

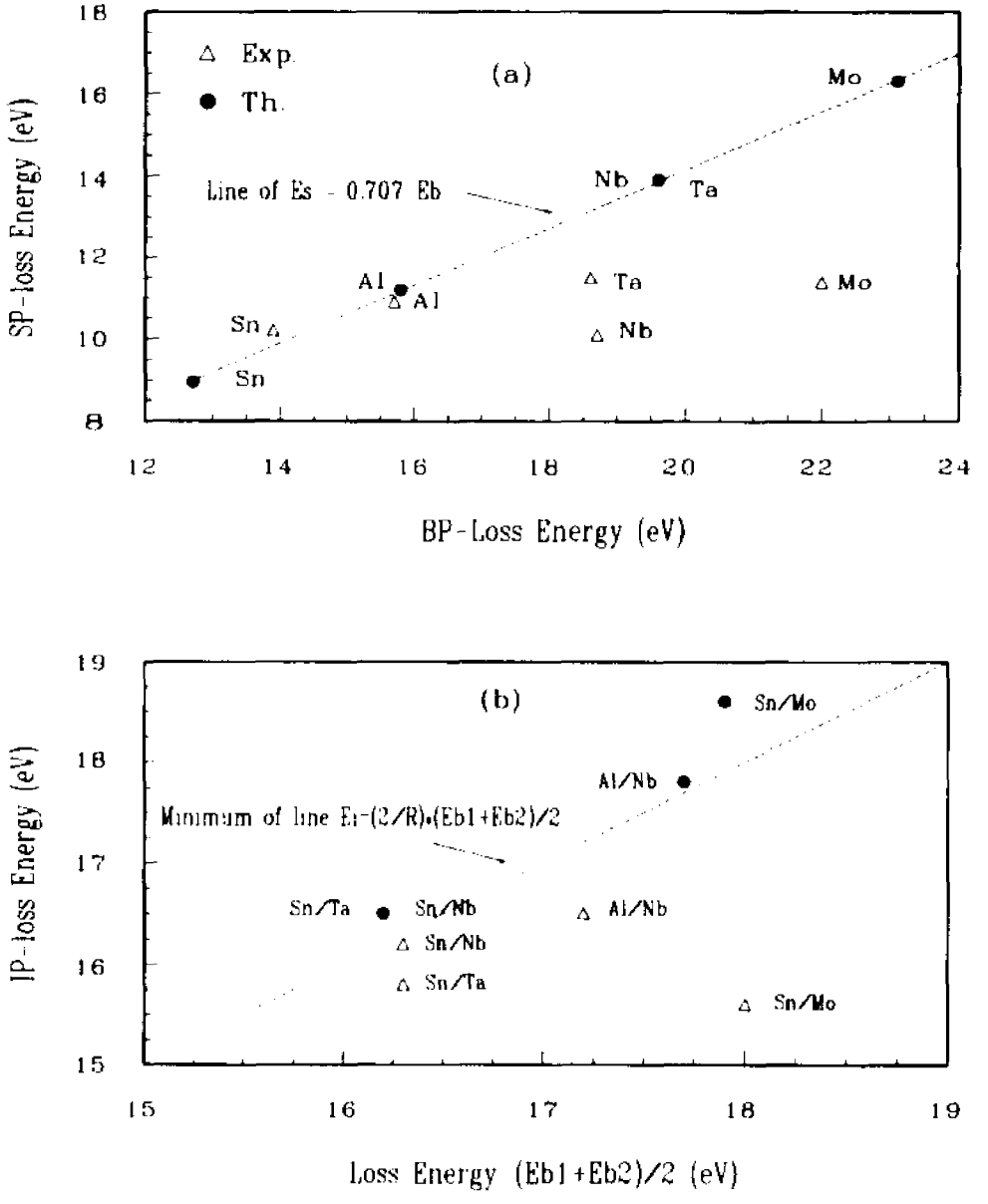

Figure 46 Expertimental and theoretical plasmon loss energies. (a) SP-loss vs. BP-loss. (b) IP-loss vs. (Eb1+Eb2)/2. The lines give the theoretical ratios (definitions are given in text)

Table 13. Plasmon loss energies of pure metals and films

(a) SP- and BP-loss energies of pure metals (eV)

	Bulk Plasmon		Ratio†	Surface Plasmon	
Metal	Exp.	Th.	Exp.	Exp.	Th.
Al	15.7	15.8	1.44	10.9	11.2
Sn	13.9	12.7	1.36	10.2	8.96
Nb	18.7	19.6	1.85	10.1	13.9
Ta	18.6	19.6	1.62	11.5	13.9
Mo	22.0	23.1	1.93	11.4	16.3

(b) IP-loss energies of films (eV)

	Interface Plasmon		Ratio‡	
Film	Exp.	Th.	Exp.	Th.
Al/Nb	16.5	17.8	2.08	1.99
Sn/Nb	16.2	16.5	2.01	1.96
Sn/Ta	15.8	16.5	2.06	1.96
Sn/Mo	15.6	18.6	2.30	1.92

† The ratio of $R=E_B/E_S$.

‡ The ratio of $R=(E_{B1}+E_{B2})/E_I$.

Section 4.4 Growth of Sn Films on Nb

The adsorption and condensation of one metal on another metal substrate, usually refractory metals, are receiving increasing attention mainly because of the possibility of the growth of films monolayer-by-monolayer. A simple technique to determine the coverage and growth mechanism of a deposition process by means of AES has been widely used recently[79-82]. This method consists of plotting the Auger signal of both the substrate and the overlayer as a function of exposure time (the so called AA–*t* plots). In this section the initial stages of deposition of Sn on clean Nb surfaces are presented for a better understanding of the growth mechanism and structure of thin Sn films formed on the Nb substrate.

Films prepared by thermal evaporation of Sn onto Nb surfaces were examined by means of AES technique. The experimental arrangement and thermal evaporation procedures were described in section 2.2.3. The AES measurements were made in the standard manner with following experimental parameters: electron primary energy 2.0 KeV, beam current 45 μA, modulation voltage 2V_{pp}, time constant 0.1 s, sweep rate 1.3 V/s. AES measurements were conducted by monitoring the Nb peak at 161 eV ($M_2M_5N_5$) and the Sn twin peaks at 425 eV ($M_5N_{45}N_{45}$) and 430 eV ($M_4N_{45}N_{45}$). Measurements were taken at regular intervals as the film was built up to give the Auger signals as a function of Sn's coverage on Nb.

Figure 47 shows a series of spectra of Sn 425 eV and 430 eV Auger transitions from clean and Sn-covered surfaces obtained during the growth of a 4.5 ML Sn film on Nb. Figure 48 shows the corresponding sequence of the Auger spectra for Nb. After proper background subtraction the original AES measurements of Nb 161 eV and Sn 430 eV transitions recorded in the derivative

dN(E)/dE mode were numerically integrated. Several selected Nb 161 eV Auger transition peak shapes during the process are given in their numerical integral forms as shown in figure 49. The AES amplitudes of Sn 430 eV and Nb 161 eV peaks, measured from their N(E) form, are plotted as a function of the coverage of Sn as shown in figure 50. The coverage scale is translated by using Sn's Zachariaen metallic radius (ZMR)[83]:

$$ZMR = V_a^{1/3} 2^{-5/6} \qquad (4.4\text{-}1)$$

In expression of (4.4-1), V_a is the volume per atom at room temperature based on bulk density. The Sn's ZMR evaluated by using above formulae is 3.32 Å.

From inspection of figure 50, upon increasing Sn's coverage the heights of the Sn 430 eV and Nb 161 eV Auger transitions do not form a series of straight line segments. Figure 50 only shows that the first step, from 0 to 1 monolayer (ML), of the increase of the Sn 430 eV peak and the attenuation of the Nb 161 eV peak is linear. At about 1 ML the slope of each curves changes; and the curves show a characteristic exponential shape. At higher coverage the slower decrease of the Nb 161 eV height suggests the growth of spreading tin isolated islands. All of the above observations – no further breaks and exponential behavior of both uptake curves, correspond to the Stranski-Kranstanvo (SK) growth mechanism[9,10]. First a complete monolayer forms then three dimensional (3D) islands grow on top of this initially formed adsorbate monolayer. These metallic 3D-islands contribute little to the layer signal but still attenuate the substrate signal slightly, therefore cause the uptake curves having the exponential behaviors after the first break point instead of straight line segments which corresponds to the layer-by-layer growth (FM growth mechanism)[9,10]. The low mobility at room temperature of adsorbed tin atoms presumably causes the film to grow in the form of separate

patches and this prevents the immediate formation of a continuous film, so that the film has a disordered structure. The electron attenuation length (AL) for both the Sn 430 eV and Nb 161 eV can be deduced by modeling the uptake curve in figure 50 at the break point, on the basis of following formula[10]:

$$I / I_0 = \exp[-d / \lambda \cos\beta], \qquad \text{for Nb} \qquad (4.4\text{-}2a)$$

$$I / I_0 = 1 - \exp[-d / \lambda \cos\beta], \qquad \text{for Sn} \qquad (4.4\text{-}2b)$$

where I / I_0 is the ratio of the AES intensity at the monolayer breakpoint to the AES intensity of the bulk material in the uptake curve, d is the overlayer thickness (taken to be 3.32 Å), and $\cos\beta$ is the Auger electron emission per unit solid angle correction which is taken to be 0.74 for the RFA that yields[10]:

$$\lambda = -d \cdot \left[0.74 \cdot \ln(I / I_0)\right]^{-1}, \qquad \text{for Nb} \qquad (4.4\text{-}3a)$$

$$\lambda = -d \cdot \left[0.74 \cdot \ln(1 - I / I_0)\right]^{-1}, \qquad \text{for Sn} \qquad (4.4\text{-}3b)$$

The values of λ_{AL} for the Sn 430 eV and Nb 161 eV are determined to be 8.2 and 7.1 Å respectively. These values are in reasonable agreement with the values determined by using the 'universal' IMFP curves, and other experimental results, for example, Paffett et al[23,83] got 10.0 eV and 9.7 eV for Sn films grown on Pt.

Table 14. The AL (Å) values determined from AA–t plots

Auger Electron Energy (eV)	Our Exp. AL With Sn film	IMFP(Å) from Universal Curve[51]	Others Exp. AL With Sn film	Eq. (3.3.3) Seah & Dench Theory[56]
64 (Pt Peak)	–	4.5 — 26	5.5, 7.2[23,83]	5.8
161 (Nb Peak)	7.1	4.0 — 10	– – –	8.6
430 (Sn Peak)	8.2	5.6 — 13	9.7, 10.0[83,23]	14

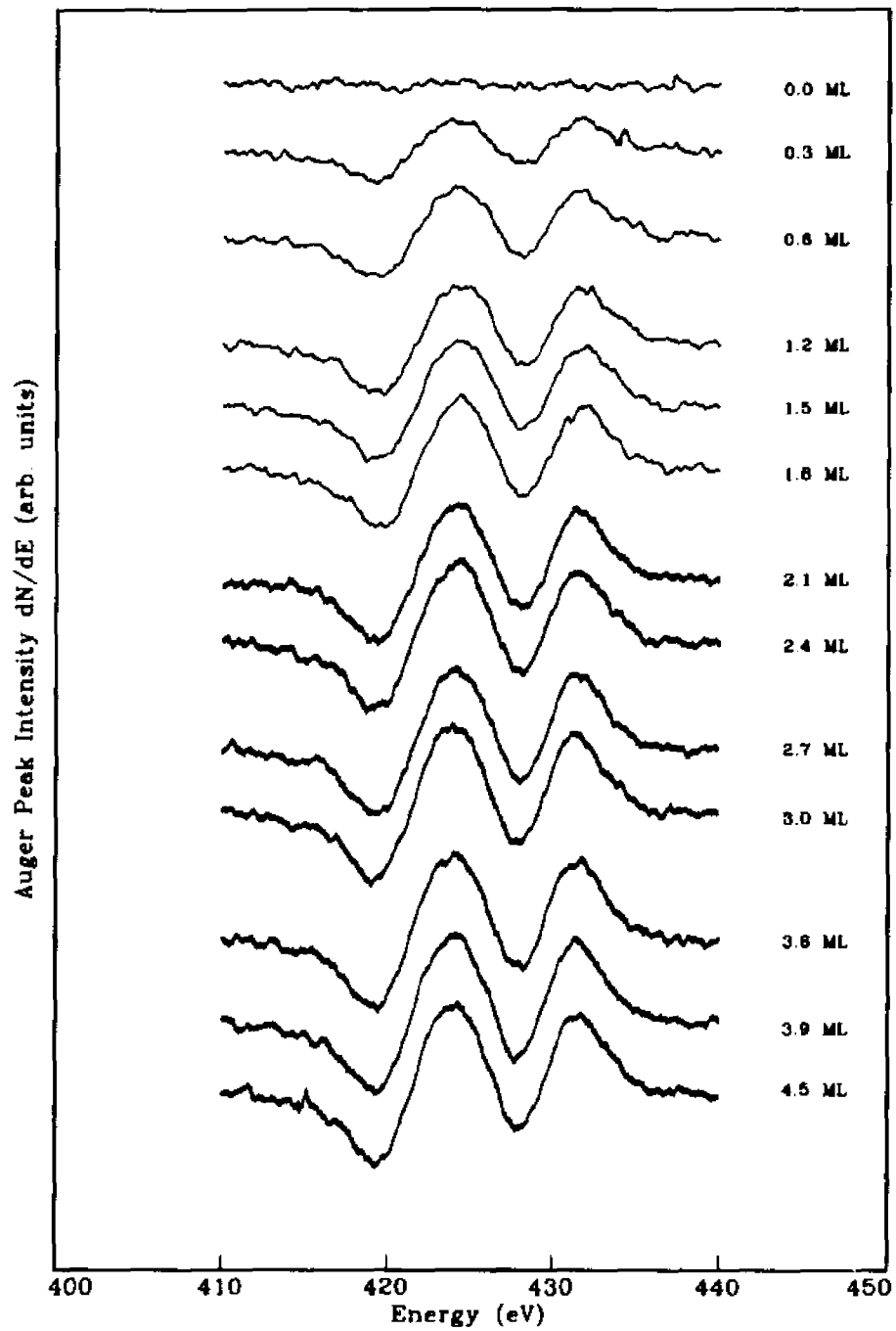

Figure 47. Auger peak intensities of the Sn during its growth on the Nb, curves 0.0 to 1.8 ML have higher sensitivities.

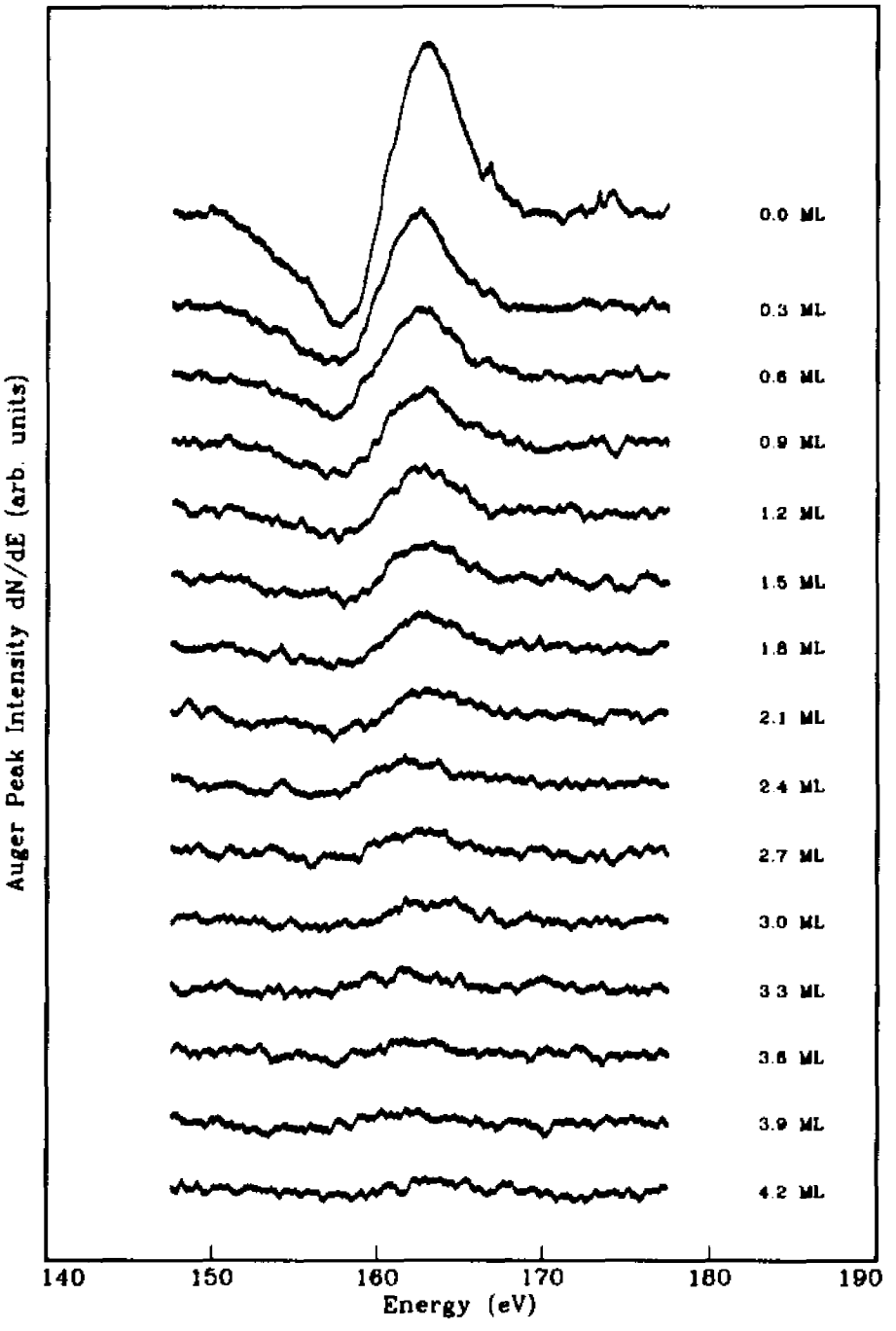

Figure 48. Auger peak intensities of the Nb 161 eV transitions during the growth of Sn on it.

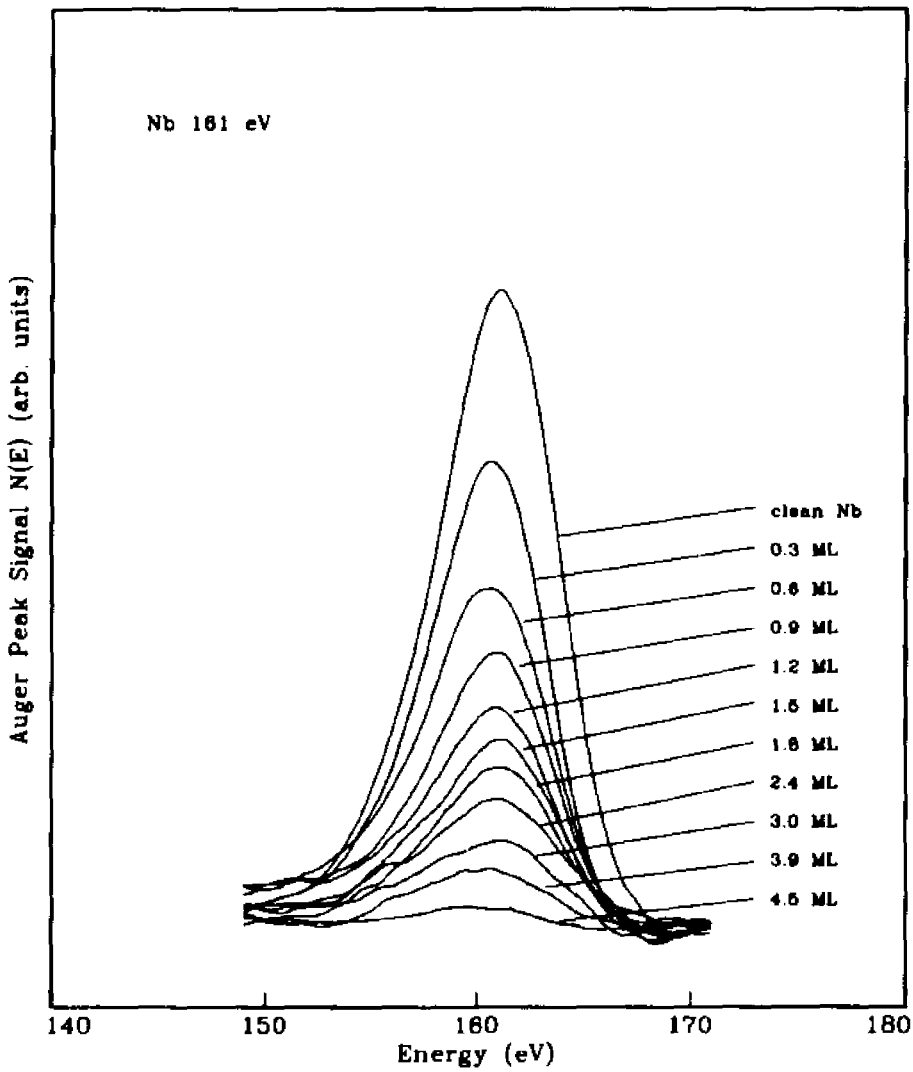

Figure 49. Auger peak heights of the Nb 161 eV transitions during the growth of a Sn film on it.

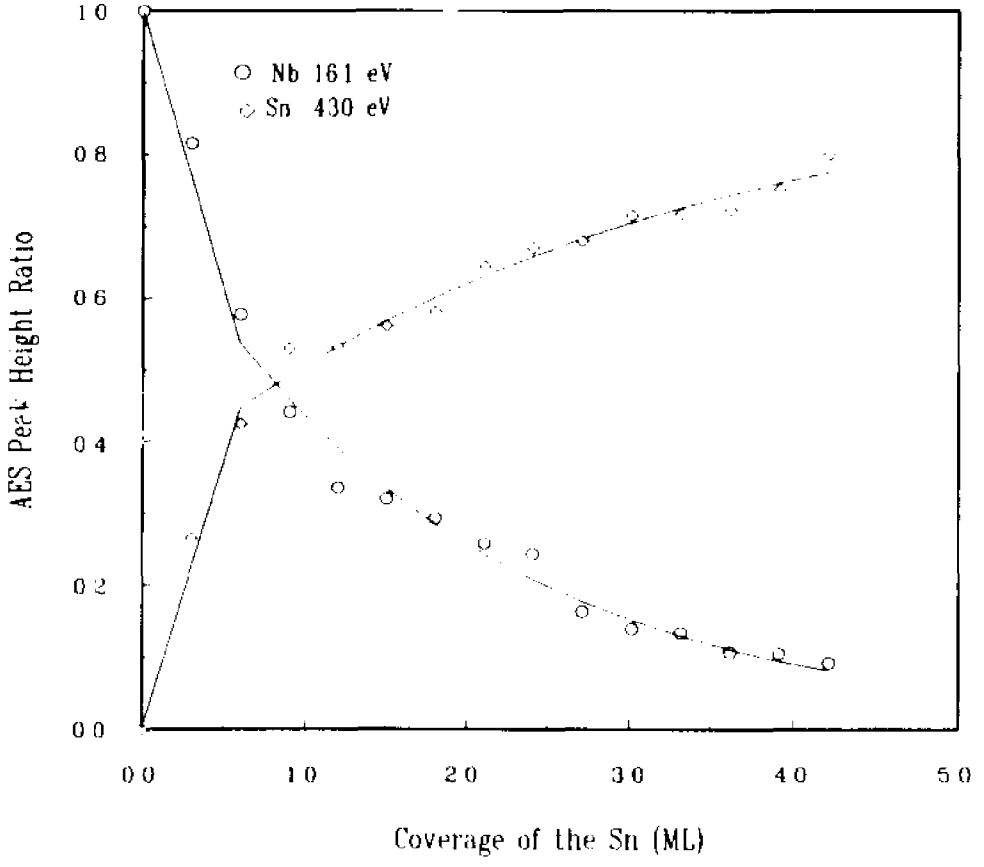

Figure 50 Auger signal intensities (peak-to-peak heights) of the Sn and the Nb as a function of the Sn's coverage (room temperature)

Section 4.5 Conclusions

From the experimental results, we conclude that the bulk plasmon (BP) may show multiple losses but the surface plasmon (SP) shows only a single loss either by itself or superimposed on a main bulk plasmon loss ($n\cdot\Delta E_b+\Delta E_s$). For some metals the double surface plasmon loss shows up as a shoulder instead of a real peak. After careful examination of the spectra and by fitting the Lorentzian line shape to them, these double surface plasmon loss lines are successfully discerned apart from other bulk plasmon loss lines and surface plasmon loss lines. The conclusion is that the double surface plasmon loss does exist even though its probability is low and it is not so obviously seen in the spectra owing to the fact that it is embedded inside the larger first two plasmon loss pairs. For transition metals Nb, Mo, and Ta, the observation that the higher order bulk plasmon loss peaks show a little shift from the anticipated combination positions is observed, due to the interband transitions.

Moreover extra plasmon losses, which are ascribed to the interface plasmon losses (IP), are clearly observed in all the Sn films as well as in the Al/Nb film. In all cases, the SP1IP1-loss (combination of SP- and IP-loss) manifests itself as a real peak. On the other hand, the first interface plasmon loss appears as a real peak only in the Al/Nb film, and it is faintly seen in other Sn films, implying that it is hidden by the larger single SP-loss or by the double SP-loss or more likely by both of them. The observed values of the interface plasmon loss energies are in reasonable agreement with the semi-theoretical values. One would not expect a perfect agreement between the theory and the experiment, since the surface conditions and some special effects, such as the surface roughness and the crystallinity effects[71], will also affect the spectra

A similar four stages annealing behavior was observed in both the AES plots and the EELS spectra (the *first-pair* loss heights) for different Sn films on both Nb and Mo. In the first stage (low temperature region), nothing happens; in the second stage, the smoothing of the 3D-islands occurs; in the third plateau stage, a relatively stable surface alloy accounts for the thermal stability of this region; in the last stage (high temperature region), the loss of the adsorbate occurs. Also observed are the systematic shifts of the break points, for changing from one stage to another, to higher temperatures when the thickness of the film increases. For thicker films more time is required for each rearrangement of the structure at a given temperature. The mobility of atoms increases rapidly with temperature; therefore shifts of the break points are indeed expected. The Sn films go through the same sequence of changes although at slightly lower temperatures for Mo than for Nb. The similarity is not surprising since the electronic configurations of Nb and Mo differ by just one *d* electron.

The growth of the Sn films on a Nb substrate at room temperature is consistent with the Stranski-Kranstanov mechanism (SK mode). By examining the corresponding AES' AA–*t* plots of both the Sn and Nb, the electron's AL (attenuation length) for the Sn 430 eV and Nb 161 eV is found to be 8.2 and 7.1Å respectively. These values are in reasonable agreement with the values determined from the universal IMFP curves (figure 7).

References

[1] H. Ibach, M. Balden, D. Bruchmann and S. Lehwald. *Surf. Sci.*, **269/270**, 94 (1992).

[2] G. F. Chiarotti, f. Fumi and M. P. Tosi, *Current Trends in the Physics of Materials*, North-Holland, Amsterdam, p.697 (1990).

[3] P. Auger, *J. Phys. Radium* **6**, 205, (1925).

[4] J. M. Dickey, *Surf. Sci.*, **50**, 515 (1975).

[5] J. M. Dickey, H. H. Farrell, O. F. Kammerer, and M. Strongin, *Phys. Letters*, **32A**, 483 (1970); and *J. Appl. Phys.*, **42**, 5808, (1971).

[6] K. Sturm and W. Schulke, *Phys. Rev. B.*, **46**, 7193 (1992).

[7] G. F. Giuliani and J. J. Quinn, *Phys. Rev. Lett.*, **51**, 919 (1983).

[8] E. Bauer and J. H. van der Merwe, *Phys. Rev. B*, **33**, 3657 (1986).

[9] J. A. Nieminen and K. Kaski, *Surf. Sci.*, **185**, L489 (1987).

[10] C. Argile and G. E. Rhead, *Surf. Sci. Rep.*, **10**, 277 (1989).

[11] J. Kolaczkiewicz, M. Hochol, and S. Zuber, *Surf. Sci.*, **247**, 284 (1991).

[12] A. Zangwill, *Physics at Surface*, Cambridge Univ., Cambridge, p.20 (1986).

[13] Scientific Solutions Inc., Solon, Ohio

[14] Borland International Inc., Scotts Valley, CA.

[15] A. Savitzky and M. J. E. Golay, *Anal. Chem.*, **36**, 1627 (1964).

[16] Material Research Coporation, Orangenurg, New York.

[17] R. D. Mathis Company, Long Beach, Californian.

[18] K. H. Behrndt, *Film-Thickness and Deposition-Rate Monitoring Devices and Techniques for Producing Films of Uniform Thickness: Physics of Thin Films*, Vol. 3, edited by G. Hass and R. E. Thun, Academic, New York, p.21 (1966).

[19] M. Tomellini and G. A. Attard, *Surf. Sci. Lett.*, **245**, L179 (1991).

[20] W. Wegscheider, K. Eberl, U. Menczigar, and G. Abstreiter, *Appl. Phys. Lett.*, **57**, 875 (1990).

[21] D. G. Emel'yanenkov, V. I. Zaporozhchenko, V. V. Kantsel', and V. I. Rakhovskii, *Sov. Phys. Crystallogr.*, **27**, 454 (1982).

[22] C.J. Barnes, H.Asonen, A. Salokatve and M.Pessa, *Surf. Sci.*, **184**, 163 (1987).

[23] M. T. Paffett., A. D. Logan, R. J. Simmonson, and B. E. Koel, *Surf. Sci.*, **250**, 123 (1991).

[24] J. M. Heitzinger, S. C. Gebhard, D. H. Parker, and B. E. Koel, *Surf Sci.*, **260**, 151 (1992).

[25] Ch. Park, E. Bauer, and H. Poppa, *Surf. Sci.*, **154**, 371 (1985).

[26] L. C. Feldman and J. W. Mayer, *Fundamentals of Surface and Thin Film Analysis*, North-Holland, New York, p.272 (1986).

[27] M. Thompson, M. D. Baker, A. Christie, and J. F. Tyson, *Auger Electron Spectroscopy*, Wiley, New York, p.43, 73, 102 (1985).

[28] C. C. Chang, *Surf. Sci.*, **25**, 53 (1971).

[29] J. J. Pireaux, J. Ghijsen, J. Wm. McGowan, J. Verbist and R. Caudano, *Surf. Sci.*, **80**, 488 (1979).

[30] A. Hoffman, T. Maniv, and M. Floman, *Surf. Sci.*, **193**, 513 (1988).

[31] A. Cornaz, M. Erbudak, P. Aebi, F. Stucki, and F.Vanini, *Phys. Rev. B*, **35**, 3062 (1987).

[32] D. Pines and D. Bohm, *Phys. Rev.* **85**, 338 (1952); and *Phys. Rev.* **92**, 609 (1953).

[33] P. M. Th. M. van Attekum and J. M. Trooster, *Phys. Rev. B* **18**, 3872 (1978).

[34] C. F. McConville, D. L. Seymour, D. P. Woodruff, and S. Bao, *Surf. Sci.*, **188**, 1 (1987).

[35] I. Colera, S. Rey, and J. L. de Segovia, *Surf. Sci.*, **251/252**, 851 (1991).

[36] D. F. Cox and G. B. Hoflund, *Surf. Sci.*, **151**, 202 (1985).

[37] H. Saijo, Y. Konda, and M. Shiojiri, *J. Vac. Sci. Technol. A*, **9**, 201 (1991).

[38] R. W. Hamming, *Digital Filters*, Prentice-Hall, New Jersey, p.34, 39, 78 (1983).

[39] P. D. Willson and T. H. Edwards, *Appl. Spectrosc. Rev.*, **12**, 1 (1976).

[40] C. G. Enke and T. A. Nieman , *Anal. Chem.*, **48**, 705A (1976).

[41] M. Ohno, *J. Phys. C*, **17**, 1437 (1984).

[42] G. D. Mahan, *Many-Particle Physics*, Plenum Press, New York, p.428, 439, 710 (1990).

[43] P. Nozieres and D. Pines, *Phys. Rev.*, **109**, 741; and **109**, 762 (1958).

[44] A. Stern and R. A. Ferrell, *Phys. Rev.*, **120**, 130 (1960).

[45] G. W. Simmons and E. J. Scheibner, *J. Appl. Phys.*, **43**, 693 (1972).

[46] H. Ibach and H. Luth, *Solid State Physics*, Springer-Verlag, Berlin, p.271 (1990).

[47] D. A. Cox and J. P. Kemp, *Surf. Sci.*, **201**, 225 (1989).

[48] T. Inaoka and T. Chihara, *Surf. Sci.*, **208**, 71 (1989).

[49] J. Lindhard, *K. Dan. Vidensk. Selsk. Mat. Fys. Medd.*, **28**, No.8 (1954).

[50] J. J. Quinn, *Phys. Rev.*, **126**, 1453 (1962).

[51] C. L. Briant and R. P. Messmer, *Auger Electron Spectroscopy*, Academic, Boston, p.56 (1988).

[52] D. P. Woodruff and T. A. Delchar, *Modern Techniques of Surface Science*, Cambridge University, Cambridge, p.77 (1986).

[53] D. R. Penn, *Phys. Rev. B*, **35**, 482 (1987).

[54] S. Tanuma, C. J. Powell, and D. R. Penn, *Surf. Sci.*, **192**, L849 (1987); and *Surf. Interface Anal.*, **11**, 577, (1988).

[55] B. Lesiak, A. Jabkonski, Z. Prussak, and P. Mrozek, *Surf. Sci.*, **223**, 213 (1989).

[56] M. P. Seah and W. A. Dench, *Surface Interface Anal.*, 1, 2 (1979).

[57] C. J. Powell, *Surf. Interface Anal.*, 7, 256, (1985); and *J. Electron Spectro. Relat. Phenom.*, **47**, 197, (1988).

[58] R. M. Digilov, E. P. Fel'dman, and V. M. Yurchenko, *Sov. Phys. Dokl.*, **33**, 933 (1989).

[59] M. Weinert, R. E. Watson, J. W. Davenport, and G. W. Fernando, *Phys. Rev. B*, **39**, 12585 (1989).

[60] R. J. Needs, *Phys. Rev. Lett.*, **58**, 53 (1987); and *Phys. Rev. B*, **42**, 10933 (1990).

[61] R. E. Watson, M. Weinert, and J. W. Davenport, *Phys. Rev. B*, **35**, 9284 (1987).

[62] M. H. Grabow and G. H. Gilmer, *Surf. Sci.*, **194**, 333 (1988).

[63] J. E. T. Andersen and P. J. Moller, *Surf. Sci.*, **258**, 247 (1991).

[64] J. P. Biberian and G. A. Somorjai, *Appl. Surf. Sci.*, **2**, 352 (1979).

[65] R. Daling, W. van Haeringen, and B. Farid, *Phys. Rev. B.*, **45**, 8970 (1992).

[66] K. Sturm, W. Schulke, and J. R. Schmitz, *Phys. Rev. Lett.*, **68**, 228 (1992).

[67] H. K. Sy and T. C. Chua, *Phys. Lett. A*, **169**, 99 (1992).

[68] W. Schulke and A. Kaprolat, *Phys. Rev. Lett.*, **67**, 879 (1991).

[69] K. J. Jainendra and P. B. Allen, *Phys. Rev. Lett.*, **54**, 947; and **54**, 2437 (1985).

[70] D. L. Seymour, C. F. McConville, D. P. Woodruff, and J. E. Inglesfield, *Surf. Sci.*, **214**, 57 (1989).

[71] P. J. Feibelman, *Phys. Rev. B*, **23**, 2629 (1981); and *Prog. Surf. Sci.*, **12**, 287 (1982).

[72] L. H. Hedin, *X-ray Spectroscopy*, McGraw-Hill, New York, p.226, (1974).

[73] D. R. Penn, *Phys. Rev. Lett.* **38**, 1429, and **40**, 568 (1977).

[74] Computer Graphics Services, Ithaca, NY.

[75] G. Mondio, F. Neri, M. Stocker, T. Janssens, G. R. Casrto, and K. Wandelt, *Surf. Sci.*, **251/252**, 243 (1991).

[76] W. K. Schuber and E. L. Wolf, *Phys. Rev. B*, **20**, 1855 (1979).

[77] E. Colavita, A. Amoddeo, R. Agostino, A. Bonanno, G. Chiarello, V. Formoso, and L. S. Caputi, *Surf. Sci.*, **211/212**, 481 (1989).

[78] M. Erbudak, F. Vanini, D. Sulmoni, and P. Aebi, *Surf. Sci.*, **189/190**, 771 (1987).

[79] M. Tikhov and E. Bauer, *Surf. Sci.*, **203**, 423 (1988).

[80] I. Andriamanantenasoa, J. P. Lacharme, and C. A. Sebenne, *Surf. Sci.*, **189/190**, 563 (1987).

[81] C. Park, E. Bauer, and H. Poppa, *Surf. Sci.*, **187**, 86 (1987).

[82] J. R. Baumann, E. K. Liebemann, M. Simon, and E. Bucher, *Phys. Rev. B*, **45**, 3778 (1992).

[83] M. T. Paffett and R. G. Windham, *Surf. Sci.*, **208**, 34 (1989).